

# Ion irradiation and modification: The role of coupled electronic and nuclear energy dissipation and subsequent nonequilibrium processes in materials

Cite as: Appl. Phys. Rev. **7**, 041307 (2020); doi: 10.1063/5.0027462

Submitted: 28 August 2020 · Accepted: 15 October 2020 ·

Published Online: 23 November 2020



View Online



Export Citation



CrossMark

Yanwen Zhang<sup>1,2,a)</sup>  and William J. Weber<sup>1,2,a)</sup> 

## AFFILIATIONS

<sup>1</sup>Materials Science and Technology Division, Oak Ridge National Laboratory, Oak Ridge, Tennessee 37831, USA

<sup>2</sup>Department of Materials Science and Engineering, University of Tennessee, Knoxville, Tennessee 37996, USA

<sup>a)</sup>Authors to whom correspondence should be addressed: [zhangyl@ornl.gov](mailto:zhangyl@ornl.gov) and [wjweber@utk.edu](mailto:wjweber@utk.edu)

## ABSTRACT

Understanding material responses to energy deposition from energetic charged particles is important for defect engineering, ion-beam processing, ion-beam analysis and modification, geologic aging, space exploration, and nuclear applications. As an incident ion penetrates a solid, its energy is transferred to electrons and to atomic nuclei of the solid. Much of this electronic energy deposition is subsequently transferred to the atomic structure via electron–phonon ( $e$ – $ph$ ) coupling, leading to local inelastic thermal spikes in which energy dissipation is influenced by the local environment. In addition, intense ionization can lead to high densities of localized electronic excitations in wide-bandgap materials and ceramics that can affect defect dynamics and atomic mobility. Specifically, energy exchange between electrons and atomic nuclei, along with localized electronic excitations, can lead to substantial competitive (ionization-induced annealing), additive (both electronic and nuclear energy depositions contributing to damage production), and synergistic (more damage than the sums of separate damage processes) effects. Although nonmonotonic effects of the  $e$ – $ph$  coupling strength and athermal processes are demonstrated for pre-existing defects and residual damage during ion–solid interactions, there is limited understanding of when such electronic effects must be considered in atomic-scale models of damage production and evolution in a broad variety of materials. Complex ceramics and chemically disordered solid solution alloys with different constituent elements allow a systematic evaluation of defect dynamics and irradiation performance with increasing complexity. Current knowledge regarding tuning of bonding characteristics and chemical disorder to control atomic-level dynamics is reviewed. Although a lack of fundamental understanding obstructs the advancement of reliable predictions for ion beam material modification, it highlights challenges and opens research opportunities. Insights into the complex electronic and atomic correlations with extreme energy deposition will strengthen our ability to design materials and predict ion-irradiation-induced damage in a radiation environment, and they may pave the way to better control fundamental processes and design new material functionalities for advanced technologies.

© 2020 Author(s). All article content, except where otherwise noted, is licensed under a Creative Commons Attribution (CC BY) license (<http://creativecommons.org/licenses/by/4.0/>). <https://doi.org/10.1063/5.0027462>

## TABLE OF CONTENTS

I. INTRODUCTION .....	2	B. Electronic energy deposition-induced athermal processes .....	4
II. COUPLED ELECTRONIC AND ATOMIC ENERGY DEPOSITION AND DISSIPATION PROCESSES.....	3	C. Partitioning of electronic and atomic energy depositions from ions .....	7
A. Ion-induced coupled electronic and atomic processes .....	3	D. Modeling effects of electronic and damage energy dissipation on defects .....	9

1.	Low energies .....	10
2.	Intermediate energies.....	10
3.	High energies .....	12
E.	Experimental approaches to separate and quantify effects.....	12
III.	INTRINSIC MATERIAL PROPERTIES AND ION-INDUCED NONEQUILIBRIUM PROCESSES .....	13
A.	Nonequilibrium defect dynamics at the level of electrons and atoms .....	13
B.	Material intrinsic properties affecting energy dissipation at the level of electrons and atoms ...	13
1.	Covalent and ionic materials .....	14
2.	Metallic materials .....	14
C.	Similarities of energy dissipation in complex ceramics and chemically disordered alloys .....	15
IV.	RADIATION-INDUCED NONEQUILIBRIUM PROCESSES IN COVALENT AND IONIC MATERIALS.....	15
A.	Competitive effects leading to defect annealing...	15
B.	Additive effects on microstructure modification ..	19
C.	Synergistic effects causing increased damage production .....	20
D.	Electronic excitations and relaxation.....	22
V.	RADIATION-INDUCED NONEQUILIBRIUM PROCESSES IN CHEMICALLY DISORDERED METALLIC ALLOYS .....	23
A.	Slow heat dissipation delaying damage buildup ..	23
B.	Electronic and ionic energy exchange resulting in more isolated smaller defect clusters .....	24
C.	Nonequilibrium damage evolution.....	26
1.	Defect energetics, directional mass transport, and defect evolution.....	26
2.	Strain relaxation from inelastic thermal spike.....	26
D.	Ionization effects in complex metal alloys under ion irradiation .....	27
1.	Evolution of pre-existing defects under ionizing irradiation.....	28
2.	Metallic alloys responding to extreme electronic energy deposition .....	29
VI.	MATERIAL MODIFICATION BY ION BEAMS: IRRADIATION CONDITION AND CHEMICAL DISORDER .....	30
VII.	OUTLOOK AND SUMMARY.....	31

## I. INTRODUCTION

Energetic ion beams over a broad range of ion masses and energies have been applied for a variety of purposes over the past several decades, such as to create device functionality,<sup>1–4</sup> to enhance material properties,<sup>5–10</sup> to synthesize or control nanostructures or low-dimensional materials,<sup>11–16</sup> to modify strain,<sup>17,18</sup> to induce phase transformation,<sup>19</sup> and to emulate the response of materials to extreme radiation environments.<sup>20–22</sup> In recent years, ion beams have been also used as a powerful tool to reveal the effects of coupled electronic and nuclear energy dissipations on nonequilibrium defect evolution processes.<sup>23</sup>

The interactions of incident ions or energetic primary knock-on atoms (PKAs) with solids result in energy deposition to electrons and atomic nuclei and subsequent energy dissipation. It is well established that the interaction of energetic ions with solids initiates energy transfer processes in both electronic and atomic structures. Despite successes in a wide range of applications for ion beams, the fundamental understanding of the intrinsically coupled energy deposition/dissipation processes in the electronic and atomic subsystems, as well as defect production and evolution in irradiated materials, lags far behind.<sup>23,24</sup> It is particularly challenging to understand and model the electronic effects resulting from increasing chemical complexity in ceramics, compound semiconductors, and disordered alloys—for example, to describe defect production and evolution both shortly after individual irradiation events and under prolonged irradiations. The importance and challenge of modeling these electronic energy dissipation processes, and their impacts on defect prediction and damage evolution, are becoming increasingly recognized for ceramics<sup>25–31</sup> and metal alloys<sup>24,32</sup> because of the complexity of the intertwined processes. However, the dynamics of elastic energy transfer to atomic nuclei, inelastic energy transfer to electrons, energy dissipation via both subsystems, exchange of energy between electrons and atomic nuclei via electron–phonon (*e*-*ph*) coupling, and accompanying ionization and atomic motions are only beginning to be understood and modeled.

The controlled use of ion beams to tailor the functionality of materials or advance radiation-tolerant concepts demands comprehensive understanding and predictive models of the energy transfer processes at the level of electrons and atoms. This review describes the current understanding of the partitioning of electronic and nuclear energy depositions and subsequent coupled nonequilibrium processes and describes how to use ion beams to understand and control energy dissipation processes in order to tailor material functionality, create nanoscale phase transitions, and develop radiation-tolerant materials. This article highlights the phenomena from the level of atoms and electrons in crystalline materials (e.g., ceramics, semiconductors, and metal alloys). The coupled effects of ionization and elastic collision processes are discussed in terms of bond types (i.e., covalent, ionic, metallic, or mixed bonds), bonding strength, local elemental inhomogeneities that increase with chemical complexity, and energy dissipation processes. This review of the behavior of model material systems provides powerful insights into how energy dissipation under non-equilibrium conditions influences defect production, recombination, and evolution. The review combines two novel points of view: (1) the role of energy dissipation through coupled electronic and atomic subsystems and its impact on atomic processes and (2) the role of extreme chemical complexity in modifying these energy dissipation mechanisms.

This review is organized into seven sections. Following Sec. I, coupled electronic and atomic energy deposition and dissipation processes are described in Sec. II with a clarification of ion-induced non-equilibrium athermal processes<sup>33</sup> vs thermal equilibrium damage evolution. To clarify ionization effects, athermal processes induced by electron beams (e-beams) are also included. The use of the Stopping and Range of Ions in Matter (SRIM) code, which includes the Transport of Ions in Matter (TRIM) subroutine,<sup>34,35</sup> and similar codes (e.g., IM3D<sup>36–38</sup> and Iradina<sup>39–41</sup>) to estimate the energy deposition to the two subsystems as a function of depth for different ions is

discussed with examples. Several novel experimental and computational tools employed to reveal coupled effects are described in Secs. II D and II E. Section III discusses the intrinsic materials properties and ion-induced nonequilibrium processes that control energy dissipation and structural stability. In Sec. IV, irradiation-induced non-equilibrium processes in covalent and ionic materials are discussed. Three distinctively different consequences—competitive (annealing), additive, and synergistic (enhanced) responses of defect production and evolution—are attributed to the coupled electronic and nuclear energy dissipation processes and/or the coupling of electronic energy dissipation processes with pre-existing defects. In Sec. V, irradiation-induced nonequilibrium processes in chemically disordered metallic alloys are discussed. A brief summary of material modification by ion beams is provided in Sec. VI, with focuses on irradiation condition and chemical disorder, to demonstrate current knowledge of ion-induced irradiation damage and material applications that benefit from control and tailoring of ionization effects. This review, ending with a summary and outlook, will hopefully pave the way for the use of ion beams to design new functionalities in material systems and to discover materials intrinsically tolerant to irradiation damage.

## II. COUPLED ELECTRONIC AND ATOMIC ENERGY DEPOSITION AND DISSIPATION PROCESSES

### A. Ion-induced coupled electronic and atomic processes

The irradiation of solids with energetic charged particles can lead to structural modifications and phase transformations that can dramatically alter the physical and chemical properties of the materials. Energy deposition from ions to a crystalline material causes disturbances in both the atomic and electronic structures [Fig. 1(a)]. When energetic particles penetrate a material, energy and momentum are transferred from the incident ions to the atomic nuclei via nuclear stopping powers ( $dE/dx_{\text{nuc}}$  or  $S_n$ ) and to target electrons via electronic stopping powers ( $dE/dx_{\text{ele}}$  or  $S_e$ ). Both types of transfers are expressed in terms of average energy transferred per unit of path length of the incident ion, e.g., keV/nm, or further normalized by the mass density of the material, e.g., keV/(mg/cm<sup>3</sup>). This energy deposition results in elastic atomic collisions that displace atoms and can cause local heating [i.e., an elastic thermal spike, as shown in Fig. 1(b)] and intense ionization that can lead to localized electronic excitations and local lattice heating [i.e., an inelastic thermal spike, as shown in Fig. 1(c)]. While “ionization” generally refers to adding electrons to or removing them from atoms or molecules by various means, in this review, it refers to the process in which energy is transferred to electrons in a solid by energetic charged particles in motion.

As the kinetic energy transferred to an atom ( $S_n$ ) from a single incident ion collision can be greater than the energy needed to permanently displace the atom from its lattice site (i.e., displacement energy), a displaced atom can become a PKA that has sufficient energy to displace additional target atoms [Figs. 1(a) and 1(b)] and even create a cascade of elastic atomic collisions that result in a high local concentration of Frenkel defects and more-complex defect clusters in the structure. Some of the energy from the PKA and secondary recoils in the cascade is also transferred to electrons and the remaining energy eventually is transferred to phonons in an elastic thermal spike. Energy transferred to target electrons ( $S_e$ ) by the incident ion, PKAs, and secondary recoils is dissipated in cascades of electron-electron energy

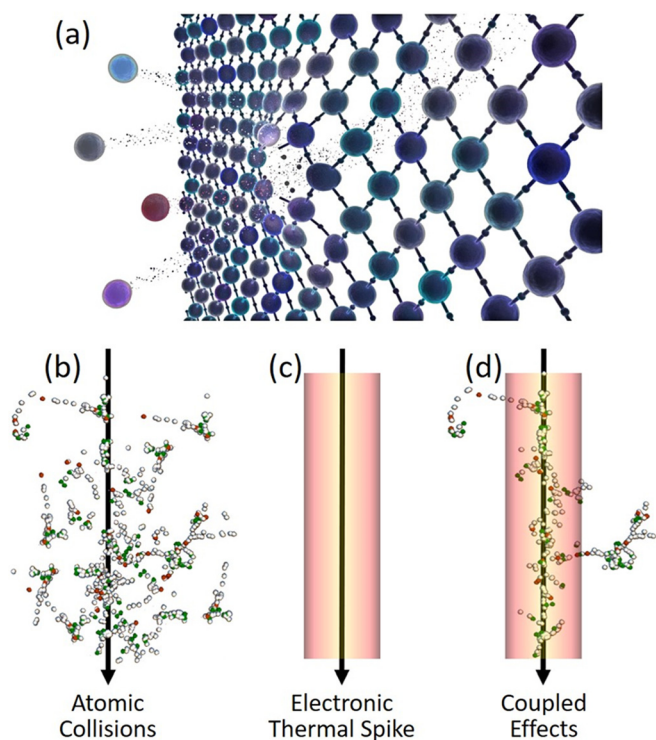


**FIG. 1.** Schematic illustrations of ion–solid interactions: (a) kinetic energy transfer to electrons and atomic nuclei, inducing atomic displacements, bond breaking, and lattice distortion, (b) dense collision cascade event, (c) electronic excitation and inelastic thermal spike along the ion path, and (d) coupled electronic and atomic processes.

exchanges that result in locally superheated electrons and the production of electron-hole (e-h) pairs. Depending on the bond types (i.e., ceramics or metals), the formation of localized electronic excitations can rupture or change the nature of covalent/ionic bonds, modify valence electron distributions, and lead to the formation of charged defects, enhanced defect and atomic mobilities, and increased system energy.<sup>42</sup> Furthermore, high electronic temperatures lead to highly localized inelastic thermal spikes on the atomic lattice via  $e\text{-}ph$  coupling that initiate short-lived transient thermal processes, which can result in defect formation, diffusion, phase transformations, and local structures driven far from equilibrium.

Research on ion-induced damage in materials is often superficially described in terms of nuclear energy deposition of a few tens of keV [displacement cascade events illustrated in Fig. 1(b)] or in terms of electronic energy deposition or ionization at much higher energies (0.1 to several GeV),<sup>43</sup> as schematically shown in Fig. 1(c). In the intermediate energy regime ( $\sim$  hundreds of keV to a few tens of MeV) most relevant for ion-beam modification, the conventional assumption, especially for metallic systems, has been that a significant amount of energy deposited into the atomic subsystem is largely absorbed by the creation of atomic displacements and the energy transferred to the electronic subsystem is ultimately dissipated by nondamaging mechanisms. Therefore, the intrinsically spatially and temporally coupled nuclear and electronic energy dissipation processes [Fig. 1(d)] are

often incorrectly considered as uncorrelated. In other words, even though energy depositions into the electronic and atomic subsystems are coupled in both time and space, the subsequent energy dissipation processes are often mistakenly considered separately and the electronic energy is assumed to be dissipated either fully in the electronic structure or through an inelastic thermal spike often presumed to have little effect on atomic defect production and evolution.

The assumption that these two mechanisms are independent and uncorrelated has been disproved in the past decade or so for ceramics.<sup>25–29,44–57</sup> Experimental work has demonstrated that swift heavy ions (SHIs) can induce annealing of pre-existing damage in ceramics.<sup>46,58–61</sup> In the MeV regime, research has shown that pre-existing disorders in SiC (>70%) can be nearly fully annealed by ions with electronic stopping powers of as low as 5–8 keV/nm.<sup>27,28,47,48</sup> For some metallic systems, researchers have shown that intense electronic excitation by SHIs leads to either defective structures and amorphization along the ion path or annihilation of pre-existing damage in pure metals<sup>62–67</sup> and, more recently, in chemically disordered complex alloys.<sup>68,69</sup> For example, in iron (Fe) metal targets irradiated with SHIs, both defect production at higher stopping powers (>40 keV/nm) and defect annihilation at lower stopping powers were reported.<sup>63</sup> Even for energies as low as a few tens of kiloelectronvolts,<sup>70–72</sup> the effects of electronic energy dissipation can be significant in cascade events, in which electronic energy loss by in-cascade ions returns via  $e\text{-}ph$  coupling, resulting in slower cooling that enhances defect recombination and surface sputtering.

Although an understanding of the effects of electronic energy loss on pre-existing damage is beginning to emerge,<sup>23,24,27–32,47–64</sup> a great deal is still unknown regarding the energy dissipation processes.<sup>73</sup> The nature of structural modifications and phase transformations depends on irradiation conditions as well as on any post-irradiation treatment. Ion irradiation studies have been conducted on various materials as a function of ion mass, energy, and temperature to understand defect production, annihilation, and evolution processes. This in turn provides a way to evaluate the separate and combined effects of electronic and nuclear energy deposition as well as its dissipation through the intertwined electronic and atomic subsystems. Research focused on advancing the understanding of coupled defect evolution and recovery over a range of irradiation conditions is gaining momentum and is beginning to reveal the underlying mechanisms from intertwined ion-induced nonequilibrium processes.

## B. Electronic energy deposition-induced athermal processes

Neutrons and charged particles (i.e., fission or radioactive decay products, cosmic radiation, ions, and electrons) interacting with a solid will produce transient irradiation-induced processes. These processes are often referred to as “athermal” because there is little or only weak dependence on temperature. Nevertheless, the processes depend on and are generally proportional to the neutron/ion flux or fission/decay rate. Specifically, energetic charged particle irradiation, owing to the large amount of energy transfer to target electrons, induces far-from-equilibrium athermal processes (i.e., inelastic thermal spikes) and radiation-enhanced diffusional processes (e.g., high defect concentrations and modified energy barriers due to the formation of charge defects and charge redistribution) that are different from thermal equilibrium conditions (e.g., annealing at high temperatures). As a

fast-moving ion loses its energy to lattice atoms ( $dE/dx_{\text{nuc}}$ ) and to electrons ( $dE/dx_{\text{ele}}$ ) of a target material, different temperatures evolve in the two subsystems. The cascade displacement event initiated by an energetic PKA created through elastic energy transfer (nuclear energy deposition,  $dE/dx_{\text{nuc}}$ ) occurs within a fraction of a picosecond (ps), followed by a transient elastic thermal spike and rapid vacancy-interstitial recombination that leaves behind a smaller number of surviving defects after a few ps.<sup>74,75</sup> The inelastic transfer of energy from incident ions, as well as PKAs and secondary recoils, to electrons in a solid via ionization (electronic energy deposition,  $dE/dx_{\text{ele}}$ )<sup>66,76</sup> creates high-energy primary electrons, often called “delta-electrons,” within a sub-femtosecond time frame. These delta electrons subsequently induce a cascade of electron-electron energy transfers resulting in intense electronic excitation and very high, radially dependent electronic temperatures ( $T_e$ ) that decrease on timescales from 10 to several hundreds of femtoseconds (fs) (Fig. 2, fs regime).<sup>77,78</sup> As  $T_e$  is much higher than the lattice temperature ( $T_a$ ), the excited electrons transfer energy to the atomic lattice through  $e\text{-}ph$  coupling, leading to a highly localized inelastic thermal spike, during which time  $T_e$  and  $T_a$  attain equilibrium. The energy transfer process ( $T_e \rightarrow T_a$ ) may last for a few ps and the increase in  $T_a$  can result in local heating, melting, and even vaporization (Fig. 2, ps regime). Energy transfer between the two subsystems occurs via  $e\text{-}ph$  interactions, depending on the local temperature difference. The subsequent melt quenching, resolidification, and annealing processes occur over ps to nanosecond (ns) timescales (Fig. 2, ns regime). Note that although a large number of atoms are

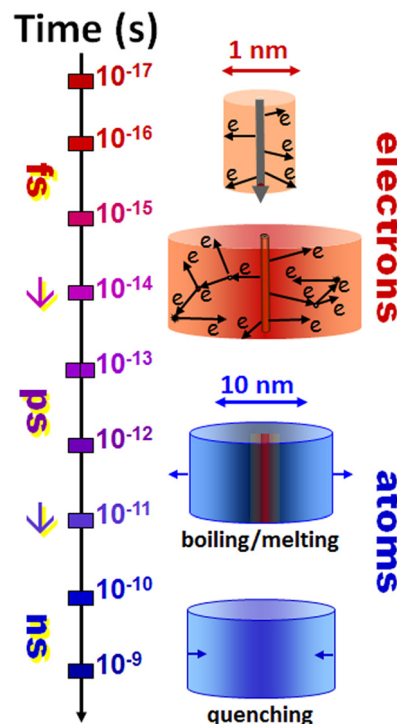


**FIG. 2.** A general description of electronic energy deposition and dissipation processes in a solid. Reproduced with permission from Zhang *et al.*, J. Mater. Res. 25, 1344 (2010). Copyright 2010 Cambridge University Press.

displaced by nuclear energy dissipation within a subpicosecond time frame and form stable defects in the ps regime,<sup>74,75</sup> subsequent thermal migration of defects occurs over much longer timescales.<sup>79</sup> Considering the timescale shown in Fig. 2, the processes associated with electronic energy dissipation are clearly coupled and interact, both in time and space, with atomic displacement processes resulting from nuclear energy dissipation.<sup>72–75</sup> While electronic energy deposition induces a highly localized thermal spike along the ion path, the associated transient processes, which occur on ps to ns time scales, drive the local structure far from equilibrium and are conceptionally different from thermal equilibrium processes.

Atomic processes from ion-solid interactions are often a consequence of the spatial and temporal coupling of atomic displacement events and energy dissipation from electronic energy loss. While atomic displacements occur via ballistic-like elastic collisions, target electrons absorb a substantial portion of the incident ion energy through inelastic energy transfer, e.g., over 90% for ions with energies over 100 keV/amu and even over 99% for many light and medium ions. The energy loss to electrons can have substantial effects on the dynamics of damage production and evolution, as the electronic energy dissipation processes interact with ballistic collision processes or accumulated defects. Furthermore, the surviving localized electronic excitations can modify migration barriers, influence bonding strengths, and even rupture bonds. These effects lead to damage production different from that described by classical molecular dynamics (MD) simulations of cascade events (i.e., from purely ballistic collision processes),<sup>23,25,32,63,68,72</sup> which completely ignore electronic energy loss and dissipation effects. The associated athermal recovery and diffusional processes, because of transient inelastic thermal spikes and localized electronic excitations that modify energy barriers, are independent of ambient sample temperature and thus are different from thermal equilibrium processes.<sup>33,80</sup>

Athermal effects have been studied in materials with covalent, ionic, metallic, and mixed bonds. A potentially large impact of electronic energy loss in nonmetallic materials is due to high electronic excitation energies and densities that create transient (tens to hundreds of ps) inelastic thermal spikes in the lattice along the ion or PKA trajectory. Such transient irradiation-induced processes are experimentally well-documented in the literature for semiconductors,<sup>27,28,30,46,48,58,59,81–83</sup> ceramics,<sup>23,29,47,49–57,60–62,69,80,84–87</sup> and metals<sup>24,32,68,88–90</sup> under neutron, fission, ion, electron, and laser irradiation. These transient processes are often referred to as athermal because they are temperature-independent or weakly dependent on temperature and cannot be described as thermally activated (e.g., some have activation energies below 0.2 eV at room temperature<sup>91</sup>) and such transient processes may precede radiation-enhanced processes occurring on longer time scales, such as those associated with the high concentration of nonequilibrium defects.<sup>83</sup> However, they are generally proportional to the neutron/ion/electron flux or fission rate. In metals, these radiation-enhanced or athermal processes are generally driven by the nonequilibrium defect concentrations produced by ballistic collisions and can lead to irradiation-induced flow stress, atomic mixing, creep, and defect recovery. While similar processes due to ballistic collisions do occur in ceramics, many of the athermal processes in ceramics are associated with ionization-induced inelastic thermal spikes or localized electronic excitations that can cause enhanced dopant displacements due to charged

defects,<sup>81,82</sup> defect production or recovery, strain relaxation, transient diffusion processes, enhanced inert gas and defect diffusion, gas resolution from bubbles, and rapid quenching of nonequilibrium phases. These athermal processes are not due to global ion or electron beam heating of the samples. They are observed at relatively low ion/electron fluxes and temperatures, where beam-induced increases in sample temperature are less than 50 K<sup>91</sup> and the corresponding thermally activated processes occur at temperatures more than 500 K higher. A few examples of ion-induced nonequilibrium conditions are discussed below to clarify athermal from thermal recovery processes.

Athermal responses have been reported in technologically important materials, such as nuclear fuel materials. For over 40 years, ionization-induced thermal spikes created by energetic fission fragments in nuclear fuel ( $\text{UO}_2$ ) have been associated with several well-known athermal processes, including enhanced diffusion of fission gas and metal cations, fission gas bubble formation, resolution of fission gas from bubbles, lattice expansion, and strain.<sup>84–86,92</sup> Recently, MD has confirmed the athermal nature of enhanced fission gas diffusion<sup>93,94</sup> and fission gas resolution<sup>95</sup> in  $\text{UO}_2$ . In the context of nuclear fuels and the transmutation of radioactive actinides, cubic  $\text{CeO}_2$  and  $\text{ZrO}_2$  have been studied as model systems—as they are isostructural with  $\text{UO}_2$ ,  $\text{ThO}_2$ , and  $\text{PuO}_2$ —to evaluate the performance of nuclear fuels and inert matrices in harsh radiation environments. The effect of electronic and nuclear energy dissipation on grain growth has been unambiguously observed in nanocrystalline oxides in  $\text{ZrO}_2$ <sup>96,97</sup> and  $\text{CeO}_2$ <sup>98,99</sup> under ion irradiation at 160–400 K. Moreover, slower grain growth has been observed in  $\text{ZrO}_2$  under 400 K irradiation than under 160 K irradiation. This somewhat unexpected finding is attributed to the difference in stable oxygen vacancies at different temperatures:  $\text{V}^0$  at 400 K vs  $\text{V}^{2-}$  and  $\text{V}^-$  at 160 K.<sup>97</sup> As the negatively charged oxygen vacancies are not thermodynamically stable at elevated temperatures, they do not contribute to grain growth at 400 K. The studies<sup>96,97</sup> indicate that the observed grain growth is not thermally activated, which would require annealing temperatures greater than 1300 K<sup>100</sup> and athermal grain growth due to the additive or combined effects of electronic and nuclear energy loss is the dominant mechanism.<sup>98</sup>

Athermal responses have been reported for many ion-irradiated and electron-irradiated complex oxides, such as  $\text{SrTiO}_3$ ,  $\text{Sr}_2\text{Nd}_8(\text{SiO}_4)_6\text{O}_2$ , and  $\text{Ca}_2\text{La}_8(\text{SiO}_4)_6\text{O}_2$ .<sup>91,101,102</sup> To unravel the inherently coupled electronic and atomic energy dissipation processes, studies of ionization-enhanced damage recovery and recrystallization have been performed under e-beam irradiation.<sup>91,101,102</sup> In  $\text{SrTiO}_3$ , ionization-induced recrystallization of a region pre-amorphized by 1 MeV Au ions is observed below 400 K under different e-beam fluxes, and the recrystallization rate is quantified via the epitaxial regrowth rate at the amorphous/crystalline (a/c) interface, as summarized in Fig. 3. The activation energy determined for the athermal recrystallization process is  $\sim 0.10$  eV, much lower than the activation energy of  $\geq 0.8$  eV for thermal recovery processes (shaded region in Fig. 3). Under 200 keV electron-beam irradiation, the ionization-induced recrystallization rate is orders of magnitude higher than the thermal growth rate from 300 to 400 K.<sup>91</sup> The rapid athermal recrystallization is attributed to localized electronic excitations that lower the energy barriers for rearrangement of interfacial atoms. While thermal recrystallization occurs above 780 K for  $\text{Sr}_2\text{Nd}_8(\text{SiO}_4)_6\text{O}_2$ , ionization-enhanced recrystallization of amorphous  $\text{Sr}_2\text{Nd}_8(\text{SiO}_4)_6\text{O}_2$  is observed at 300 K under 200 keV e-beam irradiation, where a 200 nm

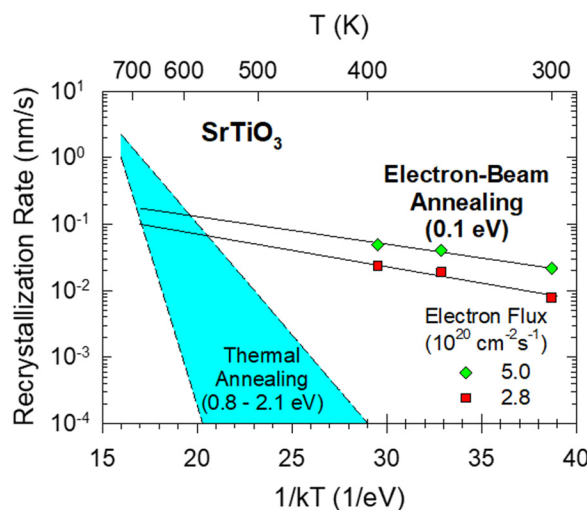


FIG. 3. Comparison of thermal and athermal (e-beam-induced) recrystallization in  $\text{SrTiO}_3$ .

pre-amorphized layer is fully recrystallized in 60 minutes.<sup>101</sup> In  $\text{Ca}_2\text{La}_8(\text{SiO}_4)_6\text{O}_2$ , post-irradiation examination of the damaged atomic structure with 200 keV focused e-beam at 300 K reveals ionization-induced recrystallization of a cascade-induced amorphous domain, as shown by the transmission electron microscopy (TEM) images in Fig. 4.<sup>102</sup>

MAX ( $M_{n+1}AX_n$ ) phases are considered as potential candidate structural materials because of their nanolamellar crystalline structure and unique thermophysical properties.<sup>103</sup> For applications in hostile high-temperature and radiation environments, ion beams have been used to simulate damage created by neutrons and to evaluate material responses to electronic excitation and ionization effects. Research has shown that the MAX phase,  $\text{Ti}_3\text{SiC}_2$ , exhibits a threshold in electronic energy loss ( $\sim 4 \text{ keV/nm}$ ), above which there is a decrease in the a/c ratio of the lattice parameters and an increase in the TiC concentration with increasing  $dE/dx_{\text{ele}}$ .<sup>103</sup> Since the changes are independent of the damage dose, the work suggests that inelastic energy dissipation should be considered together with  $dE/dx_{\text{nucl}}$  in understanding material response to ion irradiation.

Thermally enhanced processes can be minimized by carrying out irradiation at cryogenic temperatures. Damage structures produced in nickel metal by heavy-ion irradiation with Kr and Ni ions in the 50–100 keV regime have been experimentally characterized under irradiation at 30 and 300 K using *in situ* electron microscopy and the observed structures are consistent with MD simulations.<sup>104</sup> Experimental evidence shows that dislocation loops can form in isolated displacement cascades at both temperatures. Since vacancies and interstitials are believed to be immobile at 30 K (i.e., long-range thermal migration of defects is not possible), direct loop formation, coalescence of existing loops, and the annihilation/reformation of loops under continued irradiation are attributed to the athermal local relaxation within the displacement cascades revealed from the MD simulation. On the other hand, additional loops form when the 30 K irradiated samples are warmed up to room temperature, which is clearly a result of thermally activated diffusion with increasing

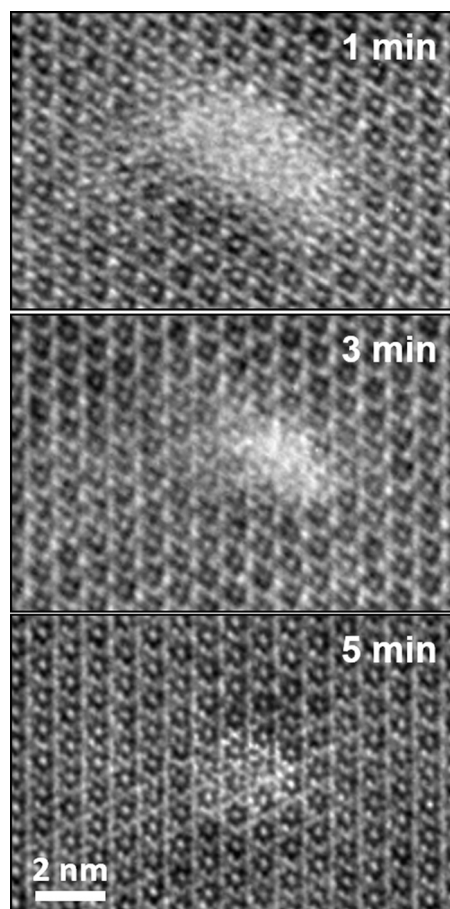
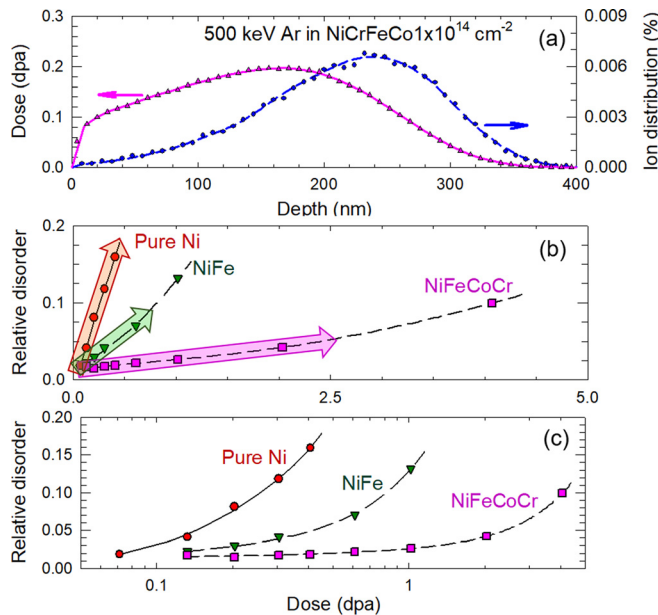


FIG. 4. TEM images showing the continuous recrystallization of a damaged region in  $\text{Ca}_2\text{Nd}_8(\text{SiO}_4)_6\text{O}_2$  under e-beam irradiation. Reproduced with permission from L. M. Wang and W. J. Weber, Philos. Mag. A **79**, 237–253 (1999). Copyright 1999 Taylor & Francis Group.

temperature, so that small defects at 30 K, not visible under the microscope, grow into visible loops.

This athermal effect has been discussed in a more recent study of concentrated solid solution alloys (CSAs).<sup>80</sup> Employing ion irradiation and *in situ* Rutherford backscattering spectrometry (RBS) along a channeling direction, an experimental investigation has been carried out at 16 K to understand early stage damage accumulation (Fig. 5) under 500 keV Ar ion bombardment. The profiles of displacement damage dose (in displacements per atom, dpa) and the injected Ar concentration in NiFeCoCr, as shown in Fig. 5(a), have been recalculated using the SRIM code in the full-cascade mode.<sup>34,35</sup> The experimentally determined density of the alloy ( $8.1435 \text{ g cm}^{-3}$ ) is used and the threshold displacement energies for all the elements are assumed to be 40 eV.<sup>105</sup> The increase in Ar-induced disorder at the damage peak with increasing dose is shown in Figs. 5(b) and 5(c). At lower doses, the damage accumulation exhibits a linear dependence on dose, as indicated by the three transparent arrows for pure Ni and the two alloys [Fig. 5(b)], up to 0.5, 0.7, and 2.5 dpa for Ni, NiFe, and NiFeCoCr, respectively. Such a linear dependence suggests little



**FIG. 5.** (a) SRIM-predicted damage profile (left axis) and implanted Ar concentration (right axis) in NiFeCoCr irradiated with 500 keV Ar at 16 K to  $1 \times 10^{14} \text{ cm}^{-2}$  at 5° off the surface normal, based on full-cascade TRIM simulations. Irradiation-induced peak disorder as a function of corresponding dose at  $\sim 170 \text{ nm}$  is shown in (b) and (c) on log and linear scales, respectively.

overlapping of defect production from incident ions. With further increases in dose, a superlinear dependence is observed. As the long-range thermal migration of vacancies and interstitials at 16 K is believed to be inefficient, the enhanced damage production results from overlapping ion damage. The results shown in Fig. 5 are in agreement with the previous conclusion regarding athermal defect interactions within displacement cascades at 30 K revealed from MD simulations and *in situ* transmission electron microscopy (TEM) observations.<sup>104</sup> The doses of 0.5, 0.7, and 2.5 dpa are equivalent to ion fluences of 2.5, 3.4, and  $12 \times 10^{14} \text{ cm}^{-2}$ , respectively, and the results shown in Figs. 5(b) and 5(c) reveal that the damage cross section for 500 keV Ar ions ranges from  $0.4 \text{ nm}^2$  in Ni to  $0.08 \text{ nm}^2$  in NiFeCoCr, supporting the early study of very small defect clusters invisible under electron microscopy.<sup>104</sup> Moreover, the range of dose values over which linearity is observed [Fig. 5(b)] for Ni, NiFe, and NiFeCoCr further illustrates the significant reduction in production of extended defect clusters with increasing alloy chemical complexity.<sup>24,106–108</sup> The significant difference in defect accumulation response shown in Fig. 5 is attributed to the more substantial impact of both elastic and inelastic thermal spikes in the alloys<sup>72,106,107</sup> arising from their intrinsic properties of decrease in thermal conductivity and increase in *e-ph* coupling<sup>24,109</sup> discussed in more detail in Sec. V.

The linear dependence of damage accumulation with increasing dose is also observed in NiCoCr under room-temperature irradiation, while sublinear dependency is evident at higher doses in Ni, as shown in Fig. 6.<sup>108</sup> The local damage dose in dpa has been determined based on the SRIM code in full cascade mode.<sup>34,35</sup> The linear dependence of NiFe and NiFeCoCr at 16 K (Fig. 5) and NiCoCr at 300 K (Fig. 6) suggests insignificant thermal migration in these CSAs at corresponding

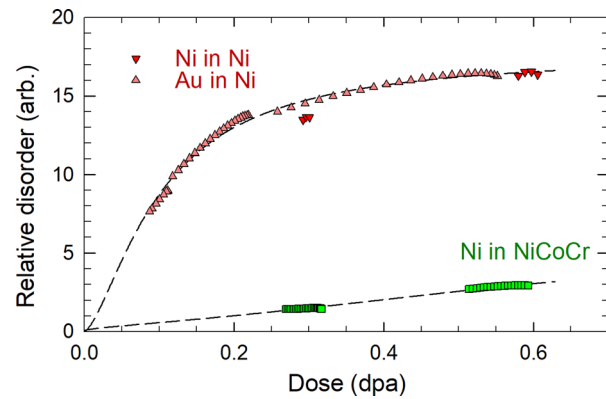


**FIG. 6.** Relative disorder in the model systems investigated under 1.5 MeV Ni and 3 MeV Au irradiations at room temperature. The dashed lines are curve fits to the data. Reproduced with permission from Granberg *et al.*, Phys. Rev. Lett. **116**, 135504 (2016). Copyright 2016 American Physical Society.

temperatures, which is consistent with MD simulations.<sup>90</sup> Given the much longer time intervals between the cascades in the experiments, compared with the MD simulations of overlapping cascades every 30 ps, the agreement between simulated and experimental spectra<sup>90</sup> on the relative trend in damage accumulation for Ni and NiCoCr suggests that thermal annealing processes do not play an important role in the accumulation of radiation damage in these alloys at room temperature. The authors<sup>90</sup> further point out that the dominant process for damage evolution in complex CSAs is athermal. Their modeling study in Ni and CSAs suggests that an irradiation-induced overlap of cascades with pre-existing damage leads to the production of extended defects, similar to that revealed in experiments by Robertson and co-workers.<sup>104</sup>

### C. Partitioning of electronic and atomic energy depositions from ions

To quantify the ionization-induced nonequilibrium processes that are conceptually distinct from thermal equilibrium evolution, the energy losses ( $dE/dx_{\text{nuc}}$  and  $dE/dx_{\text{ele}}$ ) and total ionization energy in a material resulting from energetic particles must be known. While there are several simulation codes,<sup>34,36–41</sup> the discussion is focused on using the SRIM code. SRIM<sup>34</sup> is widely applied to predict the ion range and concentration, as well as the displacement dose, as shown in Figs. 5 and 7. SRIM predictions depend on the input parameters. In addition to the ion mass, energy, and target composition, critical information should be reported (and referenced as appropriate)—such as the simulation mode (full-cascade or quick Kinchin–Pease calculation), target density, threshold displacement energies, and binding energies used in the simulation, even if the SRIM default values are used—so researchers can make meaningful comparisons between results obtained under the same or different irradiation conditions.<sup>35</sup>

As pointed in a recent article,<sup>35</sup> although there is no difference between Quick TRIM and full-cascade TRIM in the simulation of incident ion energy loss and implanted ion profiles using SRIM,<sup>34</sup> there is a significant difference in how the number of displacements, energy loss to electrons (i.e., ionization energy), and damage energy for the primary and secondary recoils are simulated or calculated. This is also

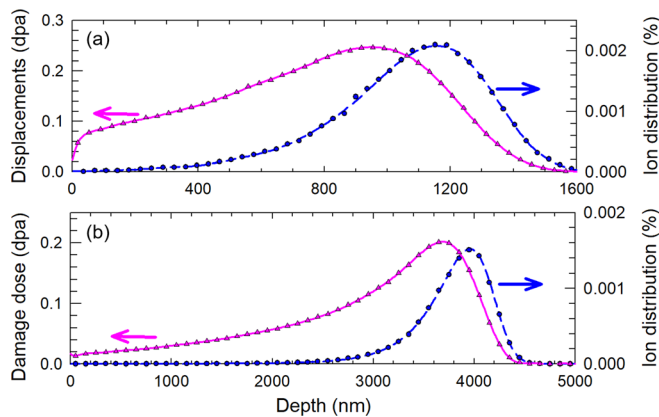


**FIG. 7.** SRIM-predicted damage dose (dpa) profile (left axis) and the injected Ni concentration (right axis) in NiCrFeCoCu under (a) 3 and (b) 23 MeV Ni irradiation to an ion fluence of  $1 \times 10^{14} \text{ cm}^{-2}$ .

true for the IM3D<sup>36,37</sup> and Iradina codes.<sup>39,40</sup> The Quick calculations of damage using the modified Kinchin-Pease model or the NRT (Norgett, Robinson, and Torrens) model<sup>110</sup> are not valid for polyatomic materials<sup>35,40</sup> and should definitely not be applied for compound semiconductors, ceramics, intermetallics, and many complex alloys of transition metals from different periods having large differences in atomic mass (e.g., HfNbTiZr). As noted recently by several authors,<sup>35,40,41</sup> the inconsistency of the NRT model with full numerical integration of the energy partitioning processes and with the self-consistent full-cascade results from three different simulation codes (i.e., SRIM, IM3D, and Iradina) raises questions regarding the validity of the semi-empirical NRT model.

To highlight the coupled electronic and atomic energy depositions and to investigate possible subsequent ionization-induced processes, the use of SRIM is described below for the high-entropy alloy (HEA) NiCrFeCoCu for the case of incident Ni ions with two energies: 3 and 23 MeV. In these calculations, a density of  $8.356 \text{ g cm}^{-3}$  is used for this equiatomic HEA.<sup>111</sup> Threshold displacement energies of 40 eV are used for all the elements.<sup>105</sup> The predicted damage dose (dpa) profiles and the implanted Ni ion distributions for a fluence of  $1 \times 10^{14} \text{ cm}^{-2}$  are shown in Fig. 7.

The damage dose (dpa) profile based on the full-cascade option is determined from the sum of the predicted vacancy concentration (VACANCY.txt file) for all target elements (i.e., Ni, Cr, Fe, Co, and Cu from NiCrFeCoCu) plus the replacement collisions (from NOVAC.txt file). The SRIM-predicted average incident ion range, implanted ion concentration peak location, and average straggling are  $\sim 1055$ ,  $1155$ , and  $245$  nm for 3 MeV Ni and  $3754$ ,  $3960$ , and  $396$  nm for 23 MeV Ni. Average range and average straggling are two of the four statistical moments: range, straggling, skewness, and kurtosis that describe the shapes of distributions; the values are provided in the RANGE.txt file. The average range ( $R_p$ ), also called the mean range, projected range, or mean projected range, is the average depth at which incident ions of energy  $E$  will come to rest. Average straggling is the variance in the locations of a set of implanted ions, which provides the appearance of the distribution. While the peak ion location is the most probable depth at which incident ions of energy  $E$  will come to rest, it can be shallower or deeper than  $R_p$  for low or high ion energies, i.e., when the

ion distribution has a positive or negative skewness. Greater straggling (396 nm vs 245 nm) is expected for high-energy ions largely because of the higher number of stochastic elastic collisions along the ion trajectories. For the same ion fluence, additional collisions and greater straggling along deeper penetration depths due to higher-energy ions can lead to somewhat lower numbers of displaced atoms at the damage peak than are produced by lower-energy ions. As can be seen in the damage dose (dpa) profile in Fig. 7, for a fluence of  $1 \times 10^{14} \text{ cm}^{-2}$ , a lower maximum damage dose and relatively broader dose profile are predicted for 23 MeV Ni than for 3 MeV Ni. The corresponding damage dose values are 0.249 dpa at 940 nm with a full width at half maximum (FWHM) of 895 nm for the 3 MeV Ni ions, but 0.201 dpa at 3690 nm with a FWHM of 1290 nm for the 23 MeV Ni ions.

SRIM is also used to estimate the partitioning of ion energy loss along the ion trajectory in materials, as illustrated in Fig. 8. The average electronic and nuclear energy losses ( $dE/dx_{\text{ele}}$  and  $dE/dx_{\text{nuc}}$ ) per unit of depth (not unit of path length, as in actual stopping powers) for incident ions of a given energy as a function of depth are determined using IONIZ.txt and E2RECOIL.txt files from full-cascade SRIM simulations. The values of  $dE/dx_{\text{ele}}$  (diamonds) are from the “IONIZ. by IONS” column in the IONIZ.txt file. The values of  $dE/dx_{\text{nuc}}$  (triangles) are the sum of “Energy Absorbed by” Ni, Cr, Fe, Co, and Cu at each depth from the E2RECOIL.txt file. This is identical to the “Energy from Ions” column if, and only if, the binding energy is set to zero for all elements in the target; otherwise, the Energy from Ions is reduced by the binding energies of the primary recoils. The

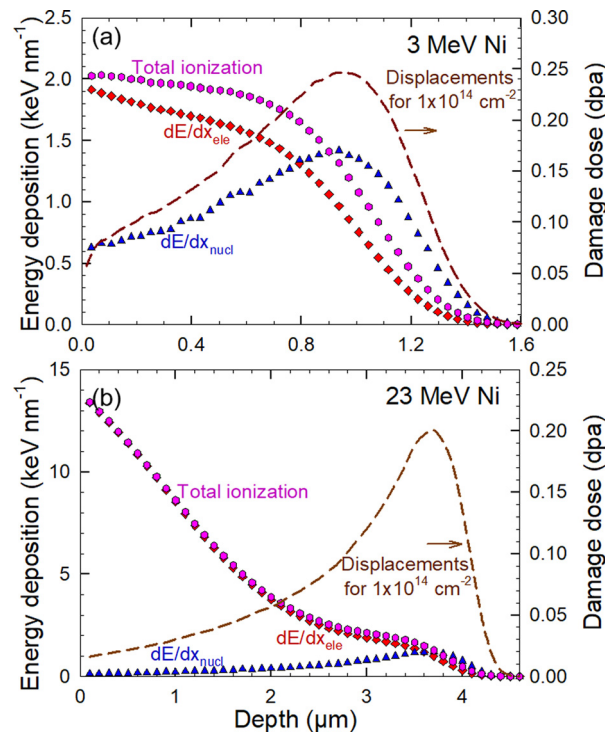


**FIG. 8.** SRIM predicted energy deposition per ion (left axis) and damage profile for an ion fluence of  $1 \times 10^{14} \text{ cm}^{-2}$  (right axis) in NiCrFeCoCu under (a) 3 and (b) 23 MeV Ni ion irradiation.

total ionization energy per unit of depth is the sum of all the energy transferred to target electrons and is determined from the IONIZ.txt by summing “IONIZ. by IONS” and “IONIZ. by RECOILS” together. The sum is clearly larger than the values of  $dE/dx_{\text{nuc}}$  over much of the depth and is comparable to or larger than  $dE/dx_{\text{nuc}}$  before the damage peak. Note that the unit keV/nm is used in Fig. 8 (left axis), and the values are per ion and independent of ion fluence.

It is also worthwhile to compare  $dE/dx_{\text{nuc}}$ ,  $dE/dx_{\text{ele}}$ , and total ionization at a depth of about 0.92  $\mu\text{m}$  in Fig. 8(a), where  $dE/dx_{\text{nuc}}$  reaches a maximum. At this depth, the average Ni ion energy is reduced to about 170 keV. The conventional belief is that, at low energies (10 to several 100 keV) where nuclear stopping is peaked ( $\sim 1 \text{ keV/amu}$ ) and maximized collision energy transfer occurs,  $dE/dx_{\text{ele}}$  may be negligible. This is an incorrect assumption, as clearly reflected in Fig. 8(a), where the curves of  $dE/dx_{\text{nuc}}$  and total ionization crossover. While the average energy loss by the incident ions via elastic nuclear collisions is higher (1.43 keV/nm) than via ionization (1.01 keV/nm), the total ionization (i.e., energy loss to electrons by the incident ion and all primary and secondary recoils) has a value of 1.36 keV/nm, which is comparable to  $dE/dx_{\text{nuc}}$ . A purely elastic nuclear collision regime does not exist and the ratio of electronic to nuclear energy losses ( $S_e/S_n$ ) or total ionization to nuclear energy losses is not negligible.

For understanding ionization-induced effects in materials, a comparison between the ionization energies and the damage energy may be an even more useful criterion. The damage energy can be calculated from the PHONON.txt file by adding “PHONONS by ION” and “PHONONS by RECOILS,” as described elsewhere.<sup>35,112</sup> Comparisons of the predicted average deposited ionization energies by incident ions (Ionization<sub>Ions</sub>), by recoils (Ionization<sub>Recoils</sub>), and by total ionization with the damage energy are shown in Figs. 9(a) and 9(b) for 3 and 23 MeV Ni in NiCrFeCoCu and in Figs. 10(a) and 10(b) for

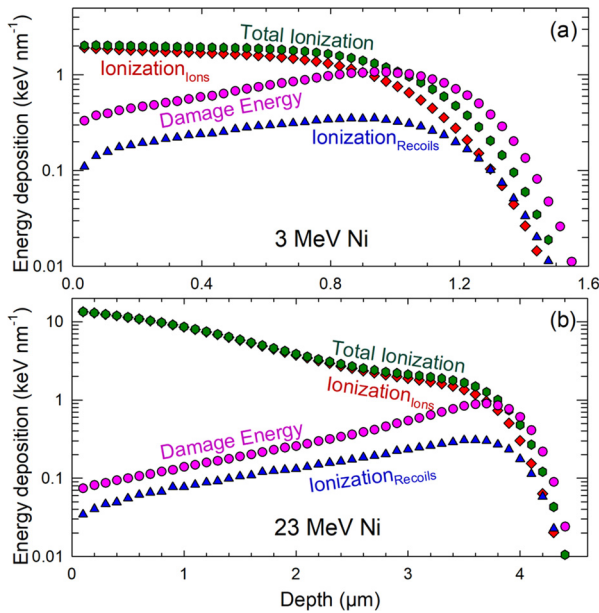


**FIG. 9.** Comparisons of full-cascade SRIM predicted ionization energies (by ions, by recoils, and total ionization) with the damage energy for (a) 3 and (b) 23 MeV Ni in NiCrFeCoCu.

5 MeV Si in SiC and 5 MeV Ni in Ni, respectively. Depending on ion-target combination and ion energies, the total ionization can be orders of magnitude higher than the damage energy [Figs. 9(b) and 10(a)]. In all four examples, the damage energy is compared directly with ionization by recoils. For 5 MeV Si ions in SiC, the ionization by recoils is higher than the damage energy at depths up to  $\sim 1900$  nm. In metals and alloys, the ionization by recoils is often lower ( $\sim 30\%-55\%$ ), but it is not negligible. Since  $dE/dx_{\text{nuc}}$  includes the ionization loss by recoils, the comparison of total ionization with damage energy provides a more useful comparison. The ratio of total ionization to damage energy has no units and is independent of any controversies about how displacements are calculated;<sup>35,41</sup> thus, it could be something both the ion beam and nuclear communities could embrace without controversy.

#### D. Modeling effects of electronic and damage energy dissipation on defects

Understanding and modeling the responses of defects and materials to ionization energy dissipation, damage energy dissipation, or the temporal and spatial coupling of ionization and damage energy dissipation processes are challenging. In this section, electronic and

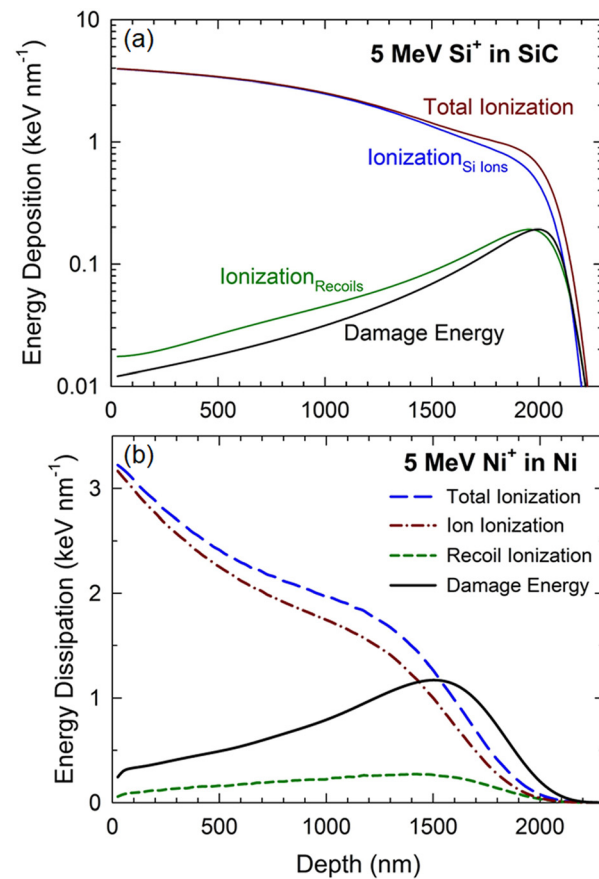


**FIG. 10.** SRIM-predicted ionization energies and damage energy for (a) 5 MeV Si in SiC and (b) 5 MeV Ni in Ni.

atomistic modeling approaches to address separate and coupled energy dissipation processes are reviewed.

### 1. Low energies

In the low-energy regime (below 200 keV), the length and time scales of ion–solid interactions are well suited for study by computer simulation techniques. Simulations of single ion–solid radiation events in ceramics have traditionally been driven by classical MD simulations based on screened empirical interatomic potentials; however, the realism and accuracy of the potentials, developed by fitting to lattice constants and elastic constants at equilibrium, are limited. *Ab initio* MD (AIMD) can play an important role in describing defect kinetics and in understanding the coupling of electronic and atomic dynamics where empirical interatomic potentials are not available for MD simulations.<sup>113–115</sup> AIMD is a unified approach for *ab initio* and classical MD. The basic idea underlying the AIMD method is to compute the forces acting on the nuclei from electronic structure calculations that are performed on-the-fly as the MD trajectory is generated. In this way, it overcomes their respective shortcomings, as the electronic variables are not integrated out beforehand but are considered as active degrees of freedom. This approach implies that, given a suitable approximate solution of the many-electron problem, chemically complex systems can be handled by MD. However, it also implies that the approximation is shifted from the level of selecting the model potential to the level of selecting a particular approximation for solving the Schrödinger equations. The dynamic processes of low-energy ion interactions can be well described, and many properties, such as the changes in bonding characteristic and electron distribution that occur during ion–solid interactions, threshold displacement energies, and migration energies, can be provided with *ab initio* accuracy.

A major computational challenge to be undertaken is to directly simulate defect generation due to displacement cascades. The Spanish Initiative for Electronic Simulations with Thousands of Atoms (SIESTA) code<sup>113</sup> is a package that includes an original method and software implementation for performing electronic structure calculations and AIMD simulations of molecules and solids. SIESTA uses a density functional theory (DFT) code that predicts the physical properties of a collection of atoms. With current computer power, it is possible to simulate low-energy displacement cascades (100 eV–1 keV) in some covalent and ionic materials using SIESTA with a few thousand atoms, and to observe charge transfer in low-energy irradiation events. As computational speed and code performance improve, it is expected that higher-energy displacement cascades will be attainable using the AIMD method.

AIMD methods have been used to investigate atomic displacement processes, charge exchange during the collision process, charge redistribution around defects, and stable interstitial configurations due to low-energy recoil events in a broad range of materials, as well as defect migration and effects of highly ionized states. The coupled electronic and nuclear radiation damage processes at low energies in GaN,<sup>116</sup> SiC,<sup>117</sup> and Y<sub>2</sub>Ti<sub>2</sub>O<sub>7</sub><sup>118</sup> have been investigated. AIMD has revealed the formation of stable defect configurations that are not predicted by MD simulations using fixed charge potentials, and has shed light on the influence of charge transfer on defect dynamics. As demonstrated in the case of Y<sub>2</sub>Ti<sub>2</sub>O<sub>7</sub>,<sup>118</sup> AIMD has identified interstitial configurations stabilized by charge redistribution/bonding changes

that had not been previously considered, and identified phase changes due to electronic excitation.

MD simulations of defect production by energetic ions in ceramics have generally included only nuclear stopping; electronic effects are not well-represented, and charge transfer and charge-density redistribution are ignored. To improve the predictive power of cascade simulations, electronic energy loss must be included. The DL-POLY code is a general-purpose serial and parallel MD simulation software developed and maintained at Daresbury Laboratory.<sup>119</sup> The current version, DL\_POLY 4, is based on domain decomposition to achieve parallelism allowing for simulations of millions of atoms on high processor counts.<sup>120</sup> This code is highly scalable and recent developments have demonstrated  $500 \times 10^6$  atom simulations of high-energy cascades (>200 keV) with local heating from electronic stopping. Large-Scale Atomic/Molecular Massively Parallel Simulator (LAMMPS) is a classical MD code.<sup>121</sup> LAMMPS is distributed as an open source code under the terms of a general public license by Sandia National Laboratories. The PARCAS code is a large-scale parallel MD code developed at the University of Helsinki.<sup>122</sup> In low-energy ion events, the loss of energy to electrons leads to reduced energy for damage production, cascades of electron-to-electron kinetic energy transfers, the thermalization and diffusion of electrons, and the transfer of this electronic energy back to the atomic lattice via *e-ph* coupling. Under these conditions, classical MD simulations with appropriate partitioning of energy loss to electrons as a friction force (i.e., the electronic stopping force) and energy feedback to the atoms via *e-ph* coupling, as described by a two-temperature model (TTM), are more physically accurate and comparable to experimental results. Including the effects of electronic stopping in MD simulations based on a two-temperature model approach was initially described by Duffy and Rutherford,<sup>70,123</sup> and this two-temperature MD (2T-MD) model has been implemented in DL-POLY, as described in detail recently.<sup>120,124</sup> A similar 2 T-MD model approach has been implemented in PARCAS<sup>125</sup> and LAMMPS.<sup>126,127</sup> More recently, electronic stopping power and *e-ph* coupling have been included in the computationally efficient MDPSCU code,<sup>128</sup> which is a graphic processing unit-accelerated MD package. The algorithms in the 2T-MD model were derived for metallic systems, and unfortunately their applicability for semiconductors and insulators has not been validated.

### 2. Intermediate energies

In the intermediate energy regime (several hundred keV up to several tens of MeV), both nuclear and electronic energy losses are significant. Classical MD simulations are limited by computational resources in describing cascades initiated by ions over several hundreds of keV. DL\_POLY has been employed to investigate uranium cascades up to 500 keV, with electronic stopping included as a friction term, in ZrO<sub>2</sub>,<sup>129</sup> and 300 keV self-ion cascades in tungsten with electronic stopping and *e-ph* coupling included (2T-MD approach).<sup>130</sup> The computational cost of such high-energy cascades can be reduced using the Cell Molecular Dynamics for Cascade (CMDc) code recently developed by Crocombe that adds and removes small simulation cells on-the-fly,<sup>131</sup> but this code is still under development and does not include *e-ph* coupling.

Although there have been few, if any, systematic evaluations of materials, possible ionization effects on defect production, defect recovery, and structural modification have been explored using an inelastic thermal spike model based on the two-temperature model (TTM).<sup>70,123,132</sup> It is used to introduce a thermal spike along an ion trajectory in the absence of collisional processes from the damage energy, or to superimpose a thermal spike on the collision cascade processes along an ion trajectory to simulate coupled electronic and atomic dissipation processes. In the TTM approach, energy deposition and dissipation in the electronic subsystem are described via a heat diffusion equation. The heat flow in the electronic system is dependent on its heat capacity, thermal conductivity, *e-ph* coupling, and energy deposition from an external radiation source. The coupled heat flow between the electronic and atomic subsystems can be provided by the continuum TTM, which is described by two coupled differential equations:

$$C_e(T_e) \frac{\partial T_e}{\partial t} = \frac{1}{r} \frac{\partial}{\partial r} \left[ r K_e(T_e) \frac{\partial T_e}{\partial r} \right] - g(T_e - T_a) + Q(r, t) \quad (1)$$

and

$$C_a(T_a) \frac{\partial T_a}{\partial t} = \frac{1}{r} \frac{\partial}{\partial r} \left[ r K_a(T_a) \frac{\partial T_a}{\partial r} \right] + g(T_e - T_a), \quad (2)$$

where  $T_e$ ,  $C_e$  and  $K_e$  and  $T_a$ ,  $C_a$  and  $K_a$  are the temperature, heat capacity, and thermal conductivity of the electronic and atomic subsystems, respectively;  $g$  is the *e-ph* coupling strength; and  $Q(r, t)$  is the energy distribution transferred to electrons by the ions, i.e., an athermal energy source.<sup>133–135</sup> Using Monte Carlo or numerical descriptions of the electronic energy deposition profile and the continuum TTM, energy transfer to the atomic system can be determined and used as input to MD simulations for describing the materials response to ion irradiation.<sup>27,136–138</sup> The coupling effects can also be investigated by a more advanced TTM approach, the 2T-MD model that includes *e-ph* coupling directly in MD simulations.<sup>25,139–141</sup> The more sophisticated 2T-MD model includes the electronic energy dissipation from the ion and directly couples it explicitly to the atomic lattice within MD.

The radial temperature profiles in pristine (undamaged) and pre-damaged  $\text{SrTiO}_3$  at different times have been calculated from the inelastic TTM for 21 MeV Ni ions,<sup>142</sup> as illustrated in Fig. 11. The corresponding energy deposition profiles used within MD simulations are illustrated in Fig. 12. The mean free path (MFP) ( $\lambda$ ) in ceramics is generally estimated from an experimentally derived relationship with the bandgap.<sup>143,144</sup> While the *e-ph* coupling parameter ( $g$ ) can be calculated from *ab initio* methods for metals and alloys,<sup>145,146</sup> it has not been calculated for ceramics. Nevertheless, using pump-probe reflectivity measurements with ultrafast laser pulses, as in the case of metals,<sup>145</sup> it may be possible to determine  $\lambda$  or  $g$  experimentally. The specific heat coefficient ( $C_e$ ) and the thermal conductivity ( $K_e$ ) for electrons can be estimated by assuming that hot electrons in the conduction band of a ceramic behave like hot electrons in a metal with a constant excited electron density.<sup>143</sup> Recently, the effect of the transient electron density on the conduction band has been considered in an electron-density-dependent TTM for dielectrics,<sup>147</sup> which suggests an extended heating time compared with the regular TTM. As described previously in the TTM case in which there is sufficient

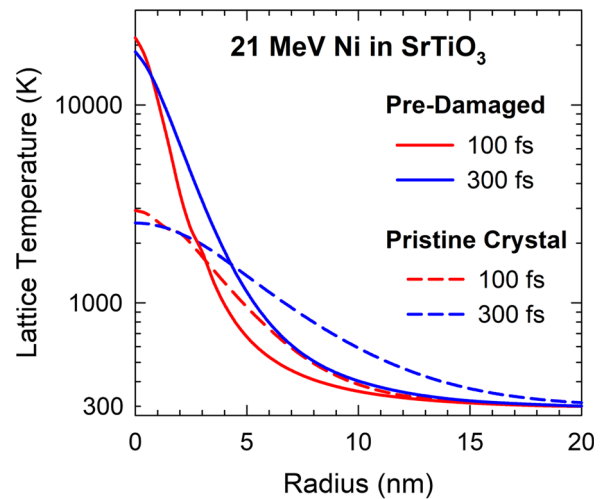


**FIG. 11.** Spatial and temporal evolution of temperature based on the two-temperature model for 21 MeV Ni ions in pristine (undamaged) and pre-damaged (1.5% defects)  $\text{SrTiO}_3$ . Reproduced with permission from Weber *et al.*, Sci. Rep. **5**, 7726 (2015). Copyright 2015, Authors, licensed under a Creative Commons Attribution-NonCommercial-ShareAlike 4.0 International License.

nuclear energy loss to produce defects, the inelastic thermal spike induced by electronic energy loss can be superimposed on the collision cascade process along the associated ion path incrementally.<sup>136,137</sup> Since the transfer of energy from incident ions to electrons and atomic recoils occur simultaneously, the thermal spike is normally delayed by 100–500 ps to account for the maximum heating (see Figs. 2 and 11).

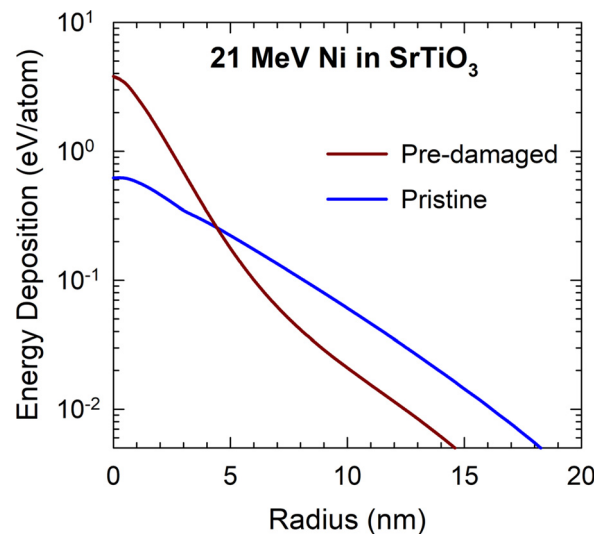


**FIG. 12.** Radial energy deposition profiles for 21 MeV Ni ions in pristine (no damage) and pre-damaged (1.5% defects)  $\text{SrTiO}_3$ . Reproduced with permission from Weber, *et al.*, Sci. Rep. **5**, 7726 (2015). Copyright 2015, Authors licensed under a Creative Commons Attribution-NonCommercial-ShareAlike 4.0 International License.

### 3. High energies

In the high-energy regime ( $\geq 1$  MeV/amu, or from 100 MeV to several GeV), heavy ions created by high-energy particle accelerators are usually referred to as swift heavy ions (SHIs), and they are often used to study fission-particle damage and cosmic ray interactions. They are also used to create novel and unique structures on nanoscale dimensions for a wide range of applications in various fields, such as sensor technology, molecular biology, and biomedicine. The extreme energy deposition for SHIs is highly localized and is transferred almost entirely to electrons over much of their track length [Fig. 1(c)]. The advantages and sometimes unique properties of nanoscale ion track structures are related to their large length-to-diameter ratios and to the ability to control and manipulate their number density, shape, length, and diameter. There is, however, still a substantial need for a better understanding of the physical processes involved in track formation.

SHI track formation in both insulators and metallic materials has been described as a consequence of pure electronic stopping using an inelastic thermal spike formalism based on the TTM, Eqs. (1) and (2), where nuclear collisions are neglected. As noted by Sigmund,<sup>148</sup> damage production by ions in this purely electronic energy loss regime is very complex. SHIs transfer energy to the loosely bound electrons of the solid, thus initiating a cascade of secondary electrons and generating a radial distribution of  $e-h$  pairs over about a 0.1 ps timescale (Fig. 2). After this time, the energy is transferred to atoms via  $e-ph$  coupling that creates an inelastic thermal spike several nm in diameter (Fig. 2); the spike can cause structural modifications via melt-quenching and recrystallization processes. The inelastic thermal spike model is an analytical model that considers evolution of different stages of ion-solid interaction: energy deposited to electrons,  $e-ph$  coupling, local melting, and quenching, where the energy deposited to the electrons is transferred to the lattice atoms via electron-electron and  $e-ph$  interactions. In other words, the model describes the energy transfer and  $e-ph$  coupling processes and the spatial distribution of thermal energy transferred to the atomic structure. Using the inelastic

thermal spike model, it is possible to describe the velocity effect, in which different track radii result from the same electronic energy loss on both sides of the Bragg stopping peak. This is because, for the same electronic energy loss, the energy deposited to electrons at a lower ion velocity leads to more efficient energy transfer to lattice atoms and consequently larger track radii. This velocity effect provides an important benchmark for developing and validating computational models of track formation. For semiconductors<sup>149,150</sup> and ceramics,<sup>54,125,151,152</sup> MD simulations based on the inelastic thermal spike model reveal radial structures of SHI tracks that are in excellent agreement with experimentally determined track sizes, concentric shell structures, local strains, and atomic arrangements (e.g., crystalline and amorphous structures), as illustrated in Fig. 13 for  $Gd_2TiZrO_7$  irradiated with 2.3 GeV  $^{208}Pb$  ions. Similarly, MD simulations of defect formation in complex alloys due to SHI are consistent with experimental observations.<sup>68</sup> The distribution of energy dissipation from such analytical models can be incorporated directly within MD environments to simulate thermal spikes and investigate the time evolution of the complex structural changes that occur as this electronic energy is dissipated.

In summary, the methodology to include electronic stopping in MD simulations provides new insights into the role of realistic damage energy densities, the effects of electronic energy dissipation on defect production, and the evolution of irradiation damage in materials susceptible to irradiation and in those that are more tolerant. The results of TTM and 2T-MD studies provide more reliable models of defect densities in displacement cascades, the occurrence of in-cascade amorphization, and the spatial extent of the cascade damage.

### E. Experimental approaches to separate and quantify effects

The dissipation of energy into the electronic system and the transfer of energy from the electronic to the atomic structure via  $e-ph$  coupling are dependent on the intensity of energy deposition and on a material's fundamental quantities (e.g., composition, structure, bandgap, bonding strength, and thermal conductivity). When energy

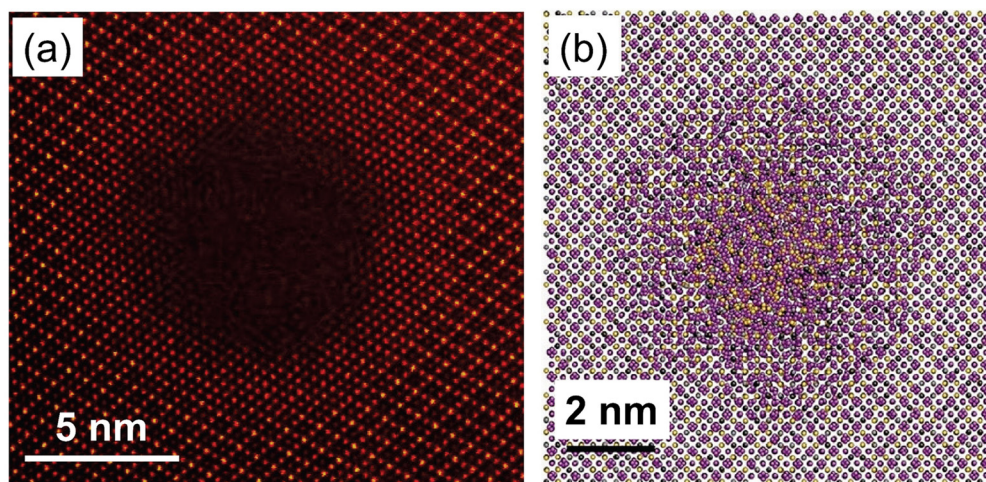


**FIG. 13.** Amorphous core and defect-fluorite shell structure of ion track in  $Gd_2TiZrO_7$  from a 2.3 GeV  $^{208}Pb$  ion: (a) high-angle annular dark field (HAADF) image and (b) MD simulation. Reproduced with permission from Sachan, et al., Sci. Rep. **6**, 27196 (2016). Copyright 2016, Authors licensed under a Creative Commons Attribution 4.0 International License.

dissipation via electronic processes is occurring simultaneously with ballistic cascade processes, e.g., at low to intermediate energies, it is challenging to separate and quantify the contributions of ionization energy and damage energy to defect production and evolution. One of the approaches successfully employed to advance this understanding is separate effects studies. In these studies, pre-existing damage with a shallow range distribution (<500 nm) is initially introduced by ions with relatively low energies via strong ballistic collisional processes. Then the separate response of the pre-existing damage to electronic energy loss is evaluated by a successive irradiation with highly ionizing ions with negligible nuclear energy loss over this shallow range. In this way, it is possible to clearly and unambiguously quantify the response to electronic energy loss as a function of pre-damage level and magnitude of the electronic energy loss. This approach is an example of sequential dual ion beam irradiation.

The sequential dual beam approach also is often used in the study of nuclear materials for which areas of interest are the behavior of fission products and helium from either alpha decay or from nuclear reactions under high radiation doses, as in the case of helium bubble formation in SiC.<sup>153</sup> Simultaneous dual-beam experiments involving low-energy and high-energy incident ions have been employed to study the dynamic synergy of nuclear and electronic energy losses in defect formation, defect structures, and phase transformations in materials.<sup>23,31,46</sup> As in the case of the sequential dual-beam approach, simultaneous dual- and triple-beam experiments are of great interest for evaluating the integrated radiation response of nuclear materials to helium, hydrogen, and damage production in fission and fusion reactor systems.

Another experimental approach to studying how ionization energy and damage energy impact defect production and evolution is performing ion irradiation along both channeling and nonchanneling directions.<sup>28</sup> Along a channeling direction, ion nuclei interactions are minimized; therefore,  $dE/dx_{\text{nuc}}$  is significantly reduced. On the other hand, the decrease in  $dE/dx_{\text{ele}}$  is limited, especially for heavy ions with large atomic numbers and radii. With a significant decrease in  $dE/dx_{\text{nuc}}$  and consequential increase in  $S_e/S_n$ , or the ratio of total ionization to damage energy, the rate of damage production is significantly reduced.<sup>28</sup> If the changes in  $dE/dx_{\text{nuc}}$  and  $dE/dx_{\text{ele}}$  along a given low-index zone axis are known, the ionization effect on damage processes can be further separated and quantified.

While energy loss to the electronic structure leads to significant  $e-h$  pair production that can result in localized electronic excitations and an inelastic thermal spike, atomic defects resulting from the nuclear energy loss may trap electrons and holes. This trapping can lead to charged defect states that can affect in-cascade recovery processes and long-range diffusion, or even can be used to probe in real time (e.g., ion beam-induced luminescence) the production or recovery of irradiation-induced defects.<sup>154,155</sup> The production of long-lived or stable localized electronic excitations from single ion events can have a dramatic effect on the longer-term collective processes that result from irradiation. Accurate descriptions and understanding of ionization processes and electronic excitation properties are essential to interpreting them and predicting their impact on the dynamics of atomic processes and overall materials' response.

Irradiation with ion beams of various mass and energies is a key technique for depositing a range of controlled energy densities in materials, and for addressing fundamental processes of energy

dissipation and defect evolution. With increasing ion energies up to ~50 keV/amu or a few tens of MeV, material responses to both nuclear and electronic energy losses must be considered. At very high energies, SHIs (above ~1 MeV/amu) are a special type of ion irradiation for which electronic stopping dominates over nuclear stopping by orders of magnitude and the ion-solid interaction can be treated as purely electronic.

### III. INTRINSIC MATERIAL PROPERTIES AND ION-INDUCED NONEQUILIBRIUM PROCESSES

Intrinsic properties of materials at the level of electrons and atoms have substantial influence on the dissipation processes for energy loss by ions, as well as on materials' responses to the energy dissipation.

#### A. Nonequilibrium defect dynamics at the level of electrons and atoms

Controlling atomic motion to suppress or control defect evolution in a nonequilibrium environment is an active research field in materials science. Ion irradiation is an effective tool to initiate a localized nonthermal equilibrium condition. A collision cascade with an accompanying pressure wave to the surrounding atoms can be viewed as an ultra-fast, nanoscale phase transition with complex thermodynamic and kinetic behavior.<sup>11</sup> Point defect clustering in dilute alloys has been shown to be primarily determined by the associated shock waves.<sup>77,78,156–159</sup> Recent cascade simulations<sup>74,158</sup> have further discovered and verified that short-range interactions of atoms have essential impacts on defect production from high-energy collisions, and the magnitude of short-range forces is a key parameter in quantitative control of primary damage production. Specifically, cascade simulations in pure Ni reveal strong forces at short distances (<2 Å) and the extreme local environment of high pressures (10–50 GPa) and high temperatures (several thousand kelvin). Broadly, nonequilibrium defect evolution can be understood in terms of close-to-equilibrium processes (solving the electron, phonon, and magnon contributions to heat conduction) and far-from-equilibrium processes (high defect concentrations and localized resolidification after a cascade event) that leave the atomic lattice largely intact but result in point defect formation. The incoherent, high-energy motion of atoms in a collision cascade modifies the transport of vacancies and constituent elements, both of which can be strongly influenced by cascade dynamics.<sup>160,161</sup>

First principles calculations show that the phonon lifetimes depend on both the mode and the polarization.<sup>77,162</sup> Longitudinal modes have shorter lifetimes than transverse modes. By accounting for the spatially correlated  $e-ph$  coupling strength and better capturing the complexity of electron-ion thermal equilibration, researchers have shown differential heating—slow for the long-wavelength mode and fast for the short-wavelength mode.<sup>77</sup>

The energy dissipation also depends on the local electronic density.<sup>163–165</sup> The coupling of ballistic processes with the electronic process (Figs. 1 and 2) due to concurrent nuclear and electronic energy dissipation from incident ions [Fig. 1(d)] has been investigated using a coupled 2T-MD model<sup>28,50,53–55,68,72,106,166</sup> and electron–phonon MD (EPH-MD) software tools,<sup>77,78</sup> both of which allow more realistic representations of the nonequilibrium defect dynamics.

Local elemental arrangements affect the properties of materials in many ways and may have a major impact on phase stability in a high-

radiation environment. More strongly coupled effects in some complex and pre-damaged ceramics (Secs. III B 1 and IV) or in chemically disordered concentrated solid solution alloys (detailed in Secs. III B 2 and V) are shown to have profound influences on defect production and damage evolution.

## B. Material intrinsic properties affecting energy dissipation at the level of electrons and atoms

For example, structural modifications, due to mechanical loading or irradiation-induced pressure waves, reflect a material's intrinsic response to an external disturbance. Understanding force mitigation or energy dissipation in materials under shock waves or ion irradiation is essential to predict and dictate the responses of materials in a non-equilibrium environment. In past decades, researchers have tried to reveal the controlling factors for structural stability under nonequilibrium irradiation conditions. This section reviews several examples of structural inhomogeneity and discusses the bonding characteristics of structural stability and the impact of chemical complexity at the electronic and atomic levels on energy dissipation.

### 1. Covalent and ionic materials

Bonding characteristics in ordered compounds depend on specific elements. Because of their importance in optoelectronics, radiation damage in III-V semiconductors has been studied extensively.<sup>167–171</sup> One intriguing question is why GaAs and InP, with very similar properties, respond so differently to intense local electronic energy deposition under SHI irradiation: GaAs exhibits very high radiation resistance, while continuous amorphous tracks form readily in InP.<sup>172</sup> The case of Al<sub>x</sub>Ga<sub>1-x</sub>As is also interesting—this compound is very susceptible to irradiation-induced amorphization from 1.7 MeV Ar ions for an aluminum content of  $x \leq 0.5$ , but it exhibits a dramatic increase in radiation resistance when the substitution of aluminum for gallium exceeds  $x = 0.75$ .<sup>173</sup> This is somewhat surprising, since adding aluminum results in no change in the crystal structure and there are no dramatic changes in the lattice constant, bandgap, or any other basic materials properties.

Cation adaptability (i.e., cation disorder) in complex compounds has been intensively investigated to understand their structural stability. It has long been observed that oxides with a similar crystal structure may be dissimilar in irradiation performance.<sup>174–176</sup> Complex ceramics with the A<sub>2</sub>B<sub>2</sub>O<sub>7</sub> composition and pyrochlore crystal structure have remarkable elemental versatility on their A or B lattice sites and significant differences in their irradiation response.<sup>175,177</sup> Cation disorder has been investigated to understand mass transfer.<sup>178</sup> Research shows that, in general, the defect-fluorite structure (disordered phase of pyrochlore) readily accommodates point defects into its lattice via lower energy barriers for cation disorder or antisite formation; whereas a structurally similar, but compositionally different, pyrochlore crystal that cannot accommodate cation antisites becomes amorphous because of the accumulation of point defects. Consequently, many pyrochlores are intrinsically more radiation sensitive than those that can accommodate cation disorder in the defect-fluorite structure. Research on cation disorder has extended to entropy-stabilized oxides,<sup>179</sup> in which one cation sublattice (e.g., the A site) has multiple random elemental substitutions, while the other cation sublattice (e.g., the B site) has a single cation species and the anion

sublattice is unchanged. Likewise, ABO<sub>3</sub> compounds with the perovskite structure exhibit a wide variation in their response to radiation.<sup>180</sup>

In addition to cation disorder, local lattice distortion is important. Pyrochlores with Ti, Nb, and Ta as major B-site cations are known to be radiation sensitive. With an increasing radius of the A-site cation, from Lu<sup>3+</sup> (0.098 nm) to Gd<sup>3+</sup> (0.106 nm), the critical temperature for amorphization under Kr<sup>+</sup> ion irradiation increases from 480 K (for Lu<sub>2</sub>Ti<sub>2</sub>O<sub>7</sub>) to 1120 K (for Gd<sub>2</sub>Ti<sub>2</sub>O<sub>7</sub>).<sup>181,182</sup> However, the critical temperature for these pyrochlore materials under heavy ion irradiation is nearly constant (1000 K).<sup>21</sup> Zirconate pyrochlores with zirconium as the B-site cation are largely radiation tolerant. For example, the crystalline structure in Gd<sub>2</sub>Zr<sub>2</sub>O<sub>7</sub> and Er<sub>2</sub>Zr<sub>2</sub>O<sub>7</sub> remains intact under extreme irradiation at cryogenic temperatures up to 100 dpa.<sup>175,183</sup> Sickafus *et al.*<sup>174</sup> suggest that the complex chemistry and structure in A<sub>2</sub>B<sub>2</sub>O<sub>7</sub> oxides with an inherent propensity to accommodate lattice distortion may resist lattice instability in an irradiation environment.

To draw attention to the bonding characteristics observed in A<sub>2</sub>B<sub>2</sub>O<sub>7</sub> materials, the correlation between bonding characteristics and the corresponding radiation performance has been analyzed by Trachenko *et al.*<sup>184</sup> in terms of the type and strength of interatomic force. They suggest that the competition between the short-range covalent and long-range ionic forces may hold the key to radiation resistance. Supporting evidence is observed for SiO<sub>2</sub>, TiO<sub>2</sub>, and GeO<sub>2</sub>. Crystalline SiO<sub>2</sub> is easily amorphizable but TiO<sub>2</sub> is more resistant than SiO<sub>2</sub> and GeO<sub>2</sub>. The underlying mechanism is attributed to the larger ionicity in the bonding of TiO<sub>2</sub> compared with SiO<sub>2</sub> and GeO<sub>2</sub>. Similarly, the binary oxides of MgO, ZrO<sub>2</sub>, and Al<sub>2</sub>O<sub>3</sub> are known to have high resistance to radiation, which is attributed to the high ionicity of these binary oxides. The results also demonstrate that complex titanates (e.g., perovskites of CaTiO<sub>3</sub>, SrTiO<sub>3</sub>, and BaTiO<sub>3</sub>, pyrochlores of Gd<sub>2</sub>Ti<sub>2</sub>O<sub>7</sub>, Sm<sub>2</sub>Ti<sub>2</sub>O<sub>7</sub>, Eu<sub>2</sub>Ti<sub>2</sub>O<sub>7</sub>, and Y<sub>2</sub>Ti<sub>2</sub>O<sub>7</sub>, and zirconolite of CaZrTi<sub>2</sub>O<sub>7</sub>) are radiation sensitive as a result of the disordered covalent fraction of Ti-O-Ti bonds. The same explanation—high ionicity of the Zr-O bond—has been used to elucidate the superior radiation performance of zirconate oxides of Gd<sub>2</sub>Zr<sub>2</sub>O<sub>7</sub>, Sm<sub>2</sub>Zr<sub>2</sub>O<sub>7</sub>, Nd<sub>2</sub>Zr<sub>2</sub>O<sub>7</sub>, Ce<sub>2</sub>Zr<sub>2</sub>O<sub>7</sub>, and Er<sub>2</sub>Zr<sub>2</sub>O<sub>7</sub>. This proposition put forward by Trachenko *et al.*<sup>184</sup> is further supported by the fact that most metals and alloys, in which metallic bonding has an even longer range, are radiation tolerant.

### 2. Metallic materials

In metals and conventional alloys, heat is conducted mainly by valence electrons. Random arrangement of multiple chemical species, as in CSAs, leads to much lower thermal electronic conductivity.<sup>24,185,186</sup> Owing to rapid heat conduction via electrons in metals and conventional alloys, ionization effects are generally thought to be negligible. In complex alloys, slow energy dissipation is expected to affect defect dynamics.

Moreover, a random arrangement of multiple elemental species is an effective way to create a maximum density of solute pinning sites per unit of volume. The atomic-level incompatibility modifies the energy landscape.<sup>24</sup> The hopping between different local minima is closely linked to both the local chemical environment and energy dissipation: a higher density of local minima is more likely to trigger cascade relaxations and thus may affect primary damage production.

Radiation-induced nonequilibrium processes in chemically disordered metallic alloys are reviewed in Sec. V.

### C. Similarities of energy dissipation in complex ceramics and chemically disordered alloys

The similarity of their atomic-level chemical complexity and site-to-site inhomogeneity is the common characteristic in complex transition-metal ceramics<sup>174,176,178</sup> and transition-metal CSAs.<sup>24,187,188</sup> The atomic-site distortions on the crystalline lattice and the effects of such disorder on bonding characteristics for a relatively simple structure are the common characteristic in single-phase CSAs (SP-CSAs), similar to complex oxides and III–V semiconductors. For example, substitutional disorder is a common phenomenon in transition-metal oxides and affects their electronic and structural properties, as well as many aspects of their materials properties, including their response to energetic ion beams.

Unlike in traditional alloys, the resulting intrinsic lattice distortion, local stress fluctuations, heterogenic strain, and variable interatomic forces are shown to have profound effects on CSA response to external forces. For example, increasing chemical complexity leads to orders-of-magnitude reductions in the electron mean free paths (MFPs) and electron and thermal conductivities of CSAs—such as NiCo, NiFe, NiPd, and NiCoFeCr—compared with Ni.<sup>24,109</sup> Compared with metals and dilute alloys, the energy exchange between the atomic and electronic subsystems in CSAs results in a smaller total number of defects and smaller clusters.<sup>72,106,166</sup> In other words, the stronger  $e\text{-}ph$  coupling and slower heat conduction in CSAs result in smaller defect clusters, whereas the larger electrical thermal conductivity in metals and chemically simple alloys results in the creation of large clusters. Research shows that the electronic configuration of transition metals affects the stability of disordered phases.<sup>187,188</sup> Studies of SP-CSAs<sup>24</sup> suggest that the chemical complexity (i.e., electronic- and atomic-level heterogeneities) can be modified via the selection of elements and their concentrations, therefore, to tailor energy dissipation pathways.

Stronger  $e\text{-}ph$  coupling is also expected in complex ceramics with high substitutional disorder. The impact of chemical disorder on material functionality, compared with the impact of cation diffusion, can be closely related to cation disorder, where high disorder allows fast vacancy-mediated diffusion.<sup>178</sup> The research effort to clarify links between these intrinsic variables and microstructural evolutions under nonequilibrium radiation conditions is just beginning.

## IV. RADIATION-INDUCED NONEQUILIBRIUM PROCESSES IN COVALENT AND IONIC MATERIALS

Normally when a material is exposed to energetic particles, such as ions, electrons, or neutrons, many defects are created, resulting in damage to the structure and property degradation. In ceramics, the primary damage state resulting from energetic cascades usually falls into one of the two categories: (1) isolated point defects and small defect clusters or (2) an amorphous (or phase-transformed) core surrounded by a cloud of point defects and defect clusters. The inelastic transfer of energy from energetic ions and electrons to target electrons in semiconductors and insulators can produce results ranging from simple ionization, as in the case of electrons, to energetically intense ionization, as in the case of ions with tens of keV to GeV energies. While all ionization leads to electron–hole production that can cause

localized electronic excitations, charged defects, and modification of local migration barriers, energetically intense ionization creates energetic delta-electrons along the ion trajectory. The delta-electrons dissipate their energy in highly localized cascades of electron–electron collisions, which significantly increase the local electronic temperature. The high energy of the electronic temperature is mostly transferred to the atomic lattice via  $e\text{-}ph$  coupling, causing a highly localized increase in the atomic temperature that is generally referred to as an inelastic thermal spike. An inelastic thermal spike along the ion path initially undergoes rapid quenching on ps time scales, which can lead to amorphization, metastable phase transitions, point defects, and local shock waves. However, reaching thermal equilibrium may require ns time scales, during which time defect and atomic mobility can be enhanced. As a consequence, electronic energy loss has significant effects on defect dynamics and damage accumulation processes.

In the past decade, experimental studies and modeling efforts have focused on characterizing such primary damage states, particularly in those materials where electronic energy deposition was long believed to have negligible or minimal effects. Understanding of the effects of electronic energy dissipation processes has been advanced by the discovery of substantial competitive effects (annealing/recovery), additive effects (additive contributions of electronic and nuclear energy dissipation to damage production and microstructural evolution), and synergistic interactions of electronic energy loss with pre-existing defects that lead to significant enhancement of damage production.

### A. Competitive effects leading to defect annealing

High electronic excitation densities often lead to damage or alteration of crystal structures; however, under certain conditions and for some materials, this energy loss also promotes recovery of pre-existing damage. For example, laser annealing of crystal damage has been observed in ion-implanted semiconductors,<sup>189</sup> in which the high-density electron plasma inside the material is thought to induce softening of the crystal lattice and defect recovery. Under ion irradiation, experimental results and atomistic simulations have revealed that energetic incident ions lose a majority of their energy in inelastic energy transfers to electrons, not in atomic collisions. The electronic energy returns to the atomic structure, via  $e\text{-}ph$  coupling, and creates a highly localized inelastic thermal spike along the ion path. This transient thermal spike, which may last for tens to hundreds of ps, can lead to local athermal recovery and relaxation of defects and structural disorder that is independent of bulk temperature. Recent research has shown that electronic energy loss from ion–solid interactions in carbides and complex oxides can promote recovery of some fraction of the defects and structural disorder created by the same ions or those existing in a pre-damaged state.<sup>23,27,28,30,31,45–48,53,56,58,59,190,191</sup> The electronic energy loss interacts competitively with ballistic collision processes or defects created by such processes, leading to decreased damage production per ion or increased athermal recovery or diffusional process that affect damage evolution. Both effects must be accounted for in predictive modeling.

One of the original studies to observe athermal recovery of radiation damage in SiC due to electronic energy dissipation was in pre-damaged 6H-SiC irradiated at room temperature with 50 MeV I ions ( $S_e \sim 12 \text{ keV/nm}$ ).<sup>192</sup> Later studies demonstrated more enhanced athermal recovery in 6H-SiC and 3C-SiC over a range of pre-damaged

states under SHI irradiation ( $S_e \sim 33 \text{ keV/nm}$ ).<sup>58,59,193</sup> Since then, high electronic energy loss by ions in SiC has been shown to result in substantial recovery of pre-existing defects and structural disorder over a range of temperatures and at  $S_e$  values as low as  $1.4 \text{ keV/nm}$ .<sup>23,27,28,30</sup> This unequivocally competitive effect (ionization-induced recovery process) in SiC is illustrated in Fig. 14. Combining experimental and computational approaches, researchers have demonstrated that electronic energy loss by energetic ions in SiC results in athermal recovery of pre-existing defects and dynamic annealing of defect production along the ion trajectory. The highly localized inelastic thermal spike effectively induces recovery of many pre-existing defects in SiC over a broad range of energies.<sup>27,28,45,48,58,59,190,191</sup> Research has shown that ions can induce self-healing of pre-existing defects in 4H-SiC at very low values of electronic energy deposition, with a projected threshold of  $1.4 \text{ keV/nm}$ ,<sup>27,28</sup> as illustrated in Fig. 15. More recent results suggest that in-cascade dynamic annealing has an even lower threshold in  $S_e$  of  $1.0 \text{ keV/nm}$ .<sup>48</sup> These results explain the dynamic annealing previously observed in SiC irradiated with ions from  $0.8 \text{ MeV Ne}$  to  $1.5 \text{ MeV Xe}$ .<sup>45,191</sup> Similar ionization-induced recovery of pre-existing defects in Si single crystals at 300 K has been reported following irradiation with  $10 \text{ MeV Co}$  ions ( $S_e = 4.0 \text{ keV/nm}$ ) at fluences of up to  $1 \text{ ion/nm}^2$ ,<sup>194</sup> however, a threshold in electronic energy loss for this process in Si has not yet been determined.

Simultaneous dual-beam irradiation of 6H-SiC with low-energy  $900 \text{ keV I}$  ions and high-energy  $36 \text{ MeV W}$  ions results in the suppression of damage accumulation due to the high electronic energy loss ( $\sim 10 \text{ keV/nm}$ ) of the W ions.<sup>46</sup> Although the studies were carried out under simultaneous dual-beam irradiation of the same area, it is unlikely that ions from both beams will impact the same sample area within a few nanometers in a ps time frame.<sup>28</sup> Thus, energy dissipation from the low-energy and high-energy ions is not spatially or temporally correlated; i.e., the probability is very low that energy dissipation

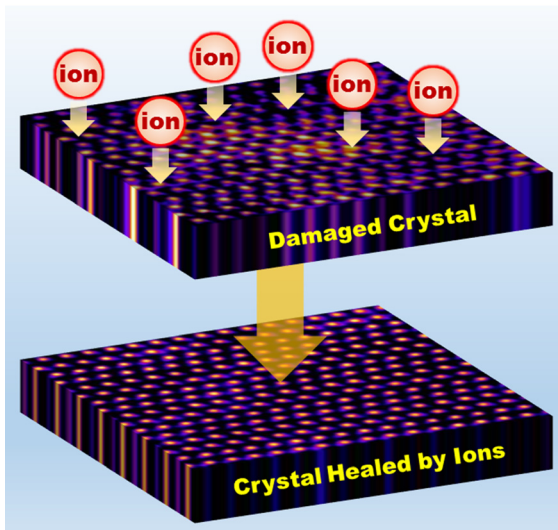


**FIG. 14.** Projected electron microscopy images showing that bombarding pre-damaged SiC (smeared spots in the top slab) with high-energy ions can heal the pre-existing defects (ordered bright spots in the bottom slab) rather than create more. This process of restoring structural order via an inelastic thermal spike is athermal annealing.

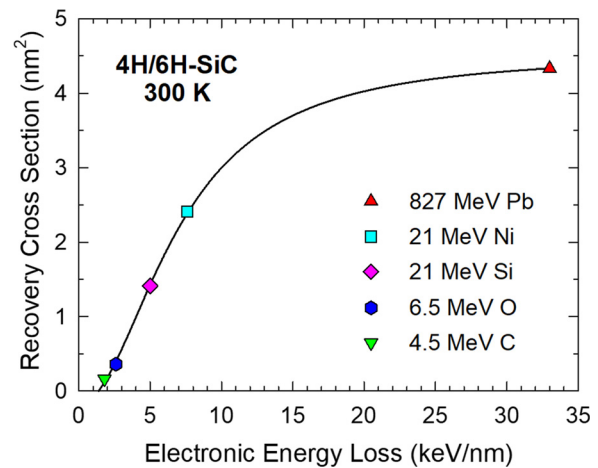


**FIG. 15.** Recovery cross sections in 4H-SiC (C, O, Si, and Ni ions) and 6H-SiC (Pb ions) as a function of electronic energy loss. Reproduced with permission from Zhang et al., *Curr. Opin. Solid State Mater. Sci.* **21**, 285 (2017). Copyright 2017 Elsevier.

from a low-energy ion will interact with energy dissipation from a high-energy ion in the same sample volume at the same time (within a ps). Similar dual-beam irradiations of Si single crystals at 300 K using  $900 \text{ keV I}$  ions, high-velocity  $27 \text{ MeV Fe}$  ions ( $dE/dx_{ele} \sim 5.5 \text{ keV/nm}$ ), and  $36 \text{ MeV W}$  ions ( $dE/dx_{ele} \sim 6.5 \text{ keV/nm}$ ) have been reported,<sup>31</sup> and the results demonstrate efficient ionization-induced annealing in Si.

More recent studies have revealed that in-cascade ionization is even more effective in suppressing the accumulation of irradiation damage in SiC because of the spatial and temporal overlap of electronic energy and ballistic damage energy deposition. The results indicate a significant dependence of irradiation damage accumulation on the ratio of total ionization energy to ballistic damage energy deposition for a range of ions (e.g., the ratio between the ionization energies and the damage energy discussed in Sec. II C). More specifically, in SiC irradiated with  $1.5 \text{ MeV Si}$  ions,<sup>28,48</sup> the inverse dose for amorphization is linearly dependent on the ratio of ionization energy to damage energy, as shown in Fig. 16, which suggests that a unique dose for amorphization of SiC is predicted for a given ion irradiation condition. Furthermore, by linear extrapolation to sufficiently high values of the ratio of ionization to damage energy deposition ( $>200$  for Si ions in SiC), the results suggest that the dose for amorphization should go to infinity and full amorphization may not be achievable. The study of in-cascade ionization effects in SiC irradiated with  $1.5 \text{ MeV Si}$  has also revealed that the threshold for in-cascade ionization-induced annealing is an electronic energy loss of  $\sim 1.0 \text{ keV/nm}$ ,<sup>48</sup> which is slightly less than that described above ( $1.4 \text{ keV/nm}$ ) for highly ionizing ions in a separate effects study.<sup>27,28</sup> In other words, these results have demonstrated that energy greater than  $1.4$  or  $1.0 \text{ keV/nm}$  transferred to electrons causes inelastic thermal spikes sufficient to activate athermal recovery of pre-existing defects<sup>27</sup> or enhance in-cascade recovery and suppress damage production in SiC.<sup>28,48</sup>

The coupling between electronic and nuclear energy dissipation along the ion trajectory has been investigated in single-crystal 4H-SiC and 6H-SiC irradiated with  $21 \text{ MeV Si}$ ,  $21 \text{ MeV Ni}$ , and  $25 \text{ MeV Au}$  ions at 300 K and characterized using RBS in channeling geometry

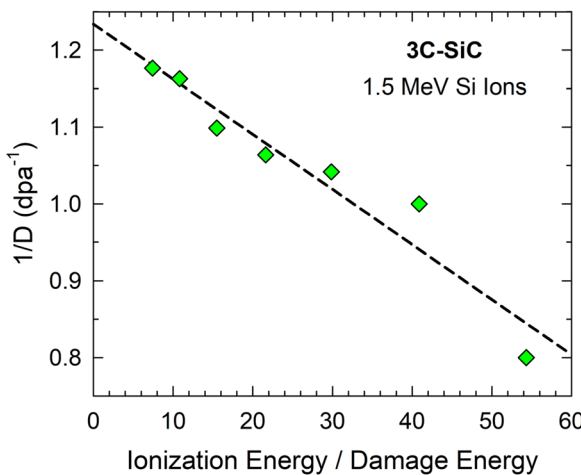


**FIG. 16.** Inverse amorphization dose ( $1/D$ ) as a function of the ratio of ionization energy to damage energy deposition. Reproduced with permission from Zhang *et al.*, *Curr. Opin. Solid State Mater. Sci.* **21**, 285 (2017). Copyright 2017 Elsevier.

(RBS/C). As shown in Fig. 17(a), damage from ballistic disordering processes under 21 MeV Si ion irradiation ( $S_e \sim 5$  keV/nm and  $S_e/S_n \sim 625$  at the surface) is fully suppressed to depths exceeding 1000 nm, and damage is fully suppressed to a depth of about 710 nm under 21 MeV Ni ion irradiation ( $S_e \sim 8.1$  keV/nm and  $S_e/S_n \sim 110$  at the surface). Under 25 MeV Au ion irradiation ( $S_e \sim 6.4$  keV/nm and  $S_e/S_n \sim 7.0$  at the surface), some suppression of ballistic damage processes may be occurring but is not clearly evident [Fig. 17(a)]. Based on the results, a dynamic threshold in electronic energy loss,  $S_{e,\text{th}}$ , for Ni ions is estimated to be 7.12 keV/nm in SiC, above which the electronic energy dissipation fully suppresses damage production due to nuclear energy loss along the incident ion trajectories. More recent results demonstrate that  $S_{e,\text{th}}$  for damage suppression increases sublinearly with incident ion atomic number ( $Z$ ) from C to Ni ions, as shown in Fig. 17(b).<sup>195</sup> Above  $S_{e,\text{th}}$  damage production is suppression by electronic energy loss; below  $S_{e,\text{th}}$  and above the threshold (1 keV/nm) for dynamic annealing, simultaneous damage recovery due to  $S_e$  competes with damage production processes. The competition between ionization-induced damage recovery and ballistic damage production can lead to damage saturation states that are dependent on the ratio  $S_e/S_n$ .<sup>48,195</sup> These results further suggest that the amount of damage suppression does not only depend on the magnitude of  $S_e$ , but also depends on the ratio  $S_e/S_n$ .<sup>48,195</sup> Since a significant fraction of the nuclear energy loss,  $S_n$ , is transferred to electrons by primary and secondary recoils (see the curves of ionization<sub>Recoils</sub> in Figs. 9 and 10), a more appropriate comparison would be the ratio of ionization energy to damage energy, as discussed in Sec. II C. Another important criterion is the correlation between the radial distribution of the electronic and damage energy dissipation along the ion trajectory, as illustrated in Fig. 18, where electronic energy dissipation is calculated based on the two-temperature model and the damage energy dissipation is derived from full-cascade SRIM simulations, as described previously.<sup>28,195</sup> Significant spatial overlapping of the two energy dissipation processes for a single ion leads to decreased defect survival and even suppression of defect production.

In summary, the integration of experiments and simulations in SiC has revealed that (1) increasing  $S_e/S_n$  decreases the rate of damage

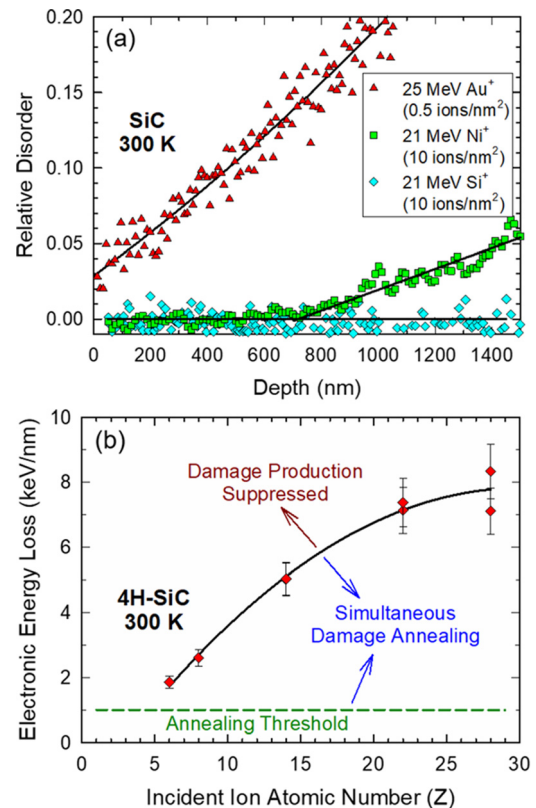


**FIG. 17.** (a) Depth dependence of relative disorder in 4H-SiC after 21 MeV Si and 21 MeV Ni ion irradiation to a fluence of 10 ions/nm<sup>2</sup> and in 6H-SiC after 25 MeV Au ion irradiation to a fluence of 0.5 ions/nm<sup>2</sup>. (b) Dependence of  $S_{e,\text{th}}$  for suppression of damage production on the atomic number ( $Z$ ) of the incident ion; also shown is the threshold in electronic energy loss for dynamic annealing. Reproduced with permission from Zhang *et al.*, *Curr. Opin. Solid State Mater. Sci.* **21**, 285 (2017). Copyright 2017 Elsevier. Reproduced with permission from Nuckols *et al.*, *Acta Mater.* **199**, 96–106 (2020). Copyright 2020 Elsevier.

accumulation; (2) the transient temperatures during the inelastic thermal spike increase with  $S_e$ , resulting in annealing of pre-existing damage along the ion trajectory, regardless of the value of  $S_n$ ; and (3) strong spatial coupling of the thermal spike with ballistic damage processes significantly decreases primary damage production, while higher-energy recoils along the ion trajectory produced by heavy ions (Au) lead to decreased spatial coupling and less reduction in primary damage production, as illustrated in Fig. 18. Research in this area has identified a significant mechanism for self-healing of irradiation damage in SiC for nuclear and space applications. It also has demonstrated the important effects of energy transfer to electrons in repairing ion implantation damage in advanced electronics and for predicting material performance in extreme radiation environments where ionization and defect production occur simultaneously.

Self-healing effects are not limited to SiC. Ulmer and Motta<sup>196</sup> have recently recognized the importance of electronic energy loss as an “instantaneous line-source of heat” that diffuses radially outward along the ion path. They have included athermal reaction rates to account for this thermal spike in a rate theory model to explain microstructural evolution observed in ZrC at cryogenic temperatures.

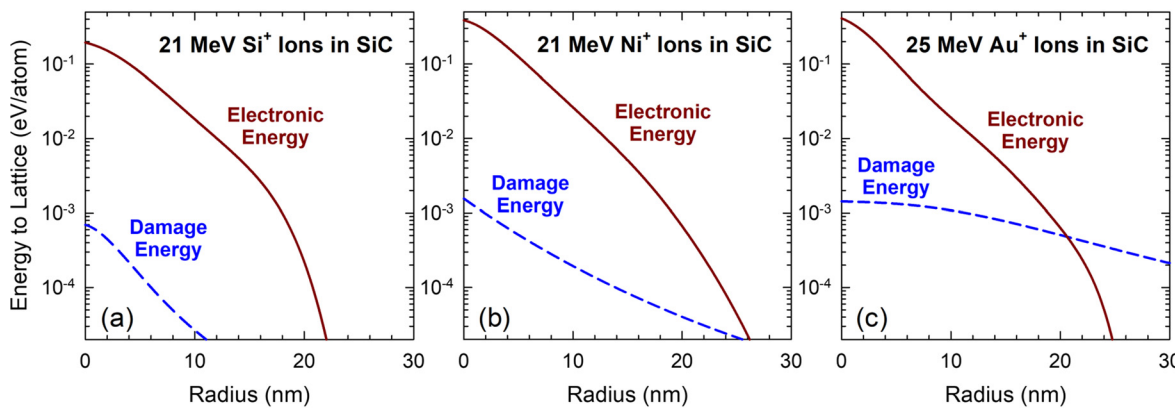


**FIG. 18.** The radial dependence of electronic energy dissipated to the atomic lattice via  $e\text{-}ph$  coupling and the damage energy dissipated to the atomic lattice, calculated over a depth range of 700–800 nm for (a) 21 MeV Si ions, (b) 21 MeV Ni ions, and (c) 25 MeV Au ions.

The competitive effect between nuclear collisions and inelastic ionization processes has also been reported in silicate apatite structures,<sup>197</sup> in which the electronic energy loss from intermediate-energy ions promotes in-cascade recovery. As illustrated in Fig. 19(a), the

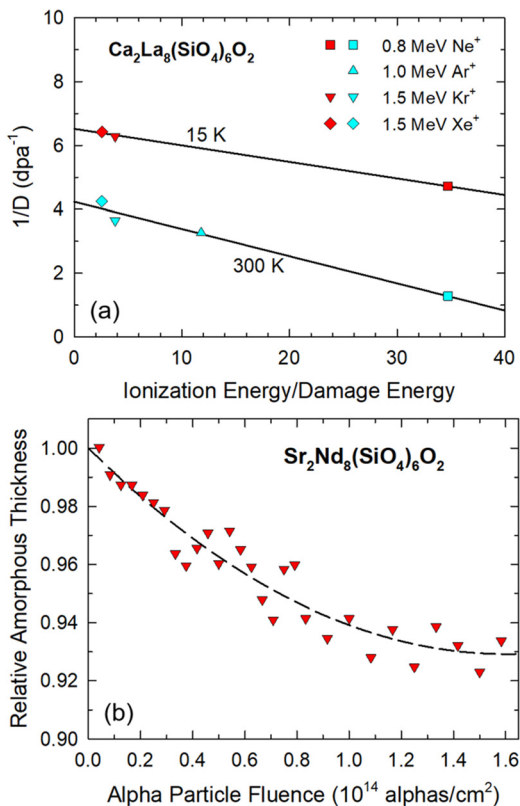


**FIG. 19.** (a) Inverse amorphization dose at 15 and 300 K as a function of the local ratio of ionization energy to damage energy and (b) relative recovery of a buried amorphous layer in  $\text{Sr}_2\text{Nd}_8(\text{SiO}_4)_6\text{O}_2$  under 2.0 MeV alpha particle irradiation at 300 K. Reproduced with permission from Weber *et al.*, RSC Adv. **2**, 595 (2012). Copyright 2012 The Royal Society of Chemistry.

inverse amorphization dose in  $\text{Ca}_2\text{La}_8(\text{SiO}_4)_6\text{O}_2$  for irradiations at 15 and 300 K exhibits a linear dependence on the SRIM-calculated ratio of ionization energy to damage energy, demonstrating a systematic increase in the amorphization dose with an increase in the local ratio of energy dissipation to electronic and displacement processes. Similar recrystallization due to 2 MeV He ions is reported for  $\text{Sr}_2\text{Nd}_8(\text{SiO}_4)_6\text{O}_2$ , in which ionization-induced epitaxial recrystallization of a buried amorphous layer is observed at 300 K [Fig. 19(b)], significantly below the temperature for thermal recrystallization ( $>1000$  K).<sup>197</sup> The result is consistent with the observed sensitivity of silicate apatite compositions to e-beam-induced ionization-induced annealing (Fig. 4).<sup>101</sup> Similar ionization-induced recovery and recrystallization under alpha particle irradiation have been observed in fluorapatite<sup>198</sup> and monazite.<sup>199</sup> Thus, ionization-induced annealing from alpha particles must be considered in predicting the evolution of radiation damage in nuclear waste forms.

This competitive recovery process has also been observed in  $\text{SrTiO}_3$ .<sup>53,55,56</sup> While high-energy ions contribute to damage production in  $\text{SrTiO}_3$  above a threshold electronic energy loss of  $\sim 6.5$  keV/nm (see synergistic effect discussion in Sec. IV C), defect recovery is induced by electronic energy loss below this threshold. Pre-damaged surface layers of  $\text{SrTiO}_3$  have been irradiated with 2 MeV He, 1.2 MeV C, 5 MeV C, and 12 MeV O ions and the results compared with those for irradiation with 200 keV electrons.<sup>53,55</sup> While ionization-induced amorphization does not occur for these ions, the inelastic thermal spike causes enough local heating to induce defect recovery that has been confirmed by MD simulations, as shown in Fig. 20(a). The results indicate two distinct regimes of ionization-induced recovery, as shown in Fig. 20(b). From  $\sim 1.1$  to  $4$  keV/nm, the dominant process for ionization-induced recovery of structural disorder is the transient inelastic thermal spike. Below  $\sim 1.1$  keV/nm, electronic excitations that enhance defect mobility are the dominant process for recovery and recrystallization. While thermal spikes dominate the observed recovery processes above  $\sim 1.1$  keV/nm, surviving electronic excitations may play a role on longer time scales.

The results discussed here show that energetic charged particles do not always damage the material; instead, they can repair pre-existing defects in the atomic structure or suppress defect production and damage evolution. The exposure of a defected material to

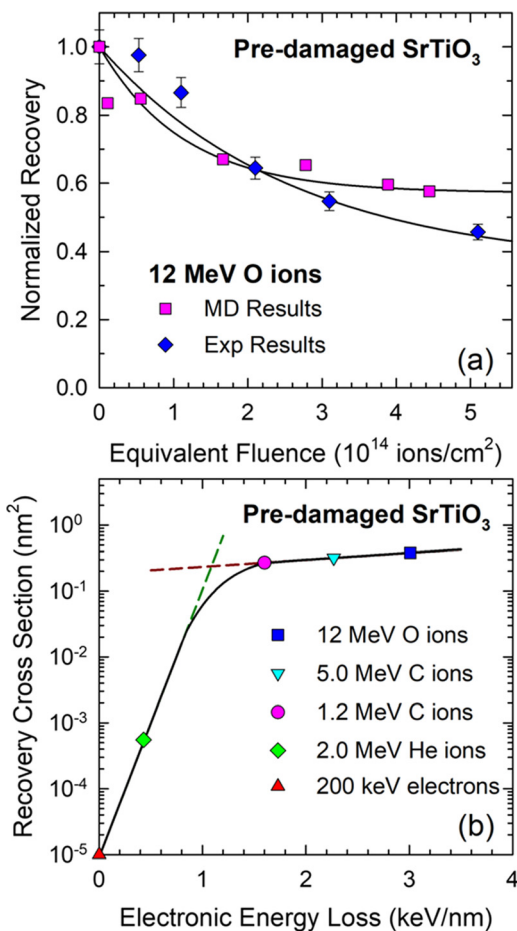


**FIG. 20.** Ionization-induced recovery in pre-damaged  $\text{SrTiO}_3$ : (a) experimental and molecular dynamics as a function of equivalent fluence and (b) recovery cross sections as a function of electronic energy loss. Reproduced with permission from Weber *et al.*, *Scr. Mater.* **173**, 154–157 (2019). Copyright 2019 Elsevier.

high-energy ions can cause local heating along the ion path that results in a significant reduction in the structural disorder at the atomic and microscopic scales. The nonintuitive athermal healing process could lead to in-operando repair of irradiation damage in some carbides and oxides in nuclear and space applications. A fundamental understanding of these energy dissipation processes could allow for better prediction of materials performance after exposure to high-energy ions.

### B. Additive effects on microstructure modification

In contrast to the competitive recovery effects from electronic energy loss, additive effects may occur in some materials in which both electronic and ballistic energy dissipation processes from a single ion lead to more damage production (e.g., amorphization)<sup>23,47,60,138</sup> or microstructural changes (grain growth)<sup>47,98</sup> than occurs from ballistic collisional processes alone.

Nanocrystalline materials are inherently prone to grain growth that is generally activated thermally but can also be driven by irradiation at much lower temperatures. The responses of nanocrystalline

$\text{CeO}_2$  and  $\text{ZrO}_2$  films to ion irradiation have been studied under different nuclear and electronic stopping powers. Specifically, irradiations of nanocrystalline  $\text{CeO}_2$  and  $\text{ZrO}_2$  films<sup>96–98</sup> were carried out at room temperature using 1 MeV Si, 3 MeV Au, and 12 MeV Au ions to different fluences. Grain growth, based on the average size with increasing ion fluence and average dose, was determined from glancing-incident angle x-ray diffraction (GIXRD). As shown in Fig. 21 for nanocrystalline  $\text{CeO}_2$ ,<sup>98</sup> a hyperbolic increase in the crystallite size is observed under both 1 MeV Si and 3 MeV Au ion irradiation. For the same ion fluence, faster grain growth is observed under the 3 MeV Au ion irradiation [Fig. 21(a)], suggesting that the amount of grain growth per incident ion is more effective for 3 MeV Au ions. On the other hand, a faster rate of grain growth under 1 MeV Si irradiation is shown in Fig. 21(b) as a function of the ballistic damage dose (dpa), suggesting more effective growth in crystallite size under 1 MeV Si irradiation, which is contradictory to the result in Fig. 21(a). By varying the amount of energy deposition into the electronic and atomic structures, as described in Sec. II C, an additive effect on grain growth is revealed that is well described as a function of total energy deposition in both nanocrystalline  $\text{CeO}_2$  and  $\text{ZrO}_2$ , as shown in Fig. 22. The seemingly conflicting dependence of grain growth rate on fluence and dose dependence under Si and Au irradiations in Fig. 21 clearly reveals that,

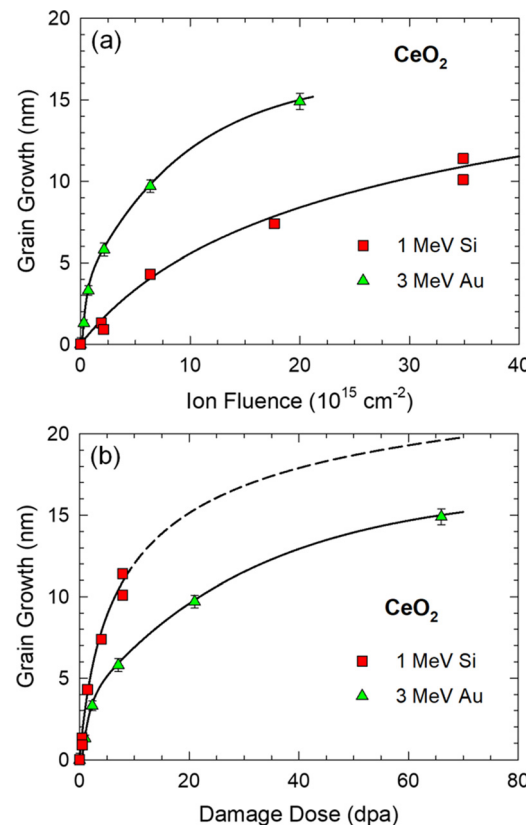


**FIG. 21.** Radiation-induced grain growth in nanocrystalline  $\text{CeO}_2$  films at 300 K under Si and Au irradiations as a function of (a) fluence and (b) average damage dose. Reproduced with permission from Zhang *et al.*, *Phys. Chem. Chem. Phys.* **16**, 8051–8059 (2014). Copyright 2014 The Royal Society of Chemistry.

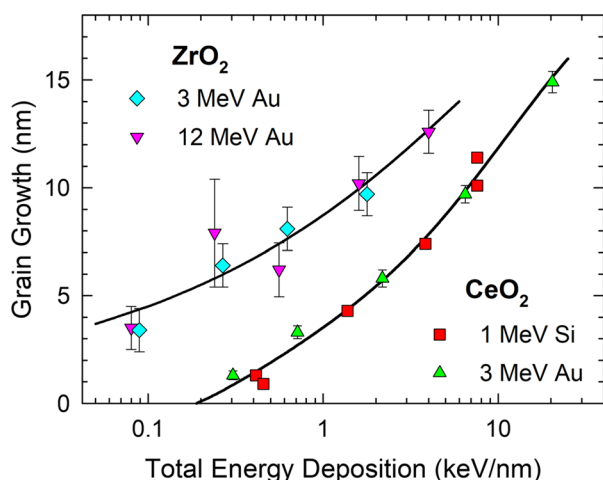


**FIG. 22.** Ion irradiation-induced increase in crystallite size in nanocrystalline CeO<sub>2</sub> and ZrO<sub>2</sub> as a function of total energy deposition in logarithmic scales. Reproduced with permission from Zhang *et al.*, Phys. Chem. Chem. Phys. 16, 8051–8059 (2014). Copyright 2014 The Royal Society of Chemistry.

in nanocrystalline ceria<sup>97</sup> and zirconia,<sup>96,98</sup> both the displacement energy and the electronic energy deposition contribute to the overall grain growth (Fig. 22) and that neither  $dE/dx_{\text{nucl}}$  nor  $dE/dx_{\text{ele}}$  is negligible.

MD simulations combining the two-temperature thermal spike model with elastic atomic collision processes along an ion trajectory have resolved a long-standing anomaly in ZrSiO<sub>4</sub> regarding a higher damage production efficiency for light ions (Kr and Xe) than for heavy ions (Pb and Bi). These simulations have revealed the critical contribution of ionization to damage production in ZrSiO<sub>4</sub> when the electronic energy loss is transferred to the atomic substructure via *e-ph* coupling. The energy transfer results in an additive increase in damage production when the thermal spike from electronic energy loss is included in MD simulations of single-ion events for 0.8 MeV Kr and Xe ions<sup>138</sup> (Fig. 23). The modeling work has shown that the increased spatial and temporal overlap of electronic and ballistic energy dissipation for 0.8 MeV Kr ions produces more damage per ion than the overlap for 0.8 MeV Xe ions with a higher nuclear energy loss, which is consistent with experimental observations and resolves the anomaly.

### C. Synergistic effects causing increased damage production

Researchers have also discovered that synergistic interactions (greater than the sum of separate electronic and nuclear energy dissipation processes) can occur because of the presence of pre-existing collisional defects that can sensitize a material to electronic energy loss effects and result in substantially more damage production (e.g., amorphous tracks) than would occur from the sum of electronic and ballistic damage production processes.

A colossal synergistic effect, orders of magnitude larger than anything previously reported, has been discovered to occur between inelastic energy loss to electrons by energetic ions (e.g., 21 MeV Ni) and pre-existing atomic defects created by elastic energy loss of 900 keV Au ions in single-crystal SrTiO<sub>3</sub>.<sup>142</sup> This synergy between

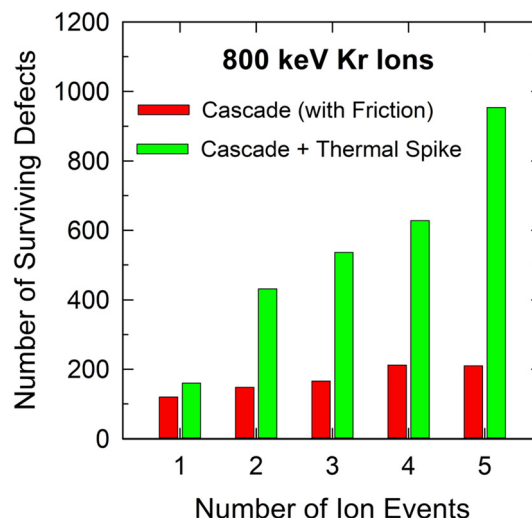


**FIG. 23.** MD simulations of defect production from 800 keV Kr ions in ZrSiO<sub>4</sub> due to collision cascades, either with electronic energy loss removed as a friction term or with electronic energy loss removed and coming back into the simulation cell as a thermal spike. Reproduced with the permission Zarkadoula *et al.*, from Appl. Phys. Lett. 107, 261902 (2015). Copyright 2015 AIP Publishing.

electronic energy loss by ions and pre-existing atomic defects has been investigated in SrTiO<sub>3</sub> over a wide range of electronic energy loss and pre-existing damage levels.<sup>50,55,200</sup> The effect results in the formation of nanometer-sized amorphous tracks that increase in diameter with increasing pre-existing defect density, but only in the narrow region where pre-existing defects exist. This is illustrated in Fig. 24(a), where a low level of pre-existing disorder sensitizes SrTiO<sub>3</sub> to the formation of amorphous tracks by 21 MeV Ni ions, as evidenced by the rapid increase in the RBS/C yield over the channel numbers corresponding to the pre-damaged layer; no increase in disorder over the pristine level is observed in an undamaged sample over the same range of fluences.<sup>142</sup> The synergistic formation of amorphous tracks occurs only over the depth region of the pre-damaged state, as shown in Fig. 24(b) for 21 MeV Ni ions.

Electron microscopy<sup>55,142,200</sup> and MD simulations,<sup>50,55,142</sup> based on a TTM, have confirmed that pre-existing defects sensitize SrTiO<sub>3</sub> to amorphous track formation, as shown in Fig. 25 for 21 MeV Ni ions. The pre-existing defects decrease the electronic and atomic thermal conductivities and increase *e-ph* coupling, which results in a significant increase in the local intensity of the thermal spike along the path of each ion, as shown in Fig. 11. The highly localized thermal spike creates a nanoscale cylindrical amorphous track, but only in the region with pre-existing defects (Fig. 24, increase in the backscattering yield and the relative disorder). Moreover, the inelastic thermal spike model predicts that the diameters of amorphous tracks should increase with defect density and with increasing electronic energy loss of the ions. This prediction has been confirmed by experimental observation, as shown in Fig. 26. The electronic stopping power threshold for ion track formation is found to be about 5.9 keV/nm for a pre-existing disorder level of 30% (Fig. 26). It has been recently reported that this threshold is about 6.2 keV/nm for a pre-existing disorder level of 15.5% (Ref. 200) and on the order of 6.7–7.0 for disorder levels of

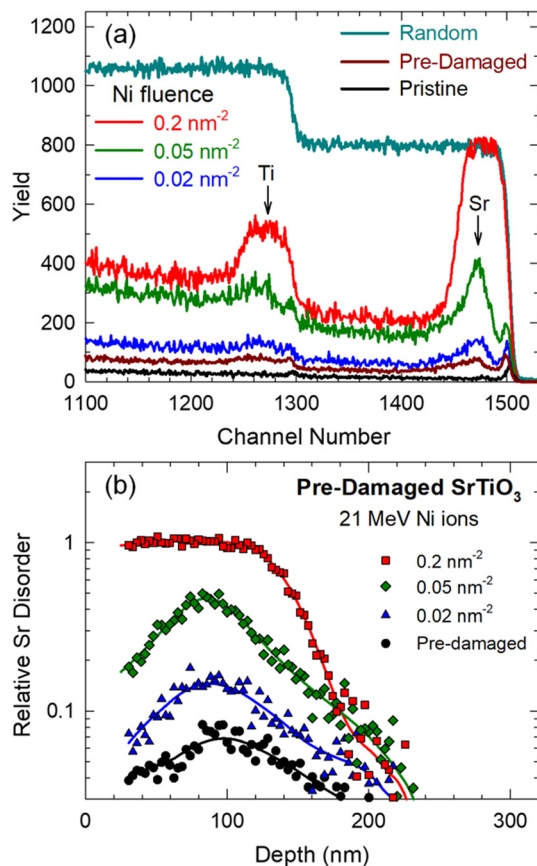


**FIG. 24.** (a) RBS/C spectra along the [100] direction in SrTiO<sub>3</sub> for pristine (undamaged), pre-damaged, and pre-damaged after irradiation at 300 K with 21 MeV Ni ions to different ion fluences. (b) Depth profiles of disorder on the Sr sublattice for the RBS/C spectra in (a). Reproduced with permission from Weber *et al.*, Sci. Rep. 5, 7726 (2015). Copyright 2015, Authors licensed under a Creative Commons Attribution-NonCommercial-ShareAlike 4.0 International License.

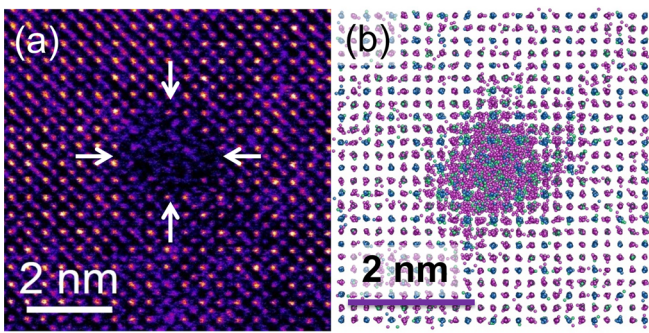


**FIG. 25.** A HAADF image (a) of an amorphous track produced by a 21 MeV Ni ion in pre-damaged ( $f_o = 0.07$ ) SrTiO<sub>3</sub>. MD simulation (b) depicts the amorphous track formed by a 21 MeV Ni ion in defective SrTiO<sub>3</sub>. Reproduced with permission Weber *et al.*, Sci. Rep. 5, 7726 (2015). Copyright 2015, Authors licensed under a Creative Commons Attribution-NonCommercial-ShareAlike 4.0 International License.

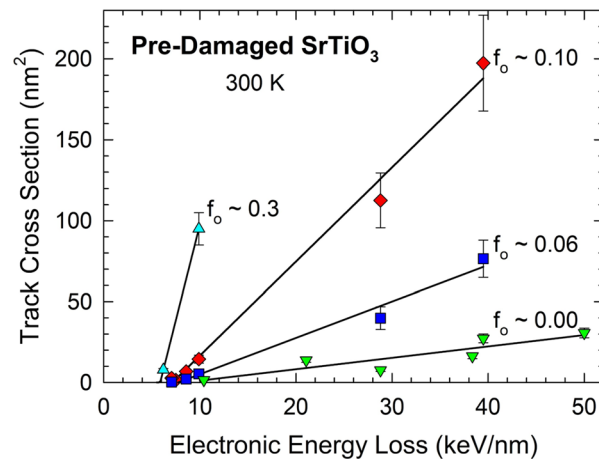


**FIG. 26.** Amorphous track cross sections in pre-damaged SrTiO<sub>3</sub> as functions of pre-existing disorder,  $f_o$ , and electronic energy loss for a range of ions from 18 MeV Si ions (6.2 keV/nm) to 946 MeV Au ions (39.5 keV/nm). Also included are average cross sections for tracks in pristine ( $f_o = 0.00$ ) SrTiO<sub>3</sub>.

6%–10%.<sup>55</sup> These thresholds in electronic stopping power are significantly below the threshold of 10 keV/nm determined for discontinuous track formation in pristine SrTiO<sub>3</sub>,<sup>201</sup> as indicated by the data for pristine SrTiO<sub>3</sub> ( $f_o \sim 0.00$ ) in Fig. 26. Below these thresholds, ionization-induced annealing of the pre-damage SrTiO<sub>3</sub> is observed,<sup>53</sup> as discussed in Sec. IV A and shown in Fig. 20. The dependence of ion track diameter on the initial pre-damaged disorder level is shown in Fig. 27 for 21 MeV Ni ions<sup>204</sup> and 629 MeV Xe ions. This collection of work on SrTiO<sub>3</sub> identifies a major gap in understanding the role of defects in electronic energy dissipation and *e-ph* coupling. Since SrTiO<sub>3</sub> is a foundational material in functional microelectronics, the work provides new insights for creating novel interfaces and nanostructures to functionalize thin-film structures, including tunable

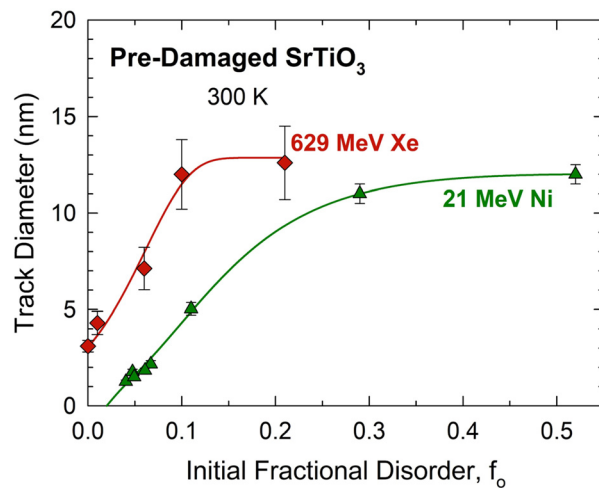


**FIG. 27.** Amorphous track diameter in pre-damaged SrTiO<sub>3</sub> as a function of initial pre-damaged disorder level for 21 MeV Ni ions and 629 MeV Xe ions.

electronic, magnetic, and optical properties in thin films of epitaxial  $\text{SrTiO}_3$ .

Ion irradiation of potassium tantalate ( $\text{KTaO}_3$ ) has also been performed to investigate the evolution of irradiation damage with and without significant electronic energy deposition.<sup>202–204</sup> Damage accumulation under irradiation with 2 MeV Au ions follows a direct-impact/defect-stimulated model and occurs more rapidly than in  $\text{SrTiO}_3$  under similar conditions. Electronic energy deposition from 21 MeV Ni ions creates negligible damage in pristine  $\text{KTaO}_3$  to depths of 1  $\mu\text{m}$ ; however, damage is greatly enhanced in samples containing pre-existing defects, as evidenced by rapid amorphization due to track formation.<sup>205</sup> The cross sections for amorphous tracks show a nearly linear dependence on initial disorder, comparable to that observed in  $\text{SrTiO}_3$  (Fig. 26). A threshold for track formation in pre-damaged  $\text{KTaO}_3$  has not yet been determined but is the subject of an ongoing investigation. For pristine  $\text{KTaO}_3$ , a threshold electronic energy loss of 13.8 keV/nm has been recently indicated for the low-velocity regime.<sup>205</sup>

Lithium tantalate ( $\text{LiTaO}_3$ ) has outstanding electro-optical properties that can be tailored by ion beams for optical devices.<sup>206,207</sup> The coupled effects of electronic and nuclear energy deposition in  $\text{LiTaO}_3$  have also been investigated.<sup>57,208</sup> Irradiation of pristine  $\text{LiTaO}_3$  samples with 2 MeV Ta ions or 1 MeV Au ions leads to amorphization due to atomic displacement damage that is described by a disorder accumulation model, whereas irradiation of pristine  $\text{LiTaO}_3$  with 20 or 21 MeV Si ions did not produce significant damage at similar ion fluences. Similar to the studies on  $\text{SrTiO}_3$  and  $\text{KTaO}_3$ , 2 MeV Ta ions are used to introduce pre-damage in  $\text{LiTaO}_3$ ; subsequent irradiation of the pre-damaged  $\text{LiTaO}_3$  with 21 MeV Si ions at room temperature leads to amorphous track formation via a synergistic two-stage phase transition process, as illustrated in Fig. 28. During the first stage, a possible ferroelectric phase transformation occurs that is complete at

relatively low doses, as evidenced by the saturation at different depths. This rapid ionization-induced transformation has a relatively large cross section of about 240 nm<sup>2</sup>. The step-like increase in disorder with depth suggests that the structure has changed, but the pre-existing defect distribution is relatively unchanged. This ionization-induced transformation appears to have sufficiently changed electronic and lattice thermal conductivities and the  $e\text{-}ph$  coupling to sensitize  $\text{LiTaO}_3$  to the formation of amorphous tracks by 21 MeV Si ions during the second stage, with an order of magnitude lower track cross section. While a threshold for these pre-existing defect-stimulated processes in  $\text{LiTaO}_3$  has not yet been identified, the threshold for amorphous track formation in pristine  $\text{LiTaO}_3$  is estimated to be less than 12 keV/nm.<sup>205</sup> This discovery could lead to the design and control of nano-scale ferroelectric phases in thin film structures and tailoring of the optical properties and functionality of novel devices.

While similar behavior has also been observed in  $\text{LiNbO}_3$ ,<sup>49</sup> this increased sensitivity to pre-damaged states is not limited to perovskites. Simultaneous dual-beam irradiations of MgO have revealed a synergy between defects produced by 900 keV I ions and the high electronic energy loss of 36 MeV W ions with regard to overall damage accumulation, which is much higher than a simple sum of the damage accumulation from separate irradiations with each ion.<sup>46</sup> Ion tracks can also be formed in the subthreshold electronic energy loss regime in both InP and GaN, if the materials are pre-damaged to produce point defects and clusters that effectively increase the  $e\text{-}ph$  coupling.<sup>172</sup>

In summary, the synergistic effect has significant implications for functionalizing ceramics and modeling damage accumulation processes: the damage production process and rate can change dramatically above a threshold defect concentration.

#### D. Electronic excitations and relaxation

Defect processes and their interactions with local charge can be studied using real-time luminescence probes. Ions carry significant momentum and interact through the Coulomb force between ions and target electrons and nuclei that is much stronger than the interaction of the electrons and nuclei through electromagnetic waves under electron or photon excitation. *In situ*, real-time ionoluminescence (IL) measurements during ion irradiation have provided information on the evolution of emission bands with ion fluence that can be used to establish correlations between point defect kinetics and phase stability. Dynamics of electronic excitation have been shown to govern a rapid increase in emission band intensity at 2.8 eV in  $\text{SrTiO}_3$  irradiated with protons, whereas accumulated irradiation damage accounted for a subsequent intensity decrease in this band. A well-resolved band at 2.0 eV dominated below 170 K,<sup>155,209–211</sup> and its intensity increased with increasing ion fluence at 100 K. This 2.0 eV band has previously been observed only in heavily strained and amorphous  $\text{SrTiO}_3$ ; however, based on *ab initio* theoretical calculations, it is attributed to  $d\text{-}d$  transitions from electrons that are self-trapped as relaxed  $\text{Ti}^{3+}$  centers in distorted  $\text{TiO}_6$  octahedra, which are stabilized by a high concentration of irradiation-induced oxygen vacancies. This interpretation has been confirmed in a more recent study using Cr-doped  $\text{SrTiO}_3$ ,<sup>210</sup> in which decay of the  $\text{Cr}^{3+}$  luminescence (due to hole trapping) was correlated with the growth of the 2.0 eV band. This work has demonstrated that defect evolution can be monitored in real time using IL, as illustrated in Fig. 29, and that the 2.0 eV emission band can be used to

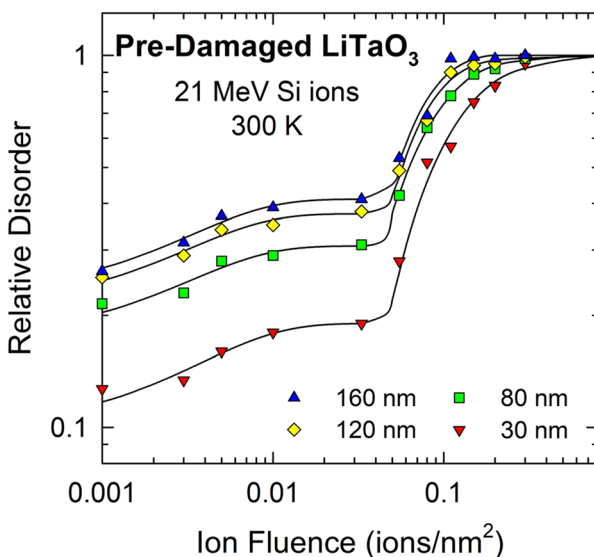


**FIG. 28.** Relative disorder at different depths in pre-damaged  $\text{LiTaO}_3$  as a function of 21 MeV Si ion fluence. Reproduced with permission from Sellami *et al.*, Mater. Res. Lett. **6**, 339–344 (2018). Copyright 2018 Taylor & Francis Group.

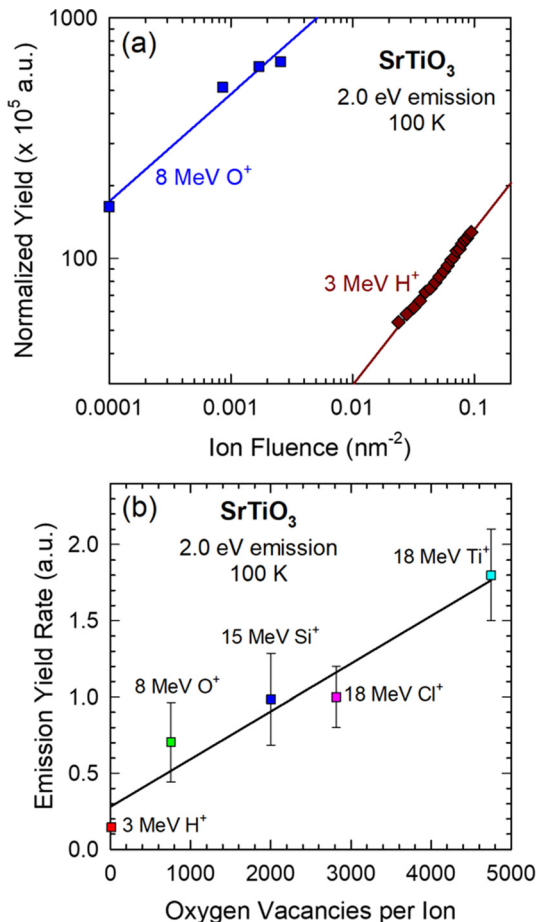


**FIG. 29.** (a) Normalized yield of 2.0 eV emission band (O vacancies) in SrTiO<sub>3</sub> at 100 K as a function of fluence for 8 MeV O ions and 3 MeV H ions. (b) Emission yield of 2.0 eV band as a function of SRIM-predicted oxygen vacancy yield per ion for different ions. Reproduced with permission from Crespillo *et al.*, Appl. Mater. Today 12, 131 (2018). Copyright 2018 Elsevier.

monitor the evolution of oxygen vacancies in SrTiO<sub>3</sub> under irradiation and annealing.

The effects of electronic excitations on SrTiO<sub>3</sub> have been investigated using first principles calculations.<sup>212</sup> The results suggest that electronic excitation induces a metallic transition and charge redistribution in SrTiO<sub>3</sub>. Upon electronic excitation, phonon frequencies in SrTiO<sub>3</sub> become highly localized and a new peak appears in the phonon density of states with negative frequencies, an indication of lattice instability. Furthermore, dynamics simulations have confirmed that SrTiO<sub>3</sub> undergoes a transition to an amorphous structure under strong electronic excitations.<sup>212</sup> The luminescence of SrTiO<sub>3</sub> under electronic excitation is consistent with the evolution of atomic structures, a finding that supports using luminescence to probe structural changes.

Damage production per ion can be characterized using *in situ* RBS/C to determine the relative atomic disorder created per ion, and using *in situ* IL and/or cathodoluminescence (CL) to determine the number of specific defects or relative phase change per ion. The primary damage state (or some subset of defect states) produced from

coupled energy dissipation in complex oxides may be characterized by using *in situ* photoluminescence (PL), CL, or IL to measure the incremental change in an emission band for oxygen vacancies under irradiation, from which the relative number of oxygen vacancies per ion can be determined. Similarly, the optimum conditions for producing divacancies in SiC, a potential qubit, can be determined from the luminescence signature. Another experimental approach is to irradiate samples to low ion fluences (nonoverlapping damage regions) with ions of specific energy to characterize an average primary damage state by *in situ* ion channeling and optical techniques. With PL, CL, and IL information as references for comparison, a fundamental understanding of single ion response can be investigated with a focus on the similarities and differences under photon, electron, and ion excitation.

## V. RADIATION-INDUCED NONEQUILIBRIUM PROCESSES IN CHEMICALLY DISORDERED METALLIC ALLOYS

While a simple macroscopically crystalline structure is retained in complex SP-CSAs, the random site occupancy by multiple metal species creates unique site-to-site atomic displacements from ideal lattice positions and little translational periodicity, leading to extreme intrinsic complexity at the electronic and atomic levels.<sup>24</sup> Chemical complexity in SP-CSAs is achieved by controlling the number, types, and concentrations of the constituent elements. Such unusual chemical disorder, which provides tunability of the electronic band structure<sup>109,213</sup> and local lattice distortion,<sup>214</sup> inevitably creates distinct properties at the level of electrons and atoms that are expected to have noticeable ionization effects and impacts on the coupling of ionization and damage energy dissipation processes induced by energetic particles.

Because of the extreme chemical complexity in CSAs, two aspects of ionization effects have drawn research interest: slow heat dissipation and strong *e-ph* coupling. In this section, we discuss compositional complexity that leads to differences in slow heat conduction that is beneficial to radiation resistance (Sec. V A); *e-ph* coupling that results in more isolated smaller defect clusters (Sec. V B); nonequilibrium damage evolution involving unique defect energetics and mass transport (Sec. V C); and consequent defect dynamics at the early stage of radiation damage and ultimately reducing the number of surviving defects and enhancing radiation tolerance (Sec. V D). We emphasize how elemental alteration (intrinsic chemical disorder, i.e., electronic band structure and local lattice distortion) can affect the coupled electronic and damage energy dissipation and subsequent nonequilibrium processes. We focus on demonstrating unique links among intrinsic material properties, energy dissipation, and enhanced athermal dynamic processes.

### A. Slow heat dissipation delaying damage buildup

Defect formation and evolution under irradiation in metallic alloys have long been inaccurately considered to involve primarily atomic-level dynamics. As a result, electronic energy dissipation has largely been neglected or assumed to be marginally relevant. The connection between electronic energy dissipation mechanisms and atomic damage processes is described by an inelastic thermal spike model. In the model, electrons in the vicinity of an ion track undergo a large degree of excitation and electron-electron scattering and subsequently transfer energy, via *e-ph* coupling, to atoms in the same region,

causing local heating. As discussed in Sec. II A, intense electronic excitation by SHIs leads to either amorphization or pre-existing damage annihilation in some metallic systems.<sup>43,63–67,73,122</sup> At much lower energies ( $\sim 10$  keV), enhanced defect recombination is attributed to electronic energy dissipation.<sup>70,71</sup>

In many irradiation studies, electronic energy dissipation in metallic alloys is shown to exert a strong influence on the rate and type of atomic damage.<sup>123,215–218</sup> Recent studies<sup>24,219</sup> have revealed strong, previously unrecognized changes in the electrical, thermal, and magnetic properties in chemically disordered SP-CSAs, such as reduction in the electrical and thermal conductivities. The reduction is shown to be element-specific and closely related to the electronic band structure.

To demonstrate the effects of chemical complexity with variations in the number of  $3d$  electrons and their effects on electrical, thermal, and magnetic properties, eight model single crystals—extending from elemental Ni to quinary HEAs [Fig. 30(a)]—have been synthesized and investigated by combining experimental and modeling methods. The very low channeling yield of the pristine crystals (<2.5%), as illustrated in Fig. 30(b), reveals the damage-free level compared with the random level, which demonstrates the high quality of

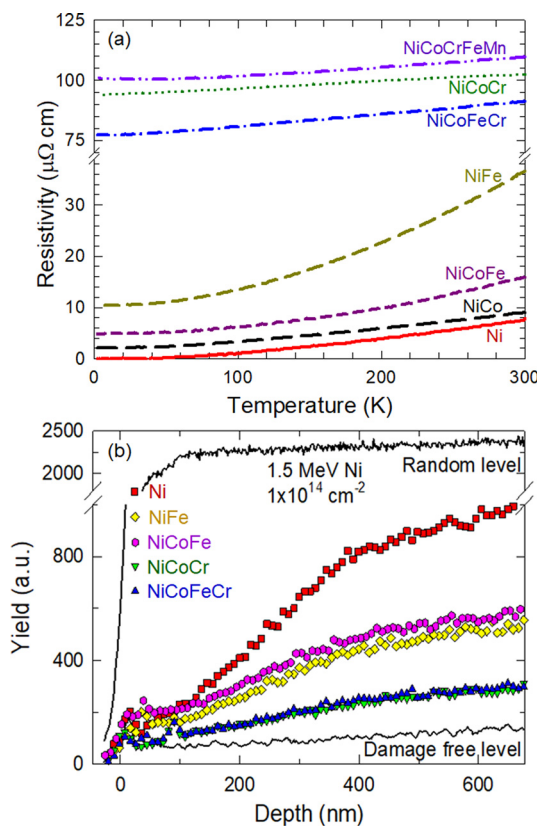


**FIG. 30.** Effects of compositional complexity on (a) electrical resistivity and (b) irradiation resistance. A similar trend between electrical resistivity and irradiation performance indicates a link between slow energy dissipation and modified defect evolution. Reproduced with permission from Zhang *et al.*, *J. Mater. Res.* **31**, 2363 (2016). Copyright 2016 Cambridge University Press.

the crystals. Such crystals make it possible to measure intrinsic properties and study defect production and damage accumulation with increasing chemical complexity. Specific heat capacity, lattice thermal expansion, thermal diffusivity, and conductivity have been studied at temperatures up to 1273 K.<sup>220</sup> These alloys showed similar specific heat values of 0.4–0.5  $\text{J}\cdot\text{g}^{-1}\cdot\text{K}^{-1}$  at room temperature, but their temperature dependence varied greatly because of Curie temperature and other anomalies, possibly related to short-range order.<sup>221,222</sup> Figure 30(a) shows high and low electrical resistivity depending on whether the alloys contain Cr or Mn, respectively. Thermal conductivity (not shown) exhibits a similar differentiation depending on the Cr and Mn content.

On the theoretical side, electronic states can be described using a mean-field single-site approximation, the Coherent Potential Approximation (CPA), in its first-principles Korringa–Kohn–Rostoker (KKR–CPA) formulation.<sup>223,224</sup> Transport coefficients are obtained using the Kubo–Greenwood linear response theory. Mean free paths can differ by up to three orders of magnitude for complex alloys.<sup>213,225</sup> Residual resistivity calculations reveal the high residual resistivity of alloys containing Cr and Mn, as confirmed by the experimental results [Fig. 30(a)].

A recent study<sup>219</sup> highlights that the electronic deformation capability of Cr/Mn/Fe with half-filled electron band structures is higher than that of Ni/Co/Cu. Research<sup>24,109,219</sup> also has shown that alloying elements with increasing differences in the  $3d$  electrons—partially filled and nearly full  $d$  bands—can substantially reduce the ability to dissipate energy that is beneficial to radiation resistance. That finding is supported by the RBS/C results shown in Fig. 30(b), where irradiation-induced damage is clearly visible in terms of increased RBS yield resulting from the formation of defects and dislocation loops. The slower damage accumulation in more chemically disordered alloys (e.g., NiCoFeCr and NiCoCr), than in less chemically disordered alloys (NiFe and NiCoFe) and limited disordered NiCo and pure Ni, is attributed to lower electronic and atomic thermal conductivities<sup>226–228</sup> and strong  $e\text{-}ph$  coupling.<sup>72,106,107,166</sup> Knowledge of the electronic structure of 3d SP-CSAs and their element-based, temperature-dependent, intrinsic properties has provided critical insights into energy dissipation processes. The critical role played by athermal effects (e.g., energy transfer between electrons and atoms) and the need to accurately describe  $e\text{-}ph$  coupling and energy dissipation to model and predict defect production and resulting structures are discussed below.

## B. Electronic and ionic energy exchange resulting in more isolated smaller defect clusters

Radiation damage mechanisms have been investigated by incorporating the coupled effects of energy carriers into atomistic simulations to better predict the outcome of damage events. Energy transfer between atoms and electrons is closely affected by the strength of the  $e\text{-}ph$  coupling strength, one of the intrinsic properties of a specific alloy. The effects of the electronic excitation on damage production and defect structures have recently been subjected to intense studies.

Two different quantum mechanical approaches, CPA and time-dependent DFT (TD-DFT), have been used to estimate the  $e\text{-}ph$  coupling in SP-CSAs. The CPA description of disorder on the electronic substructure excels in the description of magnetic effects.<sup>146</sup> Both the absolute value and the temperature dependence of the electron lifetimes are determined by considering phonons and magnetic moment

fluctuations. In SP-CSAs, magnetic ordering is accompanied by a decrease in the electronic density of states at the Fermi level, which reduces the  $e\text{-}ph$  coupling. As a result,  $e\text{-}ph$  coupling values for the same alloys are  $\sim 50\%$  smaller in the magnetic state than in a nonmagnetic state. The calculated  $e\text{-}ph$  coupling initially increases with increasing temperature. Above the Curie temperature, the calculated  $e\text{-}ph$  coupling decreases. The rate of decrease is determined by the rate of reduction in the number of available states above the Fermi level, i.e., the shape of the density of states above the Fermi level. The TD-DFT approach<sup>163–165,229</sup> describes the coupling strength in terms of the phonon wave vector, the  $q$ -dependence of phonon lifetimes. In this approach, the  $e\text{-}ph$  interactions are viewed as a stopping power process that allows for an accurate description of the out-of-equilibrium phonon population, similar to the interactions appearing in pump-probe laser heating experiments.<sup>145</sup> Building upon this approach, electron-ion coupling can be modeled at the atomic scale with collective vibrational modes.<sup>77</sup> This theoretical development allows fs interactions of ions and electrons to be described from quantum mechanics. Effects resulting from electronic excitations hence can be incorporated seamlessly in MD models to correctly simulate the aftermath of ionizing radiation events, including electronic energy dissipation, phonon relaxation lifetimes, and temperature equilibration processes.

Nuclear energy loss results in displacement damage and defect cluster formation, while energy transfer to the electrons leads to high electronic temperatures. To understand whether inelastic energy deposited to electrons would affect atomic processes resulting from the simultaneous elastic energy deposition, the energy transfer from a fast-moving ion to several fcc SP-CSAs via nuclear and electronic energy loss has been modeled using the 2T-MD model. The approach was used as an alternative to previous modeling in terms of classical MD with or without electronic stopping as a friction force—in which ionization effects are ignored or electronic energy is simply treated as excess energy that is subtracted from the projectile energy. The strength of the  $e\text{-}ph$  interactions and their temperature dependence<sup>146</sup> are incorporated into damage prediction models using the 2T-MD simulations.<sup>72,106,166</sup> Simulations of 30 keV and 50 keV Ni ion cascades in Ni and some CSAs (Fig. 31) have been performed.<sup>72,106,166</sup> The results of classical MD simulations, where the electronic effects are ignored [Fig. 31(b), left], are compared with simulations in which the electronic stopping is simply removed from the system [Fig. 31(b), middle] or the  $e\text{-}ph$  coupling is incorporated [Fig. 31(b), right]. The energy that returns to the lattice via  $e\text{-}ph$  interactions enhances defect recombination and produces more isolated defects. In other words, if the  $e\text{-}ph$  coupling is ignored, the predicted vacancy cluster size is overestimated. Compared with the results obtained from classical MD simulations in which the electronic effects are ignored, the 2T-MD results show less damage with smaller defect clusters. The 2T-MD simulations<sup>106,166</sup> also demonstrate that the damage morphology depends on electronic properties ( $g$  and  $K_e$ ). The vacancy and interstitial numbers in Fig. 32 illustrate that, in CSAs with stronger  $e\text{-}ph$  coupling (i.e., larger  $g$  values), rapid energy transfer to the lattice during collision cascades leads to enhanced local annealing; therefore, the formation of large defect clusters is suppressed. On the other hand, in relatively simple CSAs with a high  $K_e$ , the electronic subsystem cools down faster as a result of more effective heat dissipation and therefore less energy available to return to the atomic subsystem to anneal defects.

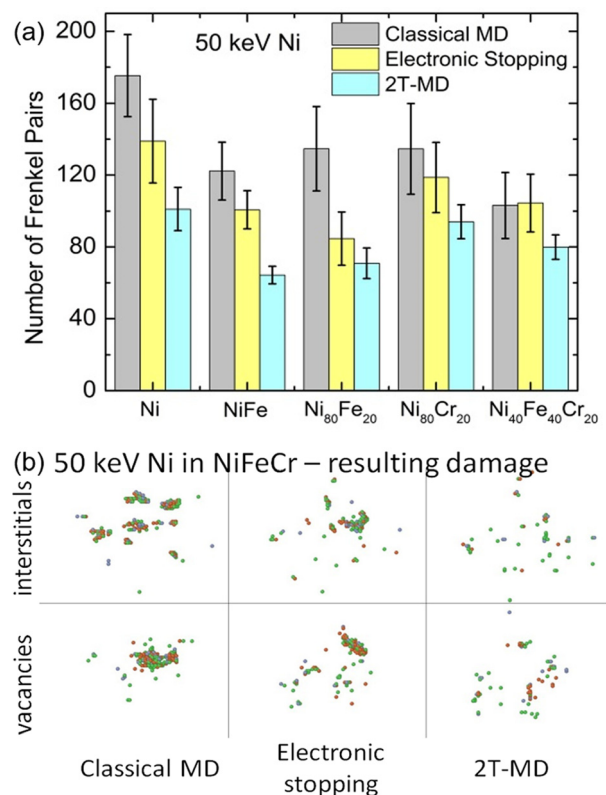


**FIG. 31.** Cascade simulations of 50 keV Ni: classical MD with all energy into atomic displacements, electronic stopping where only nuclear energy loss is considered, and 2T-MD where interactions of nuclear and electronic energy loss result in more isolated smaller defect clusters. Green and pink dots are interstitials and vacancies, respectively. Reproduced with permission from Zarkadoula *et al.*, J. Alloys Compd. 700, 106 (2017). Copyright 2017 Elsevier.

Consequently, larger defect clusters are formed, as shown in Fig. 32, in the case of high electrical thermal conductivity  $2K_e$  and  $5K_e$ .<sup>106</sup> Electronic effects are more pronounced in higher-energy cascades.<sup>106</sup> Recent work on overlapping high-energy irradiation events<sup>166</sup> suggests that excitation-induced local heating of the lattice can anneal both defects created from previous events and concurrent defects due to the ongoing displacement events, suppressing the accumulation of displaced atoms and the formation of large vacancy clusters.

The 2T-MD simulations of the coupling between different dissipation mechanisms suggest that ballistic recoil damage in alloys can be mediated by electronic annealing, just as has been observed in ceramics and semiconductors.<sup>23,27,28,138,204</sup> In harsh radiation environments, the early stages of damage production and cluster formation in complex CSAs closely relate to slow heating dissipation and local defect annealing due to  $e\text{-}ph$  interactions. The 2T-MD model predicts not only less damage in SP-CSAs but also the formation of smaller defect clusters. Dissipation of inelastic energy (deposited to electrons) interacts with elastic energy transfer processes (energy deposited simultaneously to atomic recoils), which influences the shape and size of collision cascade damage. This research highlights the need to include the local energy exchange between atomic and electronic subsystems in MD simulations.

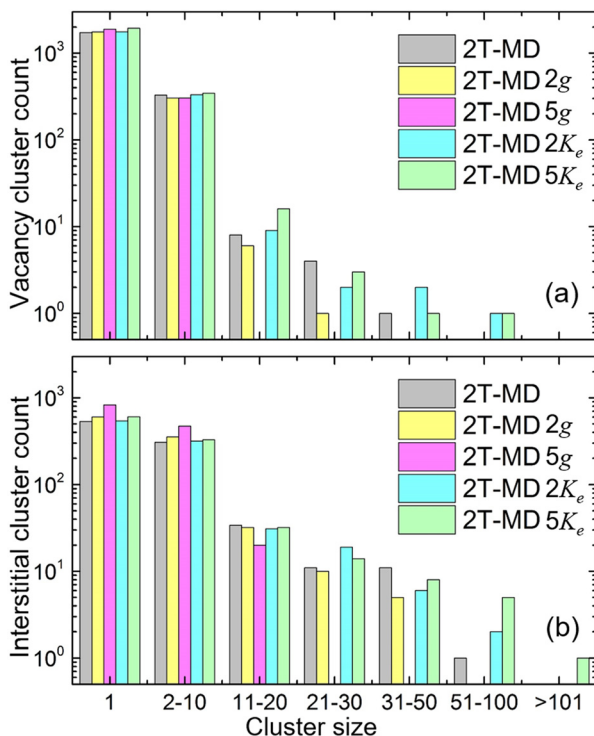


**FIG. 32.** 2T-MD simulations of 150 keV Ni ion cascades with various  $e\text{-}ph$  coupling strengths ( $g$ ) and the electrical thermal conductivities ( $K_e$ ). Reproduced with permission from Zarkadoula *et al.*, Comput. Mater. Sci. **162**, 156–161 (2019). Copyright 2019 Elsevier.

### C. Nonequilibrium damage evolution

First principles-based techniques, such as TD-DFT or AIMD, can be used to model phenomena localized in a small volume where the energy is dissipated within very short time periods. DFT results for vacancy and interstitial formation energy distributions can be used to identify whether any elemental constituents are particularly prone to form point defects and small clusters in an alloy, and whether specific compositions strongly increase defect formation energies. Both the average formation energy and variations in the distribution are important, as local low-energy sites and chemical environments provide traps for vacancies or interstitials and, in turn, modify radiation resistance resulting from nonequilibrium processes.

#### 1. Defect energetics, directional mass transport, and defect evolution

Whereas conventional thermal diffusion is often controlled by vacancy migration, irradiation damage obeys the mobility of point defects and defect clusters under both athermal nonequilibrium and thermal equilibrium conditions. Because of chemical complexity, energy dissipation processes on both electronic and atomic subsystems can be significantly affected in complex alloys; the defect properties in SP-CSAs are expected to be fundamentally different from those in pure metals and dilute alloys. Formation and migration energies of vacancies and interstitials are studied using first principles calculations based on DFT. An efficient method of calculating the elemental

chemical potentials in SP-CSAs has been demonstrated based on the distribution of nearest neighbors around various atomic sites. The method considers the global composition and local short-range order.<sup>230–232</sup> Since every atom experiences a different local atomic environment, the formation (not shown) and migration energies of vacancies and interstitials exhibit a wide distribution rather than the single value in pure metals or assumed in dilute alloys, as shown in Fig. 33 for migration energies.<sup>80,232</sup> Note that different distributions suggest that defect behavior can be greatly modified by local conditions. Migration energies of vacancies and interstitials exhibit a region of overlap (Fig. 33). Compared with relatively simple CSAs (e.g., NiFe), more significant overlapping of the migration energy distributions is observed in complex CSAs (i.e., NiCoCr and NiFeCoCr). Such overlapping is expected to contribute to enhanced defect annihilation (Figs. 5 and 6), as interstitials and vacancies are mobile in the same temperature regime. Defect formation and migration energies are closely related to the specific atoms and their neighboring atoms, which further determine the elemental diffusion properties.<sup>233,234</sup>

In SP-CSAs, low-energy temporary traps, in which a mobile defect spends most of its time, play a significant role in defect evolution. For example, Fe atoms have lower barriers to exchange with vacancies in  $\text{Ni}_x\text{Fe}_{(1-x)}$ . Once a vacancy finds an Fe atom, it will jump forward and backward, exchanging mainly with the Fe atom, delaying diffusion.<sup>233,234</sup> There is a low probability that an Ni atom will jump and that the vacancy will find another Fe atom to repeat the process. In dilute alloys, the number of such traps is small. With an increasing Fe concentration closer to the site percolation threshold ( $\sim 20$  at. % Fe), the more such traps exist, the higher the probability of delaying vacancy diffusion. Beyond this threshold, the possibility of forming links between Fe atoms and vacancies increases (possible jumps from Fe to Fe increase); therefore, the diffusion coefficient increases with the Fe concentration.<sup>233</sup> The overall effect of atomic transport can be significantly influenced by low energy barriers (e.g., Fig. 33 low-energy side of the energy distribution). The lower these energy barriers, the stronger the sluggish diffusion effect. Interactions between defects residing in these temporary traps significantly slow the entire defect evolution process. Interactions with traps depend on the specific transport mechanism (vacancies, interstitials, and defect clusters); and, in general, the effect is minimized near the percolation threshold. Multiscale computational techniques, such as DFT, MD, and on-the-fly kinetic Monte Carlo (kMC) and object kMC, identify the chemical conditions and atomic arrangements for the minimal interaction of defects with the temporary traps so that initial properties are “frozen-in,” providing insights into the observed 3D short-range vs 1D long-range migration mode of defect motion in NiFe and other complex CSAs vs the mode in NiCo and pure Ni.<sup>235</sup>

#### 2. Strain relaxation from inelastic thermal spike

In both fcc and bcc chemically complex CSAs with a strong tendency toward solid solution strengthening, no atoms reside on an ideal lattice position because of the different local environment. Although the underlying lattice structure is well defined on average, the existence of chemical variation leads to intrinsic disorder in atomic positions, as discussed in Sec. III B 2. Such local lattice distortion accommodates elements of various atomic size and electronic structure. The multiple elements do interact with one another in the matrix [i.e., maximized

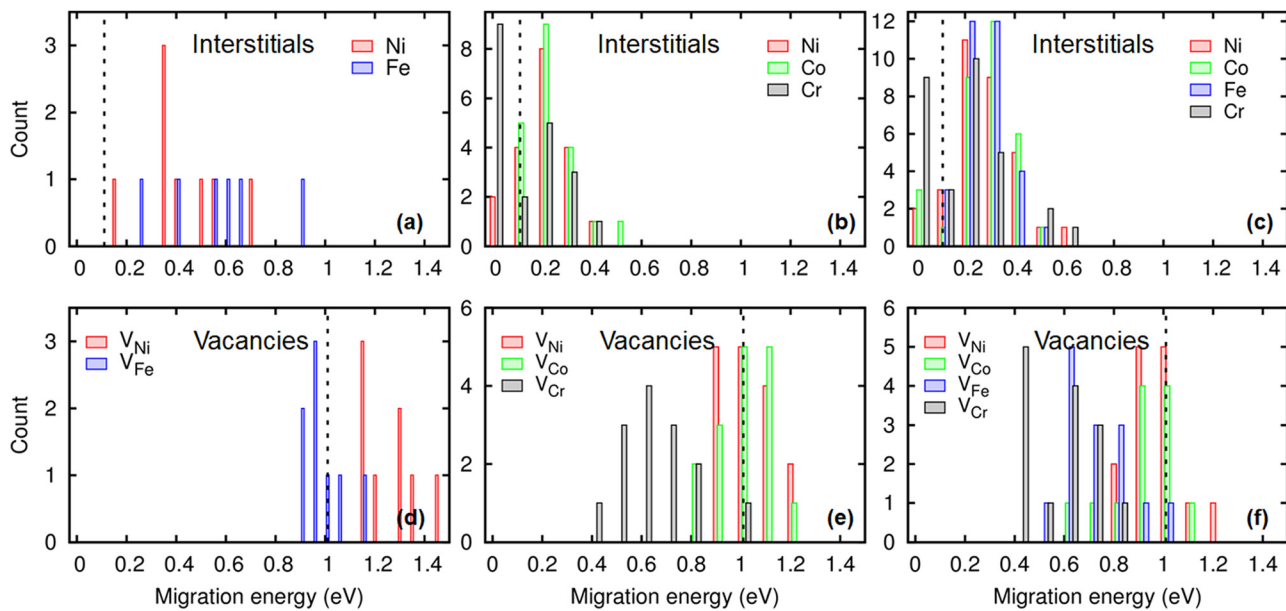


**FIG. 33.** Migration energies for interstitials and vacancies in NiFe, NiCoCr, and NiFeCoCr. Overlapping distributions may enhance defect recombination. The energies for pure Ni are indicated as dotted lines.

disorder due to the existence of a nonuniform lattice parameter,  $a$ : ( $a_{\text{1st}} - a_{\text{avg}}/a_{\text{avg}}$  between the local  $a_{\text{1st}}$  and average  $a_{\text{avg}}$  in the alloys), which is different from the solutes in conventional alloys (limited local disorder). Combined experimental and modeling studies<sup>187,214,232</sup> have shown that charge transfer depends on local atomic environments. The charge transfer reduces the effective volume mismatch. Moreover, recent work<sup>187</sup> connects the difference in the charge transfer among the alloying elements with the lattice distortion; it suggests that the greater difference in the number of valence electrons among the alloying elements may lead to increasing solid solution strength so that the lattice can tolerate more pressure or strain locally.

Atomistic simulations (Fig. 34) have revealed that ion–solid interactions produce extreme local environments—including combinations of high temperature, short-range atomic forces, and high-pressure waves, the energetics of which can affect defect generation.<sup>158</sup> Inevitably, ion-irradiation damage leads to local deformation of the crystal structure that causes measurable elastic strain. The hypothesis that the CSA lattices are stronger and can withstand irradiation-induced stress better than those of pure metals has been confirmed by GIXRD measurement and MD simulations. Total elastic strain induced from Ni ions in Ni, NiFe, and NiFeCoCr is determined by a Bragg peak shift and diffuse scattering in the tails of the Bragg peaks.<sup>32</sup> With increasing Ni ion fluence to  $3 \times 10^{13} \text{ cm}^{-2}$ , there is only a single Bragg peak [indicated by the solid red curve in Fig. 35(a) for the Ni crystals], suggesting little buildup of irradiation-induced elastic strain. In pure Ni, since small clusters migrate more easily (e.g., in Ni and NiCo)<sup>235</sup> and the lattice cannot hold much of the strain, large extended defects (e.g., large loops or dislocations) are commonly observed. The observation in Fig. 35(a) agrees well with large cluster formation in pure Ni.<sup>236</sup> On the other hand, slow heat dissipation in complex CSAs affects the formation of stacking-fault tetrahedra and dislocation loops; and smaller clusters with higher density form in more complex CSAs,

even though the number of total point defects may be lower than the number of single defects and defect clusters.<sup>72,166,236</sup> The strain is predicted to be larger in crystals containing small defect clusters.<sup>237</sup> In NiFe and NiFeCoCr CSAs, smaller defect clusters are formed that cause local elastic strain, more so than the extended defects (e.g., large clusters in pure Ni). As a result, an additional peak (a small shoulder) appears on the left side of the Bragg peak already at a low fluence of  $10^{13} \text{ cm}^{-2}$  (not shown), which becomes more pronounced with increasing Ni fluence [Figs. 35(b) and 35(c)], as the defect cluster density increases. The net tensile strain near the surface region in these irradiated CSAs is summarized in Fig. 36(a) under 1.5 MeV Ni irradiation. The strain level is not linear as a function of the Ni ion fluence, which is attributed to changes in defect configurations and concentrations. During this damage buildup stage under low-energy ion irradiation, as long as the lattice can hold the local pressure or strain induced by the ion bombardment, the strain level will increase. With a further increase in the ion fluence of 1.5 MeV Ni, strain relaxation is expected (not shown), as the defect concentration saturates and defects start to interact, evolve, and grow in size to form larger dislocation loops to reduce the local stain. The strain relief, clearly observed in both in NiFe and NiFeCoCr under 21 MeV Ni irradiation, is attributed to both the annealing of small defect clusters and the formation of larger dislocation loops by the consumption of small defect clusters, as the dissipated ionization energy relaxes the pre-existing defect structure.<sup>141</sup> The impact of ionizing irradiation on the pre-existing defects using 21 MeV Ni ions is discussed in Sec. VD 1.

#### D. Ionization effects in complex metal alloys under ion irradiation

Initial damage events typically produce a collection of defects—primarily vacancies, interstitials, and small clusters of point defects—but

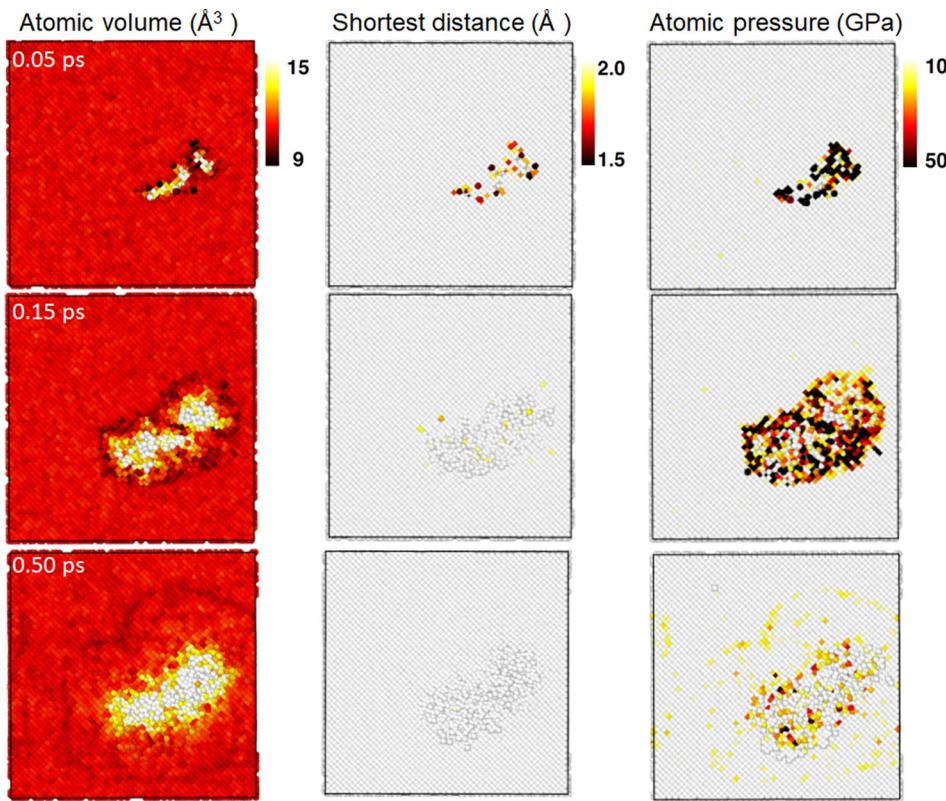


**FIG. 34.** Snapshots of atomic volume (top) during a typical 10 keV collision cascade in Ni, at times 0.05, 0.15, and 0.50 ps, create a supersonic shockwave (bottom), involving pressures of 10–50 GPa.

leave the atomic lattice mostly intact. Material failure due to irradiation originates from the aggregation of these small defects into extended defects, particularly voids and interstitial loops, which in turn leads to irradiation-induced degradation phenomena such as elemental segregation, phase separation, swelling, radiation hardening, and embrittlement. The enhanced coupling between the electronic and atomic subsystems leads not only to smaller defect clusters (as discussed in Secs. V A and V B) during the cascade

events but also to different responses in CSAs with and without pre-existing defects.

### 1. Evolution of pre-existing defects under ionizing irradiation

As discussed in Sec. II A, research on ion-induced irradiation damage has largely focused either on nuclear energy deposition at keV

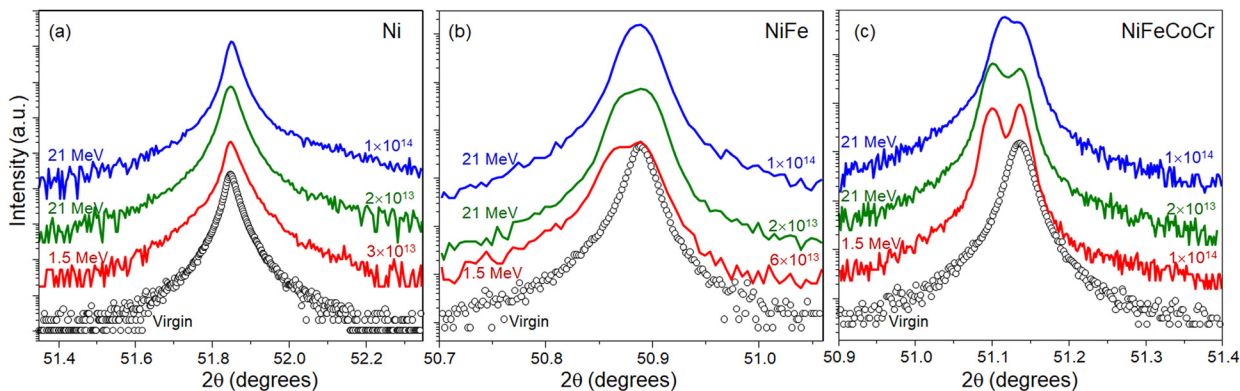


**FIG. 35.** The  $\theta$ - $2\theta$  scans recorded in the vicinity of symmetric reflections for virgin (open circles), 1.5 MeV Ni ion pre-damaged samples with the corresponding fluence noted on the bottom-right corner, and samples subsequently irradiated by 21 MeV Ni ions in (a) Ni, (b) NiFe, and (c) NiFeCoCr to fluences of  $2 \times 10^{13}$  and  $1 \times 10^{14} \text{ cm}^{-2}$ , respectively. Reproduced with permission from Sellami et al., Curr. Opin. Solid State Mater. Sci. **23**, 107 (2019). Copyright 2019 Elsevier.

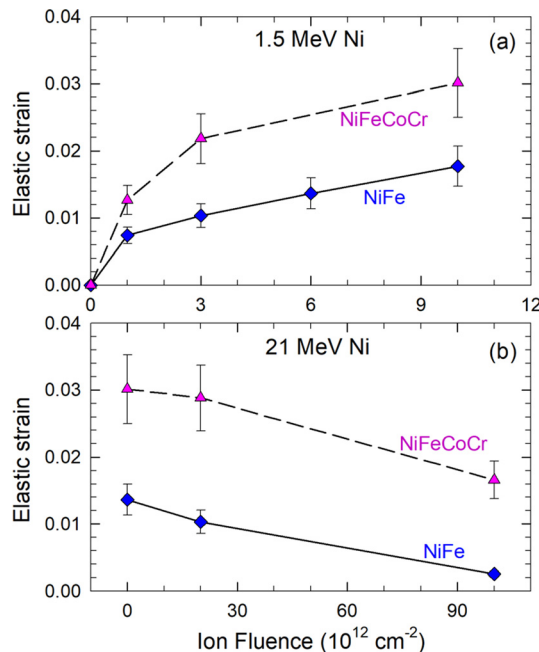


**FIG. 36.** Irradiation-induced elastic strain as a function of Ni fluence after (a) 1.5 and (b) 21 MeV irradiation in NiFe and NiFeCoCr. Reproduced with permission from Sellami *et al.*, *Curr. Opin. Solid State Mater. Sci.* **23**, 107 (2019). Copyright 2019 Elsevier.

energies or on electronic energy deposition at much higher energies (Fig. 1). In the intermediate energy regime (from a few hundreds of keV to a few tens of MeV) where energetic particles simultaneously deposit significant amounts of energy in the electronic and atomic subsystems, it has long been assumed that the large amount of energy deposited to electrons is ultimately dissipated by nondamaging mechanisms (electron excitation and heat dissipation that do not cause lattice defects). The significant amount of energy deposited into the electronic subsystem—which is a dominant fraction for ions with collision energies above a few tens of keV—is often poorly approximated, or even ignored, in conventional atomic-scale models of radiation damage in metals and alloys. It is important to understand how electronic excitation modifies the local environment and migration barriers so that pre-damaged states or small loops become mobile under excitation.

Some recent experimental, theoretical, and computational developments have started to investigate how pre-existing defect configurations respond to electronic energy deposition, as well as to coupled electronic and atomic processes. Pre-damaged states can be created with ions in the highly ballistic regime (keV energy range), and defect evolution under ionizing irradiation is studied using ions with high electron-to-nuclear stopping ratios ( $S_e/S_n$ ) in the MeV–GeV ion range.

Strain relaxation from inelastic thermal spikes is discussed in Sec. VC2 using 21 MeV Ni ions and is detailed in this section as an example to show the impact of ionization on pre-existing defects. X-ray scattering and ion channeling are used to study interactions of energetic particles with pre-existing defects and dislocations (e.g., induced by low-energy heavy ion irradiation, as shown in Fig. 35) and

to determine the change in elastic strain level resulting from changes in defect configurations and densities in irradiated samples. A recent study<sup>32</sup> has reported increasing elastic strain resulting from accumulated damage under prolonged 1.5 MeV Ni irradiation in NiFe and NiFeCoCr [Figs. 35(b), 35(c), and 36(a)]. This damage is, however, sensitive to subsequent highly ionizing 21 MeV Ni irradiation [Fig. 36(b)].

To study the effect of electronic energy deposition on pre-existing damage in crystalline metals, single crystals of Ni, NiFe, and NiCoCrFe have been pre-damaged with 1.5 MeV Ni at ion fluences of  $3 \times 10^{13} \text{ cm}^{-2}$ ,  $6 \times 10^{13} \text{ cm}^{-2}$ , and  $1 \times 10^{14} \text{ cm}^{-2}$ , respectively, and subsequently irradiated with 21 MeV Ni to fluences of  $2 \times 10^{13}$  and  $10^{14} \text{ cm}^{-2}$  (Fig. 35). The Ni crystal has been pre-damaged by relatively low-energy Ni ions at a fluence of  $3 \times 10^{13} \text{ cm}^{-2}$ . As expected, no obvious strain is detected before and after subsequent 21 MeV Ni irradiation [Fig. 35(a)]. With increasing fluence in pure Ni, the diffuse scattering becomes higher on the right side of the Bragg peak (not shown) owing to the generation of large interstitial dislocation loops by elastic nuclear collisions, whereas the energy deposited to electrons dissipates rapidly in Ni with little influence on the atomic defects. For the alloys, the pre-damage irradiation ( $6 \times 10^{13} \text{ cm}^{-2}$  for NiFe and  $1 \times 10^{14} \text{ cm}^{-2}$  for NiFeCoCr) leads to significant elastic strain [Figs. 35(b), 35(c), and 36(a)]. However, the XRD curves recorded on the pre-damaged samples subsequently irradiated with 21 MeV Ni show that the peak separation decreases with increasing fluence [the peak at the low angle side moves toward the Bragg peak, Figs. 35(b) and 35(c)], implying strain relaxation [Fig. 36(b)], during which the strain generated by elastic nuclear collisions undergoes partial relaxation due to the annihilation of interstitial–vacancy pairs or their growth into dislocation loops, depending on the alloy composition and irradiation conditions. This study demonstrates that electronic energy deposition from ion irradiation, even at a moderate level of  $\sim 12 \text{ keV/nm}$ , has a significant impact on pre-existing damage.

## 2. Metallic alloys responding to extreme electronic energy deposition

SHIs with energies of  $\sim 1 \text{ MeV/amu}$  and above, where nuclear energy deposition is negligible, excite the electronic subsystem to extreme nonequilibrium conditions at fs to ps timescales, depending on energy deposition over different time and length scales (Fig. 2). Under SHI irradiation, target electrons are initially excited as a result of extremely high electronic stopping power along the ion path [Fig. 1(c)].

In single-impact simulations, energy deposition and dissipation from a 1.542 GeV Bi ion in Ni, NiFe, and NiCo have been studied using 2T-MD with a parametrization directly calculated from first principles (Fig. 37).<sup>68</sup> The heat flow in the electronic subsystem is very different in these three modeling systems (Sec. II B 2). Replacing 50% of the Ni in pure Ni with Co or Fe reduces the heat dissipation via the electronic subsystem; the highly localized slow energy dissipation in NiCo and NiFe results in melting along the ion path, while there is no melting or detectable damage production in pure Ni. The lifetime of the molten cylindrical region is  $\sim 60$  and 120 ps for NiCo and NiFe, respectively. While a dislocation loop structure and isolated point defects are formed in both alloys, defect clusters are about 20 times more numerous in NiFe than in NiCo. The simulation results are supported by STEM annular bright-field imaging of Ni and NiFe.

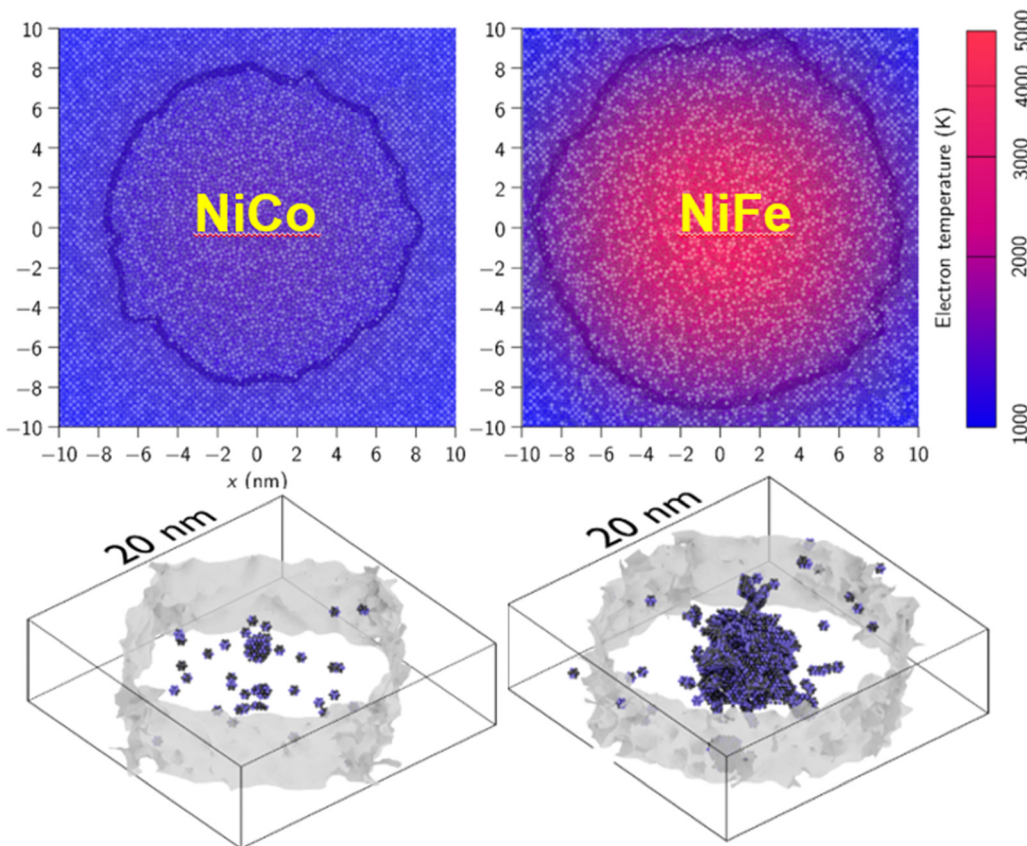


**FIG. 37.** Residual damage in simulation cells. Top: snapshot of MD simulation cells 20 ps after ion impact. Solid–melt interface shown by solid line and electron temperatures shown by color. Bottom row: Melt–solid interface when the molten radius is at its maximum. Small atom fragments are caused by vacancies. Reproduced with permission from Leino *et al.*, *Acta Mater.* **151**, 191–200 (2018). Copyright 2018 Elsevier. Reproduced with permission from Zhang *et al.*, *MRS Bull.* **44**, 798 (2019). Copyright 2019 Cambridge University Press.

Comparing the results with those obtained by an instantaneous energy deposition model, without consideration of *e-ph* interactions, shows a different qualitative behavior. The significance of the 2T-MD model demonstrated here is that Ni-based alloys have remarkable differences in their response to electronic energy loss depending on the alloy composition and thus the chemical complexity.<sup>68</sup> This insight into time-dependent energy dissipation in the electronic substructure and energy transfer from electrons to atoms should be taken into consideration to understand the response of materials subjected to extreme ionizing radiation, especially in chemically complex alloys such as SP-CSAs, when the coupling between the electronic and atomic subsystems is strong.

## VI. MATERIAL MODIFICATION BY ION BEAMS: IRRADIATION CONDITION AND CHEMICAL DISORDER

Scientific understanding and technical development often go hand-in-hand in the successful development of advanced and functional materials or the control/prediction of materials performance to meet growing societal needs for applications in energy conservation and production, a clean environment, and national security. The current situation is just the beginning of a revolutionary change in the systematic understanding and quantitative modeling of damage production and microstructure evolution in materials under ionizing

ion irradiation, where energy transfer processes occur both in and between the electronic and atomic structures. Although there are explanations for the observed property modifications under ionizing ion bombardments, there is no unified or quantified understanding of the underlying mechanisms. What is clear, as illustrated in the examples presented in the preceding sections (Secs. IV and V), is that chemical disorder (chemical inhomogeneity) and bonding characteristics emerge as controlling factors for structural stability and enhanced radiation resistance. Energetic ion beams are a power tool to understand and delineate the coupled electronic/nuclear energy deposition and subsequent nonequilibrium processes in chemically disorder ceramics and metallic alloys.

Historical use of ion beams has been focused on relatively separate aspects of the energy processes: nuclear energy deposition (e.g., doping in the semiconductor industry, displacement damage in nuclear materials) and electronic energy deposition (e.g., ion beam analysis and SHI applications) that until a decade or two ago largely ignored electronic energy dissipation processes in both the interpretation and the modeling of dynamics of radiation effects. While only quantified for SiC and SrTiO<sub>3</sub> at room temperature, the separable and distinct effects of ionization-induced recovery processes are critical to understanding and modeling the complex damage accumulation

behavior observed in these and other ceramics as a function of temperature for different ion masses. To understand the coupling effects and quantify the ionization impact, simulations and experiments can be performed by varying nuclear energy loss ( $S_n$ ), electronic energy loss ( $S_e$ ), and the electronic-to-nuclear energy loss ratio ( $S_e/S_n$ ) along channeling or off-channel directions.

With better understanding of cation disorder in single-phase complex ceramics and chemical heterogeneity from the elemental diversity in SP-CSAs, targeted transition metals with unique electronic structures can be selected to tune the  $e\text{-}ph$  coupling strength and heat capacity, which affect local energy dissipation and defect annealing. This approach provides a path forward to investigate, delineate, and understand athermal radiation effects. Moreover, ionizing ion beams can be used to modify materials properties by reordering or amorphizing the local atomic arrangements. A few examples are briefly described in the following paragraphs.

Ionizing charged-particle beams (both ion and electron) can sculpt functional nanochannels in oxides. Researchers have discovered that far-from-equilibrium processes under sequential energetic ion and electron irradiation produce functional nanochannels in complex oxides with atomic-level precision, such as in  $\text{Yb}_2\text{Ti}_2\text{O}_7$  and  $\text{Gd}_2\text{TiZrO}_7$  with the pyrochlore structure.<sup>61</sup> Along an energetic ion's trajectory in many complex oxides, nonequilibrium superheating leads to a linear nanoscale amorphous track or nanochannel. Subsequent irradiation with an electron beam focused to atomic dimensions creates far-from-equilibrium conditions at the atomic level that transform the amorphous phase in  $\text{Yb}_2\text{Ti}_2\text{O}_7$  and  $\text{Gd}_2\text{TiZrO}_7$  to a highly oxygen-conducting metastable phase with atomic precision. This electron-beam guided transformation is dependent on composition, which has been confirmed by MD simulations. Understanding far-from-equilibrium processes under ion and electron irradiation can lead to nanopatterning of functional phases and engineering of complex interfaces. New understanding of nonequilibrium fast electronic processes (fs to sub-ns), which use energetic ions to sculpt cylindrical nanophases and sequential focused electron beams to induce phase transitions and new functionalities, will promote the application of guided ion/electron-beam irradiation to nanopattern new functional phases with atomic precision.

Defect production and damage accumulation under nuclear and electronic energy depositions have been studied in model  $\text{ABO}_3$  oxides: single-crystalline  $\text{SrTiO}_3$ ,<sup>23,50,53,55,56</sup>  $\text{KTaO}_3$ ,<sup>202–204</sup>  $\text{LiTaO}_3$ ,<sup>57,208</sup> and  $\text{LiNbO}_3$ .<sup>52</sup> While highly ionizing ions may not produce amorphous or damage tracks in pristine  $\text{ABO}_3$  structures, electronic energy deposition interacts with pre-existing defects leading to synergistic damage production or defect annealing. More specifically, intense electronic energy deposition may result in a rapid, nonlinear increase in damage production (the synergistic effect) and even lead to full amorphization. There is a significant reduction in the incubation fluence for rapid amorphization with increasing amount of accumulated damage, and the amorphous cross sections exhibit a linear dependence on the initial disorder level. On the other hand, ionization may induce significant defect annihilation and amazingly restore lattice order (the competitive effect). Both synergistic (damaging) or competitive (annealing) effects can occur in the same material for electronic stopping powers either above or below a threshold respectively, demonstrating complex interactions between ionization energy deposition and pre-existing atomic defects.<sup>23,53,55</sup> The potential to shape

nanochannels in  $\text{SrTiO}_3$  is illustrated in Fig. 38.<sup>50</sup> Since the electronic stopping power threshold for amorphous ion track formation depends on the pre-damaged defect state, it is possible to selectively produce nanometer-scale amorphous ion tracks in  $\text{SrTiO}_3$ . Such modifications by ionizing ion beams can be used to tune interfaces for electronic/magnetic functionalities, create 1D polarity in an amorphous state, and engineer crystalline/amorphous interfaces for electronic conduction, as well as selective etching of the amorphous structure.

## VII. OUTLOOK AND SUMMARY

The response of materials to energy deposition from energetic ions is inherently connected with a simultaneous disturbance of the electronic and atomic structures. Energy deposition to the electronic structure produces a large number of electron-hole pairs that can result in the formation of atomic-scale defects or charge alteration of pre-existing defects, localized electronic excitations, rupture of covalent and ionic bonds in ceramics, charge redistributions in metallic alloys, modification of energy barriers, enhanced defect and atomic diffusion, and other effects. As a result, the effects of extreme ionization can have a first-order effect on the kinetics of atomic processes in many materials, especially those with complex elemental inhomogeneities that cause stronger  $e\text{-}ph$  coupling, affecting the evolution of microstructure, phase changes, and thermodynamic properties. Realistic prediction of radiation effects in materials requires a foundational understanding of the coupled processes of electronic and atomic dynamics.

This review highlights the important role of ionization effects on atomic-level defects by combining two aspects at its core: the role of energy dissipation through coupled electronic and atomic subsystems and its impact on atomic processes, and the role of extreme chemical complexity in modifying these energy dissipation mechanisms. To move beyond current knowledge and incremental property improvements in understanding materials responding to ionizing energy deposition, we must understand the roles of all constituents of structural

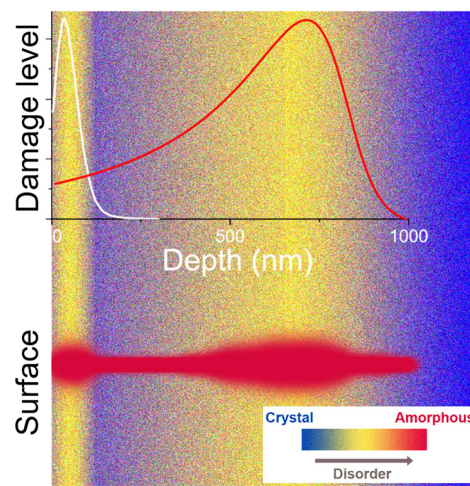


**FIG. 38.** Schematic drawing of a dumbbell-shaped amorphous ion track (bottom) produced by 20 MeV Ti ion irradiation in pre-damaged  $\text{SrTiO}_3$  with a nonuniform initial disorder profile: high damage level close to the surface (white solid line) and peaked near 700 nm (red solid line). Reproduced with permission Xue et al., Acta Mater. 127, 400–406 (2017). Copyright 2019 Elsevier.

stability and their effects on energy dissipation mechanisms at the level of electrons and atoms.

Unlike the relatively simple chemistry of ideal or perfectly ordered materials, the intrinsic lattice distortions, intricate electron-electron interactions, complex energy landscapes, and local stress fluctuations that arise in chemically complex materials are shown to have profound effects on these materials' properties and their response to radiation. Yet the research effort to clarify links between these intrinsic variables and microstructural evolutions under nonequilibrium radiation conditions across all spatial and temporal scales is just starting. Given the complexities of lattice distortion and atomic stress fluctuation (e.g., in multicomponent oxide solid solutions and SP-CSAs), the defects in structurally simple lattices (e.g., perovskite, fluorite, pyrochlore, fcc, or bcc) sit in a wide range of distributions of local environments, in contrast to the very explicit and narrow distributions in traditional oxides or dilute alloys. For chemically complex materials, e.g., high-entropy ceramics and high-entropy alloys, there are many open questions to be addressed. These include the following: (1) How can we understand the intricate correlations between the atomic or electronic constituents, (2) how do the electronic and atomic subsystems respond to energy deposition separately and collectively, (3) how can we control energy flow and mass transport during the correlated, athermal electronic and atomic processes, (4) how can we understand, predict, and ultimately control the dynamics of excited or nonequilibrium states and control matter far away from equilibrium, and (5) how can we reveal underlying crucial knowledge for the development of transformative materials with optimized functionality under extreme conditions? These questions make the study of nonequilibrium defect dynamics at the level of electrons and atoms particularly challenging but critical.

Understanding the varying roles of spatial and temporal processes in the response of materials to energy deposition and transfer processes is critical to developing new functional materials based on the formation of novel defect states, structures far from equilibrium, and a wide variety of nanostructural inhomogeneities, along with realizing exotic and often incredible material properties that are important to many energy and information-related technologies. Control and exploitation of nonequilibrium electronic and atomic interactions thus hold promise for great scientific and technological breakthroughs and the design of novel materials functionalities, as well as for understanding of and predicting radiation effects in materials under extreme radiation environments.

## ACKNOWLEDGMENTS

The review of ceramics was supported by the U.S. Department of Energy, Office of Science, Basic Energy Sciences, Materials Sciences and Engineering Division under Contract No. DE-AC05-00OR22725. The review of metals and alloys was supported as part of the Energy Dissipation to Defect Evolution (EDDE) Energy Frontier Research Center funded by the U.S. Department of Energy, Office of Science, Basic Energy Sciences under Contract No. DE-AC05-00OR22725.

This manuscript has been authored by UT-Battelle, LLC., under Contract No. DE-AC05-00OR22725 with the U.S. Department of Energy (DOE). The U.S. government and the publisher, by accepting the article for publication, acknowledge that

the U.S. government retains a nonexclusive, paid-up, irrevocable, worldwide license to publish or reproduce the published form of this manuscript, or allow others to do so, for U.S. government purposes. The DOE will provide public access to these results of federally sponsored research in accordance with the DOE Public Access Plan (<http://energy.gov/downloads/doe-public-access-plan>).

## DATA AVAILABILITY

The data that support the findings of this study are available from the corresponding authors upon reasonable request.

## REFERENCES

- <sup>1</sup>S. J. Pearton, J. C. Zolper, R. J. Shul, and F. Ren, "GaN: Processing, defects, and devices," *J. Appl. Phys.* **86**, 1 (1999).
- <sup>2</sup>A. Chroneos and H. Bracht, *Appl. Phys. Rev.* **1**, 011301 (2014).
- <sup>3</sup>R. T. Tung, *Appl. Phys. Rev.* **1**, 011304 (2014).
- <sup>4</sup>A. G. Baca, A. M. Armstrong, B. A. Klein, A. A. Allerman, E. A. Douglas, and R. J. Kaplar, *J. Vac. Sci. Technol., A* **38**, 020803 (2020).
- <sup>5</sup>M. Bazzan and C. Sada, *Appl. Phys. Rev.* **2**, 040603 (2015).
- <sup>6</sup>T. Frigge, B. Hafke, T. Witte, B. Krenzer, C. Streubühr, A. Samad Syed, V. Mikšić Trontl, I. Avigo, P. Zhou, M. Ligges, D. von der Linde, U. Bovensiepen, M. Horn-von Hoegen, S. Wippermann, A. Lücke, S. Sanna, U. Gerstmann, and W. G. Schmidt, *Nature* **544**, 207 (2017).
- <sup>7</sup>Y. K. Kim, N. H. Sung, J. D. Denlinger, and B. J. Kim, *Nat. Phys.* **12**, 37 (2016).
- <sup>8</sup>P. W. Anderson, *Science* **235**, 1196 (1987).
- <sup>9</sup>F. Chen, *J. Appl. Phys.* **106**, 081101 (2009).
- <sup>10</sup>N. Toyoda, B. Tilakaratne, I. Saleem, and W.-K. Chu, *Appl. Phys. Rev.* **6**, 020901 (2019).
- <sup>11</sup>L. Jiang, Y. Hu, K. Sun, P. Xiu, M. Song, Y. Zhang, W. L. Boldman, M. L. Crespiello, P. D. Rack, L. Qi, W. J. Weber, and L. Wang, *Adv. Mater.* **32**, 2002652 (2020).
- <sup>12</sup>M. G. Stanford, B. B. Lewis, K. Mahady, J. D. Fowlkes, and P. D. Rack, *J. Vac. Sci. Technol., B* **35**, 030802 (2017).
- <sup>13</sup>M. Kang and R. S. Goldman, *Appl. Phys. Rev.* **6**, 041307 (2019).
- <sup>14</sup>S. A. Norris and M. J. Aziz, *Appl. Phys. Rev.* **6**, 011311 (2019).
- <sup>15</sup>Z. Li and F. Chen, *Appl. Phys. Rev.* **4**, 011103 (2017).
- <sup>16</sup>A. V. Krasheninnikov and K. Nordlund, *J. Appl. Phys.* **107**, 071301 (2010).
- <sup>17</sup>G. Abadias, E. Chason, J. Keckes, M. Sebastiani, G. B. Thompson, E. Barthel, G. L. Doll, C. E. Murray, C. H. Stoessel, and L. Martinu, *J. Vac. Sci. Technol., A* **36**, 020801 (2018).
- <sup>18</sup>G. Greczynski, I. Petrov, J. E. Greene, and L. Hultman, *J. Vac. Sci. Technol., A* **37**, 060801 (2019).
- <sup>19</sup>L. Pelaz, L. A. Marqués, and J. Barbolla, *J. Appl. Phys.* **96**, 5947 (2004).
- <sup>20</sup>G. S. Was and R. S. Averback, in *Comprehensive Nuclear Materials*, edited by R. J. M. Konings (Elsevier, Amsterdam, 2012), Vol. 1, p. 195.
- <sup>21</sup>R. C. Ewing, W. J. Weber, and J. Lian, *J. Appl. Phys.* **95**, 5949 (2004).
- <sup>22</sup>F. García Ferré, A. Mairov, M. Vanazzi, Y. Serruys, F. Leprêtre, L. Beck, L. Van Brutzel, A. Chartier, M. G. Beghi, K. Sridharan, and F. Di Fonzo, *Acta Mater.* **143**, 156 (2018).
- <sup>23</sup>W. J. Weber, D. M. Duffy, L. Thomé, and Y. Zhang, *Curr. Opin. Solid State Mater. Sci.* **19**, 1–11 (2015).
- <sup>24</sup>Y. Zhang, T. Egami, and W. J. Weber, *MRS Bull.* **44**, 798 (2019).
- <sup>25</sup>D. M. Duffy, S. L. Daraszewicz, and J. Mulroue, *Nucl. Instrum. Methods Phys. Res., Sect. B* **277**, 21 (2012).
- <sup>26</sup>G. Szenes and L. Toth, *Phys. Scr.* **94**, 115810 (2019).
- <sup>27</sup>Y. Zhang, R. Sachan, O. H. Pakarinen, M. F. Chisholm, P. Liu, H. Xue, and W. J. Weber, *Nat. Commun.* **6**, 8049 (2015).
- <sup>28</sup>Y. Zhang, H. Xue, E. Zarkadoula, R. Sachan, C. Ostrouchov, P. Liu, X. Wang, S. Zhang, T. S. Wang, and W. J. Weber, *Curr. Opin. Solid State Mater. Sci.* **21**, 285–298 (2017).
- <sup>29</sup>M. Bricout, C. Onofri, A. Debelle, Y. Pipon, R. C. Belin, F. Garrido, F. Lepretré, and G. Gutierrez, *J. Nucl. Mater.* **531**, 151967 (2020).
- <sup>30</sup>A. Debelle, L. Thomé, I. Monnet, F. Garrido, O. H. Pakarinen, and W. J. Weber, *Phys. Rev. Mater.* **3**, 063609 (2019).

- <sup>31</sup>L. Thomé, G. Gutierrez, I. Monnet, F. Garrido, and A. Debelle, *J. Mater. Sci.* **55**, 5938–5947 (2020).
- <sup>32</sup>N. Sellami, A. Debelle, M. W. Ullah, H. M. Christen, J. K. Keum, H. Bei, H. Xue, W. J. Weber, and Y. Zhang, *Curr. Opin. Solid State Mater. Sci.* **23**, 107–115 (2019).
- <sup>33</sup>K. Nordlund, S. J. Zinkle, A. E. Sand, F. Granberg, R. S. Averback, R. Stoller, T. Suzudo, L. Malerba, F. Banhart, W. J. Weber, F. Willaime, S. L. Dudarev, and D. Simeone, *Nat. Commun.* **9**, 1084 (2018).
- <sup>34</sup>J. F. Ziegler, see <http://www.srim.org> for “SRIM-2013 Software Package.”
- <sup>35</sup>W. J. Weber and Y. Zhang, *Curr. Opin. Solid State Mater. Sci.* **23**, 100757 (2019).
- <sup>36</sup>Y. G. Li, Y. Yang, M. P. Short, Z. J. Ding, Z. Zeng, and J. Li, *Sci. Rep.* **5**, 18130 (2015).
- <sup>37</sup>Y. Yang, Y. G. Li, M. P. Short, C.-S. Kim, K. K. Berggren, and J. Li, *Nanoscale* **10**, 1598–1606 (2018).
- <sup>38</sup>N. Sarkar and N. K. Puri, *International Journal of Creative Research Thoughts* **6**, 56–63 (2018); available at <http://ijcrt.org/papers/IJCRT1801291.pdf>.
- <sup>39</sup>C. Borschel and C. Ronning, *Nucl. Instrum. Methods Phys. Res., Sect. B* **269**, 2133 (2011).
- <sup>40</sup>J.-P. Crocombe and C. Van Wambeke, *EPJ Nucl. Sci. Technol.* **5**, 7 (2019).
- <sup>41</sup>S. Chen and D. Bernard, *Results Phys.* **16**, 102835 (2020).
- <sup>42</sup>N. Itoh and A. M. Stoneham, *Materials Modification by Electronic Excitations* (Cambridge University Press, Cambridge, UK, 2001).
- <sup>43</sup>R. L. Fleischer, P. B. Price, and R. M. Walker, *J. Appl. Phys.* **36**, 3645–3652 (1965).
- <sup>44</sup>J. M. Pruneda, D. Sanchez-Portal, A. Arnaud, J. I. Juaristi, and E. Artacho, *Phys. Rev. Lett.* **99**, 235501 (2007).
- <sup>45</sup>W. J. Weber, L. Wang, Y. Zhang, W. Jiang, and I. Bae, *Nucl. Instrum. Methods Phys. Res., Sect. B* **266**, 2793–2796 (2008).
- <sup>46</sup>L. Thomé, A. Debelle, F. Garrido, P. Trocellier, Y. Serruys, G. Velisa, and S. Miro, *Appl. Phys. Lett.* **102**, 141906 (2013).
- <sup>47</sup>Y. Zhang, T. Varga, M. Ishimaru, P. D. Edmondson, H. Xue, P. Liu, S. Moll, F. Namavar, C. Hardiman, S. Shannon, and W. J. Weber, *Nucl. Instrum. Methods Phys. Res., Sect. B* **327**, 33–43 (2014).
- <sup>48</sup>H. Xue, Y. Zhang, and W. J. Weber, *Mater. Res. Lett.* **5**, 494–500 (2017).
- <sup>49</sup>P. Liu, Y. Zhang, H. Xue, K. Jin, M. L. Crespillo, X. Wang, and W. J. Weber, *Acta Mater.* **105**, 429–437 (2016).
- <sup>50</sup>H. Xue, E. Zarkadoula, P. Liu, K. Jin, Y. Zhang, and W. J. Weber, *Acta Mater.* **127**, 400–406 (2017).
- <sup>51</sup>W. A. Hanson, M. K. Patel, M. L. Crespillo, F. Zhang, S. J. Zinkle, Y. Zhang, and W. J. Weber, *Acta Mater.* **173**, 195–205 (2019).
- <sup>52</sup>N. Sellami, M. Crespillo, H. Xue, Y. Zhang, and W. J. Weber, *J. Phys. D* **50**, 325103 (2017).
- <sup>53</sup>W. J. Weber, H. Xue, E. Zarkadoula, and Y. Zhang, *Scr. Mater.* **173**, 154–157 (2019).
- <sup>54</sup>R. Sachan, E. Zarkadoula, X. Ou, C. Trautmann, Y. Zhang, M. F. Chisholm, and W. J. Weber, *ACS Appl. Mater. Interfaces* **10**, 16731–16738 (2018).
- <sup>55</sup>H. Xue, E. Zarkadoula, R. Sachan, Y. Zhang, C. Trautmann, and W. J. Weber, *Acta Mater.* **150**, 351–359 (2018).
- <sup>56</sup>G. Velisa, E. Wendler, H. Xue, Y. Zhang, and W. J. Weber, *Acta Mater.* **149**, 256–264 (2018).
- <sup>57</sup>N. Sellami, M. L. Crespillo, Y. Zhang, and W. J. Weber, *Mater. Res. Lett.* **6**, 339–344 (2018).
- <sup>58</sup>A. Debelle, M. Backman, L. Thomé, W. J. Weber, M. Toulemonde, S. Mylonas, A. Boulle, O. H. Pakarinen, N. Juslin, F. Djurabekova, K. Nordlund, F. Garrido, and D. Chaussende, *Phys. Rev. B* **86**, 100102 (2012).
- <sup>59</sup>A. Benyagoub and A. Audren, *J. Appl. Phys.* **106**, 083516 (2009).
- <sup>60</sup>M. Toulemonde, W. J. Weber, G. Li, V. Shuththanandan, P. Kluth, T. Yang, Y. Wang, and Y. Zhang, *Phys. Rev. B* **83**, 054106 (2011).
- <sup>61</sup>R. Sachan, V. R. Cooper, B. Liu, D. S. Aidhy, B. K. Voas, M. Lang, X. Ou, C. Trautmann, Y. Zhang, M. F. Chisholm, and W. J. Weber, *J. Phys. Chem. C* **121**, 975–981 (2017).
- <sup>62</sup>Z. G. Wang, C. Dufour, E. Paumier, and M. Toulemonde, *J. Phys.* **7**, 2525 (1995).
- <sup>63</sup>A. Dunlop, D. Lesueur, P. Legrand, H. Dammak, and J. Dural, *Nucl. Instrum. Methods Phys. Res., Sect. B* **90**, 330–338 (1994).
- <sup>64</sup>C. Dufour, Z. G. Wang, M. Levalois, P. Marie, E. Paumier, F. Pawlak, and M. Toulemonde, *Nucl. Instrum. Methods Phys. Res., Sect. B* **107**, 218–222 (1996).
- <sup>65</sup>H. Dammak, A. Dunlop, and D. Lesueur, *Nucl. Instrum. Methods Phys. Res., Sect. B* **107**, 204–211 (1996).
- <sup>66</sup>K. H. Bennemann, *J. Phys.* **16**, R995–R1056 (2004).
- <sup>67</sup>A. I. Ryazanov, S. A. Pavlov, E. V. Metelkin, and A. V. Zhemerev, *J. Exp. Theor. Phys.* **101**, 120–127 (2005).
- <sup>68</sup>A. Leino, G. D. Samolyuk, R. Sachan, F. Granberg, W. J. Weber, H. Bei, J. Liu, P. Zhai, and Y. Zhang, *Acta Mater.* **151**, 191–200 (2018).
- <sup>69</sup>R. Sachan, M. W. Ullah, M. F. Chisholm, J. Liu, P. Zhai, D. Schaures, P. Kluth, C. Trautmann, H. Bei, W. J. Weber, and Y. Zhang, *Mater. Des.* **150**, 1–8 (2018).
- <sup>70</sup>A. M. Rutherford and D. M. Duffy, *J. Phys.* **19**, 496201 (2007).
- <sup>71</sup>A. Dovenbeck and A. Wucher, *Phys. Rev. B* **72**, 165408 (2005).
- <sup>72</sup>E. Zarkadoula, G. Samolyuk, and W. J. Weber, *J. Alloys Compd.* **700**, 106–112 (2017).
- <sup>73</sup>D. M. Duffy, N. Itoh, A. M. Rutherford, and A. M. Stoneham, *J. Phys.* **20**, 082201 (2008).
- <sup>74</sup>R. E. Stoller, A. Tamm, L. K. Beland, G. D. Samolyuk, G. M. Stocks, A. Caro, L. V. Slipchenko, Y. N. Ossetskiy, A. Aabloo, M. Klintenberg, and Y. Wang, *J. Chem. Theory Comput.* **12**, 2871–2879 (2016).
- <sup>75</sup>D. S. Aidhy, C. Lu, K. Jin, H. Bei, Y. Zhang, L. Wang, and W. J. Weber, *Acta Mater.* **99**, 69–76 (2015).
- <sup>76</sup>J. Zhang, M. Lang, R. C. Ewing, R. Devanathan, W. J. Weber, and M. Toulemonde, *J. Mater. Res.* **25**, 1344 (2010).
- <sup>77</sup>A. Tamm, M. Caro, A. Caro, G. Samolyuk, M. Klintenberg, and A. Correa, *Phys. Rev. Lett.* **120**, 185501 (2018).
- <sup>78</sup>E. E. Quashie and A. A. Correa, *Phys. Rev. B* **98**, 235122 (2018).
- <sup>79</sup>Y. N. Ossetskiy, A. Barashev, and Y. Zhang, *Materialia* **4**, 139–146 (2018).
- <sup>80</sup>G. Velisa, E. Wendler, S. Zhao, K. Jin, H. Bei, W. J. Weber, and Y. Zhang, *Mater. Res. Lett.* **6**, 136–141 (2018).
- <sup>81</sup>R. A. Brown, J. C. McCallum, and J. S. Williams, *Nucl. Instrum. Methods Phys. Res., Sect. B* **54**, 197–203 (1991).
- <sup>82</sup>X. Bai, Y. Liu, W. Chen, C. Qi, X. Jin, G. Wang, R. Li, C. Wang, and J. Li, *AIP Adv.* **9**, 115010 (2019).
- <sup>83</sup>S. Mirabella, D. De Salvador, E. Napolitani, E. Bruno, and F. Priolo, *J. Appl. Phys.* **113**, 031101 (2013).
- <sup>84</sup>H. Assmann and H. Stehle, *Nucl. Eng. Des.* **48**, 49 (1978).
- <sup>85</sup>H. Matzke, *Radiat. Eff.* **75**, 317 (1983).
- <sup>86</sup>H. Matzke, P. G. Lucuta, and T. Wiss, *Nucl. Instrum. Methods Phys. Res., Sect. B* **166–167**, 920 (2000).
- <sup>87</sup>S. J. Zinkle, V. A. Skuratov, and D. T. Hoelzer, *Nucl. Instrum. Methods Phys. Res., Sect. B* **191**, 758 (2002).
- <sup>88</sup>G. S. Was, *Fundamentals of Radiation Materials Science*, 2nd ed. (Springer, New York, 2017).
- <sup>89</sup>W. Qin, T. Nagase, and Y. Umakoshi, *Acta Mater.* **57**, 1300 (2009).
- <sup>90</sup>S. Zhang, K. Nordlund, F. Djurabekova, F. Granberg, Y. Zhang, and T. S. Wang, *Mater. Res. Lett.* **5**, 433–439 (2017).
- <sup>91</sup>Y. Zhang, J. Lian, C. M. Wang, W. Jiang, R. C. Ewing, and W. J. Weber, *Phys. Rev. B* **72**, 094112 (2005).
- <sup>92</sup>J. Rest, M. W. D. Cooper, J. Spino, J. A. Turnbull, P. Van Uffelen, and C. T. Walker, *J. Nucl. Mater.* **513**, 310 (2019).
- <sup>93</sup>M. W. D. Cooper, C. R. Stanek, J. A. Turnbull, B. P. Uberuaga, and D. A. Andersson, *J. Nucl. Mater.* **481**, 125 (2016).
- <sup>94</sup>J. L. Wormald and A. I. Hawari, *J. Mater. Res.* **30**, 1485 (2015).
- <sup>95</sup>W. Setaywan, M. W. D. Cooper, K. J. Roche, R. J. Kurtz, B. P. Uberuaga, D. A. Andersson, and B. D. Wirth, *J. Appl. Phys.* **124**, 075107 (2018).
- <sup>96</sup>Y. Zhang, W. Jiang, C. Wang, F. Namavar, P. D. Edmondson, Z. Zhu, F. Gao, J. Lian, and W. J. Weber, *Phys. Rev. B* **82**, 184105 (2010).
- <sup>97</sup>P. D. Edmondson, W. J. Weber, F. Namavar, and Y. Zhang, *Scr. Mater.* **65**, 675–678 (2011).
- <sup>98</sup>Y. Zhang, D. S. Aidhy, T. Varga, S. Moll, P. D. Edmondson, F. Namavar, K. Jin, C. N. Ostrochov, and W. J. Weber, *Phys. Chem. Chem. Phys.* **16**, 8051–8059 (2014).
- <sup>99</sup>P. D. Edmondson, Y. Zhang, S. Moll, T. Varga, F. Namavar, and W. J. Weber, *Phys. Rev. B* **85**, 214113 (2012).

- <sup>100</sup>N. Nafsin, J. A. Aguiar, T. Aoki, A. M. Thron, K. V. Benthem, and R. H. R. Castro, *Acta Mater.* **136**, 224–234 (2017).
- <sup>101</sup>I. Bae, Y. Zhang, W. J. Weber, M. Higuchi, and L. Giannuzzi, *Appl. Phys. Lett.* **90**, 021912 (2007).
- <sup>102</sup>L. M. Wang and W. J. Weber, *Philos. Mag. A* **79**, 237–253 (1999).
- <sup>103</sup>W. A. Hanson, M. K. Patel, M. L. Crespi, Y. Zhang, and W. J. Weber, *Acta Mater.* **161**, 302 (2018).
- <sup>104</sup>I. M. Robertson, J. S. Vetrano, M. A. Kirk, and M. L. Jenkins, *Philos. Mag. A* **63**, 299–318 (1991).
- <sup>105</sup>ASTM E521, “Standard practice for neutron radiation damage simulation by charged-particle irradiation,” *Annual Book of ASTM Standards* (ASTM International, West Conshohocken, PA, 2009), Vol. 12, p. 2.
- <sup>106</sup>E. Zarkadoula, G. Samolyuk, and W. J. Weber, *Comput. Mater. Sci.* **162**, 156–161 (2019).
- <sup>107</sup>E. Zarkadoula, G. Samolyuk, and W. J. Weber, *AIP Adv.* **8**, 015121 (2018).
- <sup>108</sup>F. Granberg, K. Nordlund, M. W. Ullah, K. Jin, C. Lu, H. Bei, L. Wang, F. Djurabekova, W. J. Weber, and Y. Zhang, *Phys. Rev. Lett.* **116**, 135504 (2016).
- <sup>109</sup>Y. Zhang, G. M. Stocks, K. Jin, C. Lu, H. Bei, B. C. Sales, L. Wang, L. K. Béland, R. E. Stoller, G. D. Samolyuk, M. Caro, A. Caro, and W. J. Weber, *Nat. Commun.* **6**, 8736 (2015).
- <sup>110</sup>M. Norgett, M. T. Robinson, and I. Torrens, *Nucl. Eng. Des.* **33**, 50–54 (1975).
- <sup>111</sup>Y. Zhang, M. A. Tunas, M. L. Crespi, F. Zhang, W. L. Boldman, P. D. Rack, L. Jiang, C. Xu, G. Greaves, S. E. Donnelly, L. Wang, and W. J. Weber, *Nanotechnology* **30**, 294004 (2019).
- <sup>112</sup>R. E. Stoller, M. B. Toloczo, G. S. Was, A. G. Certain, S. Dwaraknath, and F. A. Garner, *Nucl. Instrum. Methods Phys. Res., Sect. B* **310**, 75–80 (2013).
- <sup>113</sup>J. M. Soler, E. Artacho, J. D. Gale, A. García, J. Junquera, P. Ordejón, and D. Sánchez-Portal, *J. Phys.* **14**, 2745–2779 (2002).
- <sup>114</sup>H. Y. Xiao, W. J. Weber, Y. Zhang, X. T. Zu, and S. Li, *Sci. Rep.* **5**, 8265 (2015).
- <sup>115</sup>H. Y. Xiao, W. J. Weber, Y. Zhang, and X. T. Zu, *Acta Mater.* **87**, 273–282 (2015).
- <sup>116</sup>H. Y. Xiao, X. T. Zu, F. Gao, and W. J. Weber, *J. Appl. Phys.* **105**, 123527 (2009).
- <sup>117</sup>F. Gao, H. Y. Xiao, X. T. Zu, M. Posselt, and W. J. Weber, *Phys. Rev. Lett.* **103**, 027405 (2009).
- <sup>118</sup>H. Y. Xiao, F. Gao, and W. J. Weber, *J. Phys.* **22**, 415801 (2010).
- <sup>119</sup>I. T. Todorov, B. Smith, M. T. Dove, and K. Trachenko, *J. Mater. Chem.* **16**, 1911–1918 (2006).
- <sup>120</sup>M. A. Seaton, I. T. Todorov, S. L. Daraszewicz, G. S. Khara, and D. M. Duffy, *Mol. Simul.* **2018**, 1.
- <sup>121</sup>S. Plimpton, *J. Comput. Phys.* **117**, 1–9 (1995).
- <sup>122</sup>K. Nordlund, M. Ghaly, R. S. Averback, M. Caturla, T. Diaz de la Rubia, and J. Tarus, *Phys. Rev. B* **57**, 7556–7570 (1998).
- <sup>123</sup>D. M. Duffy and A. M. Rutherford, *J. Phys.* **19**, 016207 (2007).
- <sup>124</sup>R. Darkins and D. M. Duffy, *Comput. Mater. Sci.* **147**, 145–153 (2018).
- <sup>125</sup>A. A. Leino, S. L. Daraszewicz, O. H. Pakarinen, F. Djurabekova, K. Nordlund, B. Afra, and P. Kluth, *Nucl. Instrum. Methods Phys. Res., Sect. B* **326**, 289–292 (2014).
- <sup>126</sup>A. E. Ismail, J. A. Greathouse, P. S. Crozier, and S. M. Foiles, *J. Phys.* **22**, 225405 (2010).
- <sup>127</sup>C. Zhang, F. Mao, and F.-S. Zhang, *J. Phys.* **25**, 235402 (2013).
- <sup>128</sup>J. Cui, Z. Zhou, B. Fu, and Q. Hou, *Nucl. Instrum. Methods Phys. Res., Sect. B* **471**, 90–99 (2020).
- <sup>129</sup>E. Zarkadoula, R. Devanathan, W. J. Weber, M. A. Seaton, I. T. Todorov, K. Nordlund, M. T. Dove, and K. Trachenko, *J. Appl. Phys.* **115**, 083507 (2014).
- <sup>130</sup>E. Zarkadoula, D. M. Duffy, K. Nordlund, M. A. Seaton, I. T. Todorov, W. J. Weber, and K. Trachenko, *J. Phys.* **27**, 135401 (2015).
- <sup>131</sup>J.-P. Crocombete, *Comput. Mater. Sci.* **147**, 168–175 (2018).
- <sup>132</sup>O. Osmani, N. Medvedev, M. Schleberger, and B. Rethfeld, *Phys. Rev. B* **84**, 214105 (2011).
- <sup>133</sup>M. I. Kaganov, I. M. Lifshitz, and L. V. Tanatarov, *Journal of Experimental and Theoretical Physics* **4**, 173 (1957); available at [http://www.jetp.ac.ru/cgi-bin/dn/e\\_004\\_02\\_0173.pdf](http://www.jetp.ac.ru/cgi-bin/dn/e_004_02_0173.pdf).
- <sup>134</sup>M. Toulemonde, C. Dufour, A. Meftah, and E. Paumier, *Nucl. Instrum. Methods Phys. Res., Sect. B* **166–167**, 903 (2000).
- <sup>135</sup>D. S. Ivanov and L. V. Zhigilei, *Phys. Rev. B* **68**, 064114 (2003).
- <sup>136</sup>M. Backman, F. Djurabekova, O. H. Pakarinen, K. Nordlund, Y. Zhang, M. Toulemonde, and W. J. Weber, *Nucl. Instrum. Methods Phys. Res., Sect. B* **303**, 129–132 (2013).
- <sup>137</sup>M. Backman, F. Djurabekova, O. H. Pakarinen, K. Nordlund, Y. Zhang, M. Toulemonde, and W. J. Weber, *J. Phys. D* **45**, 505305 (2012).
- <sup>138</sup>E. Zarkadoula, M. Toulemonde, and W. J. Weber, *Appl. Phys. Lett.* **107**, 261902 (2015).
- <sup>139</sup>S. L. Daraszewicz and D. M. Duffy, *Nucl. Instrum. Methods Phys. Res., Sect. B* **303**, 112–115 (2013).
- <sup>140</sup>B. Y. Mueller and B. Rethfeld, *Phys. Rev. B* **87**, 035139 (2013).
- <sup>141</sup>M. W. Ullah, N. Sellami, A. Leino, H. Bei, Y. Zhang, and W. J. Weber, *Comput. Mater. Sci.* **173**, 109394 (2020).
- <sup>142</sup>W. J. Weber, E. Zarkadoula, O. H. Pakarinen, R. Sachan, M. F. Chisholm, P. Liu, H. Xue, K. Jin, and Y. Zhang, *Sci. Rep.* **5**, 7726 (2015).
- <sup>143</sup>A. Meftah, J. M. Costantini, N. Khalfaoui, S. Boudjadar, J. P. Stoquert, F. Studer, and M. Toulemonde, *Nucl. Instrum. Methods Phys. Res., Sect. B* **237**, 563 (2005).
- <sup>144</sup>M. Toulemonde, W. Assmann, C. Dufour, A. Meftah, F. Studer, and C. Trautmann, *R. Dan. Acad. Sci. Lett., Copenhagen, Mat. Fys. Medd.* **52**, 263 (2006).
- <sup>145</sup>S. L. Daraszewicz, Y. Giret, H. Tanimura, D. M. Duffy, A. L. Shluger, and K. Tanimura, *Appl. Phys. Lett.* **105**, 023112 (2014).
- <sup>146</sup>G. D. Samolyuk, L. K. Béland, G. M. Stocks, and R. E. Stoller, *J. Phys.* **28**, 175501 (2016).
- <sup>147</sup>B. Rethfeld, A. Rämer, N. Brouwer, N. Medvedev, and O. Osmani, *Nucl. Instrum. Methods Phys. Res., Sect. B* **327**, 78 (2014).
- <sup>148</sup>P. Sigmund, R. Dan. Acad. Sci. Lett., Copenhagen, Mat. Fys. Medd. **52**, 557 (2006).
- <sup>149</sup>T. Bierschenk, R. Giulian, B. Afra, M. D. Rodriguez, D. Schaures, S. Mudie, O. H. Pakarinen, F. Djurabekova, K. Nordlund, O. Osmani, N. Medvedev, B. Rethfeld, M. C. Ridgway, and P. Kluth, *Phys. Rev.* **88**, 174111 (2013).
- <sup>150</sup>M. C. Ridgway, T. Bierschenk, R. Giulian, B. Afra, M. D. Rodriguez, L. L. Araujo, A. P. Byrne, N. Kirby, O. H. Pakarinen, F. Djurabekova, K. Nordlund, M. Schleberger, O. Osmani, N. Medvedev, B. Rethfeld, and P. Kluth, *Phys. Rev. Lett.* **110**, 245502 (2013).
- <sup>151</sup>D. S. Aidhy, R. Sachan, E. Zarkadoula, O. H. Pakarinen, M. F. Chisholm, Y. Zhang, and W. J. Weber, *Sci. Rep.* **5**, 16297 (2015).
- <sup>152</sup>R. Sachan, E. Zarkadoula, M. Lang, C. Trautmann, Y. Zhang, M. F. Chisholm, and W. J. Weber, *Sci. Rep.* **6**, 27196 (2016).
- <sup>153</sup>C.-H. Chen, Y. Zhang, Y. Wang, M. L. Crespi, C. L. Fontana, J. T. Graham, G. Duscher, S. C. Shannon, and W. J. Weber, *J. Nucl. Mater.* **472**, 153–160 (2016).
- <sup>154</sup>M. L. Crespi, J. T. Graham, Y. Zhang, and W. J. Weber, *J. Lumin.* **172**, 208 (2016).
- <sup>155</sup>M. L. Crespi, J. T. Graham, F. Agulló-López, Y. Zhang, and W. J. Weber, *Appl. Mater. Today* **12**, 131 (2018).
- <sup>156</sup>A. Caro, M. Alurrade, R. Saliba, and M. Caro, Jr., *Nucl. Mater.* **251**, 72 (1997).
- <sup>157</sup>A. F. Calder, D. J. Bacon, A. V. Barashev, and Y. N. Ossetsky, *Philos. Mag.* **90**, 863–884 (2010).
- <sup>158</sup>L. K. Béland, Y. N. Ossetsky, and R. E. Stoller, *npj Comput. Mater.* **2**, 16007 (2016).
- <sup>159</sup>E. Lopasso, M. Caro, and A. Caro, *Phys. Rev. B* **63**, 174105 (2001).
- <sup>160</sup>H. H. Van Swygenhoven and A. Caro, *Phys. Rev. Lett.* **70**, 2098–2101 (1993).
- <sup>161</sup>H. Van Swygenhoven, M. Spaczler, A. Caro, and D. Farkas, *Phys. Rev. B* **60**, 22 (1999).
- <sup>162</sup>S. Mu, R. J. Olsen, B. Dutta, L. Lindsay, G. D. Samolyuk, T. Berlijn, E. D. Specht, K. Jin, H. Bei, T. Hickel, B. C. Larson, and G. M. Stocks, *npj Comput. Mater.* **6**, 4 (2020).
- <sup>163</sup>M. Caro, A. Tamm, A. A. Correa, and A. Caro, *J. Nucl. Mater.* **507**, 258–266 (2018).
- <sup>164</sup>M. Caro, A. Tamm, A. A. Correa, and A. Caro, *Phys. Rev. B* **99**, 174301 (2019).
- <sup>165</sup>A. Tamm, M. Caro, A. A. Correa, and A. Correa, *Phys. Rev. B* **99**, 174302 (2019).
- <sup>166</sup>E. Zarkadoula, G. Samolyuk, and W. J. Weber, *Mater. Res. Lett.* **7**, 490–495 (2019).
- <sup>167</sup>K. Karsten and P. Ehrhart, *Phys. Rev. B* **51**, 10508 (1995).
- <sup>168</sup>M. Sayed, J. H. Jefferson, A. B. Walker, and A. G. Gullis, *Nucl. Instrum. Methods Phys. Res., Sect. B* **102**, 232 (1995).

- <sup>169</sup>B. A. Turkot, B. W. Lagow, I. M. Robertson, D. V. Forbes, J. J. Coleman, L. E. Rehn, and P. M. Baldo, *J. Appl. Phys.* **80**, 4366 (1996).
- <sup>170</sup>E. Wendler and L. Wendler, *Appl. Phys. Lett.* **100**, 192108 (2012).
- <sup>171</sup>C. Björkas, K. Nordlund, K. Arstila, J. Keinonen, V. D. S. Dhaka, and M. Pessa, *Nucl. Instrum. Methods Phys. Res., Sect. B* **257**, 324 (2007).
- <sup>172</sup>A. Kamarou, W. Wesch, E. Wendler, A. Undisz, and M. Rettenmayr, "Radiation damage formation in InP, InSb, GaAs, GaP, Ge, and Si due to fast ions," *Phys. Rev. B* **78**, 054111 (2008).
- <sup>173</sup>P. Partyka, R. S. Averback, D. V. Forbes, J. J. Coleman, and P. Ehrhart, *J. Appl. Phys.* **83**, 1265 (1998).
- <sup>174</sup>K. E. Sickafus, L. Minervini, R. W. Grimes, J. A. Valdez, M. Ishimaru, F. Li, K. J. McClellan, and T. Hartmann, *Science* **289**, 748–751 (2000).
- <sup>175</sup>J. Lian, L. M. Wang, K. Sun, and R. C. Ewing, *Microsc. Res. Tech.* **72**, 165–181 (2009).
- <sup>176</sup>R. Devanathan, W. J. Weber, and J. D. Gale, *Energy Environ. Sci.* **3**, 1551–1559 (2010).
- <sup>177</sup>M. Lang, M. Toulemonde, J. M. Zhang, F. X. Zhang, C. L. Tracy, J. Lian, Z. Wang, W. J. Weber, D. Severin, M. Bender, C. Trautmann, and R. C. Ewing, *Nucl. Instrum. Methods Phys. Res., Sect. B* **336**, 102–115 (2014).
- <sup>178</sup>R. Perriot, B. P. Uberuaga, R. J. Zamora, D. Perez, and A. F. Voter, *Nat. Commun.* **8**, 618 (2017).
- <sup>179</sup>C. M. Rost, E. Sachet, T. Borman, A. Moballegh, E. C. Dickey, D. Hou, J. L. Jones, S. Curtarolo, and J.-P. Maria, *Nat. Commun.* **6**, 8485 (2015).
- <sup>180</sup>M. R. Levy, R. W. Grimes, and K. E. Sickafus, *Philos. Mag.* **84**, 533–545 (2004).
- <sup>181</sup>J. Lian, J. Chen, L. M. Wang, R. C. Ewing, J. M. Farmer, L. A. Boatner, and K. B. Helean, *Phys. Rev. B* **68**, 134107 (2003).
- <sup>182</sup>J. Lian, K. B. Helean, B. J. Kennedy, L. M. Wang, A. Navrotsky, and R. C. Ewing, *J. Phys. Chem. B* **110**, 2343–2350 (2006).
- <sup>183</sup>S. X. Wang, L. M. Wang, R. C. Ewing, G. S. Was, and G. R. Lumpkin, *Nucl. Instrum. Methods Phys. Res., Sect. B* **148**, 704–709 (1999).
- <sup>184</sup>K. Trachenko, *J. Phys.* **16**, R1491–R1515 (2004).
- <sup>185</sup>D. B. Miracle and O. N. Senkov, *Acta Mater.* **122**, 448–511 (2017).
- <sup>186</sup>B. Cantor, *Entropy* **16**, 4749 (2014).
- <sup>187</sup>H. S. Oh, S. J. Kim, K. Odbadrakh, W. H. Ryu, K. N. Yoon, S. Mu, F. Körmann, Y. Ikeda, C. C. Tasan, D. Raabe, T. Egami, and E. S. Park, *Nat. Commun.* **10**, 2090 (2019).
- <sup>188</sup>M. C. Troparevsky, J. R. Morris, P. R. C. Kent, A. R. Lupini, and G. M. Stocks, *Phys. Rev. X* **5**, 011041 (2015).
- <sup>189</sup>J. Van Vechten, R. Tsu, and F. Saris, *Phys. Lett. A* **74**, 422–426 (1979).
- <sup>190</sup>A. Benyagoub, *Nucl. Instrum. Methods Phys. Res., Sect. B* **365**, 376–379 (2015).
- <sup>191</sup>W. J. Weber, Y. Zhang, and L. M. Wang, *Nucl. Instrum. Methods Phys. Res., Sect. B* **277**, 1–5 (2012).
- <sup>192</sup>W. Jiang, W. J. Weber, Y. Zhang, S. Thevuthasan, and V. Shutthanandan, *Nucl. Instrum. Methods Phys. Res., Sect. B* **207**, 92–99 (2003).
- <sup>193</sup>A. Benyagoub and A. Audren, *Appl. Phys. Lett.* **89**, 241914 (2006).
- <sup>194</sup>M. D. Mihai, P. Ionescu, C. Pantelica, H. Petrascu, C. Craciun, V. Craciun, R. Vasiliu, B. S. Vasiliu, and I. Mercioniu, *Nucl. Instrum. Methods Phys. Res., Sect. B* **450**, 85–89 (2019).
- <sup>195</sup>L. Nuckols, M. L. Crespillo, C. Xu, E. Zarkadoula, Y. Zhang, and W. J. Weber, *Acta Mater.* **199**, 96–106 (2020).
- <sup>196</sup>C. J. Ulmer and A. T. Motta, *Nucl. Instrum. Methods Phys. Res., Sect. B* **410**, 200 (2017).
- <sup>197</sup>W. J. Weber, Y. Zhang, H. Xiao, and L. M. Wang, *RSC Adv.* **2**, 595 (2012).
- <sup>198</sup>S. Ouchani, J.-C. Dran, and J. Chaumont, *Nucl. Instrum. Methods Phys. Res., Sect. B* **132**, 447–451 (1997).
- <sup>199</sup>A.-M. Seydoux-Guillaume, X. Deschanel, C. Baumier, S. Neumeier, W. J. Weber, and S. Peuget, *Am. Miner.* **103**(5), 824–827 (2018).
- <sup>200</sup>Y. Liu, X. Han, M. L. Crespillo, Q. Huang, P. Liu, and X. Wang, *Materialia* **7**, 100402 (2019).
- <sup>201</sup>M. Karlušić, M. Jakšić, H. Lebius, B. Ban-d'Etat, R. Wilhelm, R. Heller, and M. Schleberger, *J. Phys. D* **50**, 205302 (2017).
- <sup>202</sup>G. Velisa, E. Wendler, L.-L. Wang, Y. Zhang, and W. J. Weber, *J. Mater. Sci.* **54**, 149–158 (2019).
- <sup>203</sup>K. Jin, Y. Zhang, and W. J. Weber, *Mater. Res. Lett.* **6**, 531–536 (2018).
- <sup>204</sup>E. Zarkadoula, Y. Zhang, and W. J. Weber, *AIP Adv.* **10**, 015019 (2020).
- <sup>205</sup>X. Han, Y. Liu, Q. Huang, M. L. Crespillo, P. Liu, and X. Wang, *J. Phys. D* **53**, 105304 (2020).
- <sup>206</sup>G. Liu, R. He, S. Akhmadaliev, J. R. Vázquez de Aldana, S. Zhou, and F. Chen, *Nucl. Instrum. Methods Phys. Res., Sect. B* **325**, 43–46 (2014).
- <sup>207</sup>Y. Liu, M. L. Crespillo, Q. Huang, X. Han, X. Wang, and P. Liu, *J. Phys. D* **52**, 175303 (2019).
- <sup>208</sup>X. Han, Y. Liu, M. L. Crespillo, E. Zarkadoula, Q. Huang, X. Wang, and P. Liu, *Crystals* **10**, 877 (2020).
- <sup>209</sup>M. L. Crespillo, J. T. Graham, F. Agulló-López, Y. Zhang, and W. J. Weber, *J. Phys. D* **50**, 155303 (2017).
- <sup>210</sup>M. L. Crespillo, J. T. Graham, F. Agulló-López, Y. Zhang, and W. J. Weber, *J. Phys. Chem. C* **121**, 19758 (2017).
- <sup>211</sup>M. L. Crespillo, J. T. Graham, F. Agulló-López, Y. Zhang, and W. J. Weber, *Crystals* **9**, 95 (2019).
- <sup>212</sup>S. Zhao, Y. Zhang, and W. J. Weber, *J. Phys. Chem. C* **121**, 26622 (2017).
- <sup>213</sup>Y. Zhang, K. Jin, H. Xue, C. Lu, R. J. Olsen, L. K. Beland, M. W. Ullah, S. Zhao, H. Bei, D. S. Aidhy, G. D. Samolyuk, L. Wang, M. Caro, A. Caro, G. M. Stocks, B. C. Larson, I. M. Robertson, and W. J. Weber, *J. Mater. Res.* **31**, 2363 (2016).
- <sup>214</sup>Y. Tong, S. Zhao, H. Bei, T. Egami, Y. Zhang, and F. Zhang, *Acta Mater.* **183**, 172–181 (2020).
- <sup>215</sup>C. P. Flynn and R. S. Averback, *Phys. Rev. B* **38**, 7118–7120 (1988).
- <sup>216</sup>S. Prönnecke, A. Caro, M. Victoria, T. D. de la Rubia, and M. W. Guinan, *J. Mater. Res.* **6**, 483–491 (1991).
- <sup>217</sup>C. P. Race, D. R. Mason, and A. P. Sutton, *New J. Phys.* **12**, 093049 (2010).
- <sup>218</sup>A. A. Correa, J. Kohanoff, E. Artacho, D. Sánchez-Portal, and A. Caro, *Phys. Rev. Lett.* **108**, 213201 (2012).
- <sup>219</sup>Y. Zhang, X. Wang, Y. Osetsky, Y. Tong, R. Harrison, S. E. Donnelly, D. Chen, Y. Wang, H. Bei, B. C. Sales, K. L. More, P. Xiu, L. Wang, and W. J. Weber, *Acta Mater.* **181**, 519–529 (2019).
- <sup>220</sup>K. Jin, S. Mu, K. An, W. D. Porter, G. D. Samolyuk, G. M. Stocks, and H. Bei, *Mater. Des.* **117**, 185–192 (2017).
- <sup>221</sup>B. C. Sales, K. Jin, H. Bei, G. M. Stocks, G. D. Samolyuk, A. F. May, and M. A. McGuire, *Sci. Rep.* **6**, 26179 (2016).
- <sup>222</sup>B. C. Sales, K. Jin, H. Bei, J. Nichols, M. F. Chisholm, A. F. May, N. P. Butch, A. D. Christianson, and M. A. McGuire, *npj Quantum Mater.* **2**, 33 (2017).
- <sup>223</sup>G. Stocks, W. Temmerman, and B. Gyorffy, *Phys. Rev. Lett.* **41**, 339 (1978).
- <sup>224</sup>P. P. Singh, *Solid State Commun.* **76**, 1223–1227 (1990).
- <sup>225</sup>K. Jin, B. C. Sales, G. M. Stocks, G. D. Samolyuk, M. Daene, W. J. Weber, Y. Zhang, and H. Bei, *Sci. Rep.* **6**, 20159 (2016).
- <sup>226</sup>G. D. Samolyuk, S. Mu, A. F. May, B. C. Sales, S. Wimmer, S. Mankovsky, H. Ebert, and G. M. Stocks, *Phys. Rev. B* **98**, 165141 (2018).
- <sup>227</sup>G. D. Samolyuk, C. C. Homes, A. F. May, S. Mu, K. Jin, H. Bei, G. M. Stocks, and B. C. Sales, *Phys. Rev. B* **100**, 075128 (2019).
- <sup>228</sup>M. Caro, L. K. Beland, G. D. Samolyuk, R. E. Stoller, and A. Caro, *J. Alloys Compd.* **648**, 408–413 (2015).
- <sup>229</sup>A. Caro, A. Correa, A. Tamm, G. Samolyuk, and G. Stocks, *Phys. Rev. B* **92**, 144309 (2015).
- <sup>230</sup>S. Zhao, G. M. Stocks, and Y. Zhang, *Phys. Chem. Chem. Phys.* **18**, 24043–24056 (2016).
- <sup>231</sup>S. Zhao, Y. Osetsky, and Y. Zhang, *Acta Mater.* **128**, 391–399 (2017).
- <sup>232</sup>S. Zhao, T. Egami, G. M. Stocks, and Y. Zhang, *Phys. Rev. Mater.* **2**, 013602 (2018).
- <sup>233</sup>Y. N. Osetskiy, L. Beland, A. Barashev, and Y. Zhang, *Curr. Opin. Solid State Mater. Sci.* **22**, 65–74 (2018).
- <sup>234</sup>A. Barashev, Y. N. Osetskiy, H. Bei, C. Lu, L. Wang, and Y. Zhang, *Curr. Opin. Solid State Mater. Sci.* **23**, 92–100 (2019).
- <sup>235</sup>C. Lu, L. Niu, N. Chen, K. Jin, T. Yang, P. Xiu, Y. Zhang, F. Gao, H. Bei, S. Shi, M.-R. He, I. M. Robertson, W. J. Weber, and L. Wang, *Nat. Commun.* **7**, 13564 (2016).
- <sup>236</sup>M. W. Ullah, H. Xue, G. Velisa, K. Jin, H. Bei, W. J. Weber, and Y. Zhang, *Sci. Rep.* **7**, 4146 (2017).
- <sup>237</sup>J. Channagiri, A. Boulle, and A. Debelle, *J. Appl. Crystallogr.* **48**, 252–261 (2015).